16. TITAN-II FUSION-POWER-CORE ENGINEERING

Clement P. C. Wong
Patrick I. H. Cooke
Paul J. Gierszewski
Rodger C. Martin
Shahram Sharafat

James P. Blanchard
Richard L. Creedon
Steven P. Grotz
Farrokh Najmabadi
Don Steiner

Edward T. Cheng
Nasr M. Ghoniem
Mohammad Z. Hasan
Kenneth R. Schultz
Dai-Kai Sze

Contents

16. TITAN-II FUSION-POWER-CORE ENGINEERING

16.1. INTRODUCTION

The TITAN-II reactor is a compact, high-neutron-wall-loading (18 MW/m^2) design. The TITAN-II fusion power core (FPC) is cooled by an aqueous lithium-salt solution which also acts as the breeder material [1]. An overview of the TITAN-II design is given in Section 15. Global parameters of the design are summarized in Table 16.1-I. A detailed list of the TITAN-II operating parameters can be found in Appendix B. The poloidal cross section of the TITAN-II FPC is shown in Figures 16.1-1.

The major feature of the TITAN-II reactor is that the entire primary loop is located at the bottom of a low-temperature, atmospheric-pressure, pure-water pool. Detailed safety analyses show that the TITAN-II pool can contain the afterheat energy of the FPC and will remain at a low enough temperature so that tritium or other radioactive material in the primary-coolant system will not be released (Section 19).

The first wall and blanket of the TITAN-II design consists of stamped side plates made of the low-activation, high-strength ferritic steel, 9-C [2]. These plates, called "J-plates" because of their cross section, are assembled into sub-modules (or blanket lobes) as shown in Figure 16.1-2. Inside each of the lobes are 9-C-clad beryllium rods. These rods occupy the first 20 cm behind the first wall. The blanket lobes are then stacked side-by-side to form a blanket module. The shield is used as a clamp to restrain the lobes from any movement. A cross section and an isometric view of a blanket module are shown, respectively, in Figures 16.1-3 and 16.1-4. Twelve blanket modules and three divertor sections are assembled into a single reactor torus. The vacuum boundary for the FPC, located outside the toroidal-field (TF) coils, acts as a boundary between the pool and the hot torus. The TF coils occupy the space between the back of the shield and the vacuum shell (Figure 16.1-3). Vacuum-duct penetrations through the vacuum shell are located in the region near the divertors.

In this section, the detailed engineering design and analysis of the TITAN-II FPC is presented. The FPC components considered here are the first wall, blanket, shield, and the coil sets. The use of an aqueous solution imposes special constraints on the selection of breeder and structural material because of the corrosion concerns, hydrogen embrittle-

ment, and radiolytic effects. These issues are discussed in Section 16.2. At the same time, the dissolved salt in the coolant changes the thermophysical properties of the coolant and the trade-offs between the lithium concentration in the coolant, neutronics performance (Section 16.3), thermal and structural design (Section 16.4), and power-cycle analysis (Section 16.5) are considered. Other engineering aspects of the TITAN-II design (*i.e.*, divertor and vacuum engineering, tritium systems, safety and waste disposal, and main-

Table 16.1-I.

TITAN-II OPERATING PARAMETERS

Major radius, R_T	3.90	m
Minor plasma radius, r_p	0.60	m
First wall radius, r_{FW}	0.66	m
Primary coolant	Aqueous solution	
Structural material	Ferritic steel 9-C	
Breeder material	$LiNO_3$	
Neutron multiplier	Be	
Coolant inlet temperature	298	°C
Coolant exit temperature	330	°C
Neutron wall load, I_w	18.0	MW/m^2
Radiation heat flux on first wall, q''_o	4.6	MW/m^2
Fusion power, P_f	2290	MW
Total thermal power, P_{th}	3027	MW
Net electric power, P_{net}	900	MWe
Gross efficiency, η_{gross}	35%	
Net efficiency, η_{net}	30%	
Mass power density, MPD	806	kWe/tonne

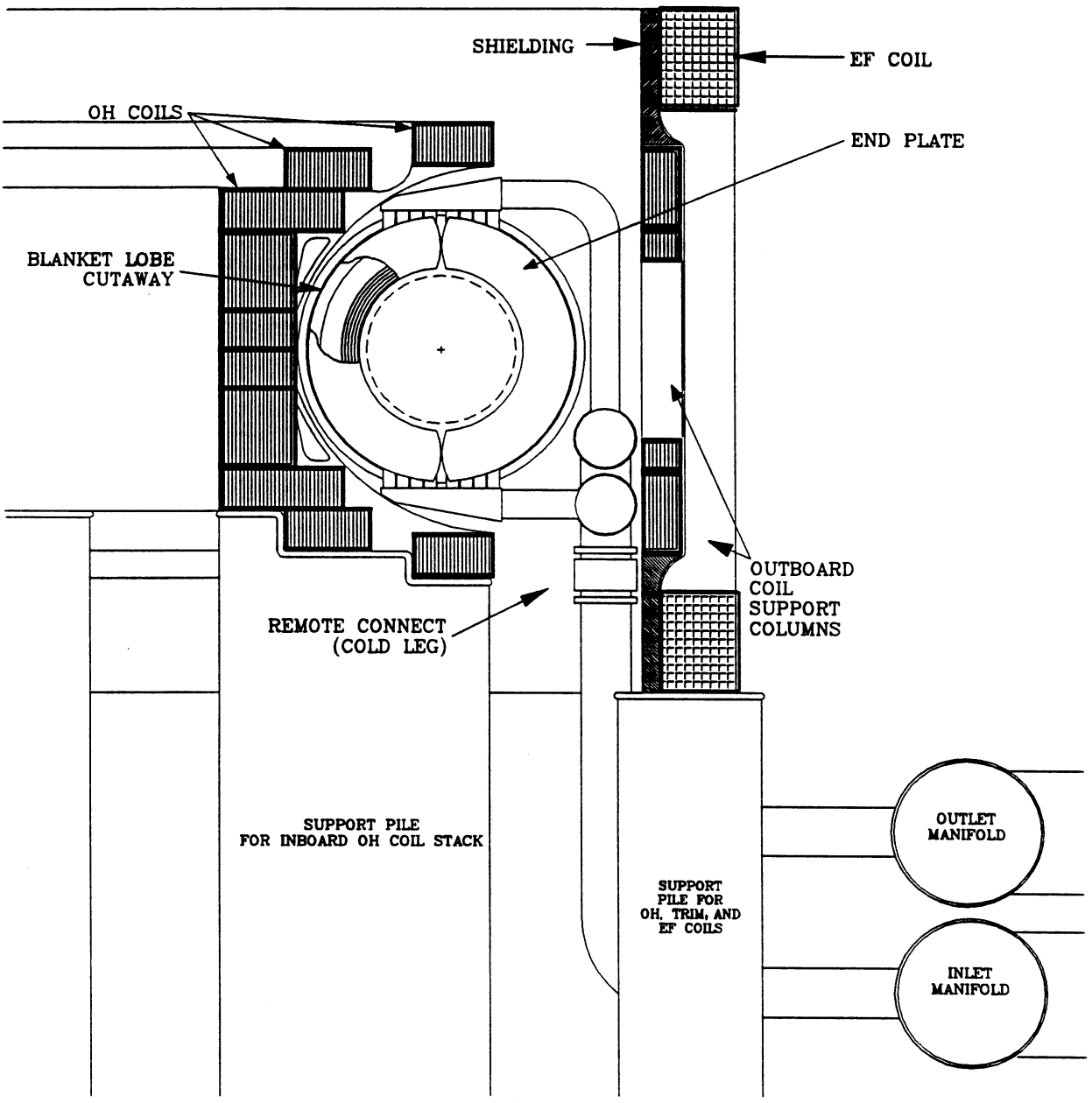

Figure 16.1-1. Poloidal cross section of the TITAN-II fusion power core.

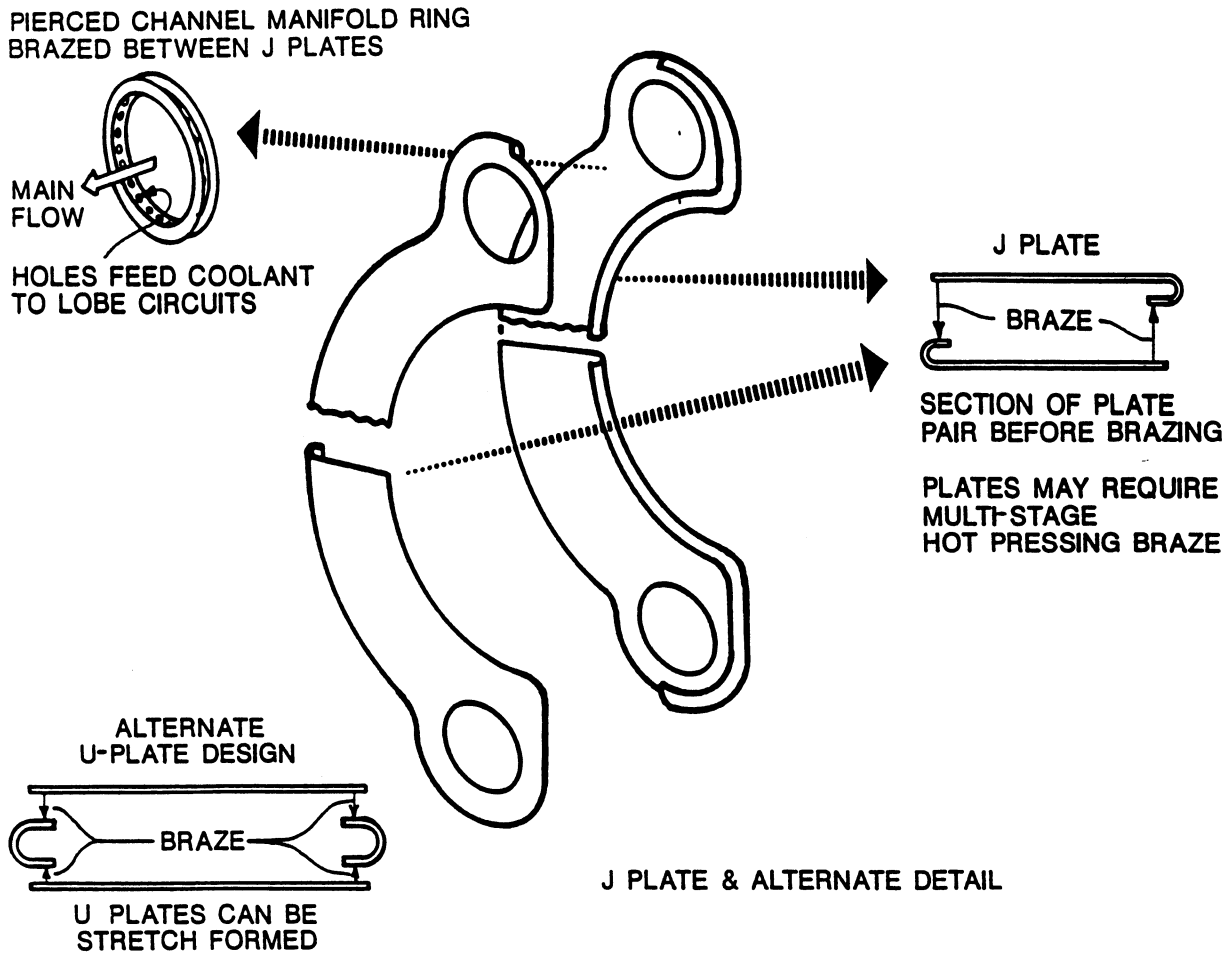

Figure 16.1-2. The TITAN-II blanket lobe, J-plate design.

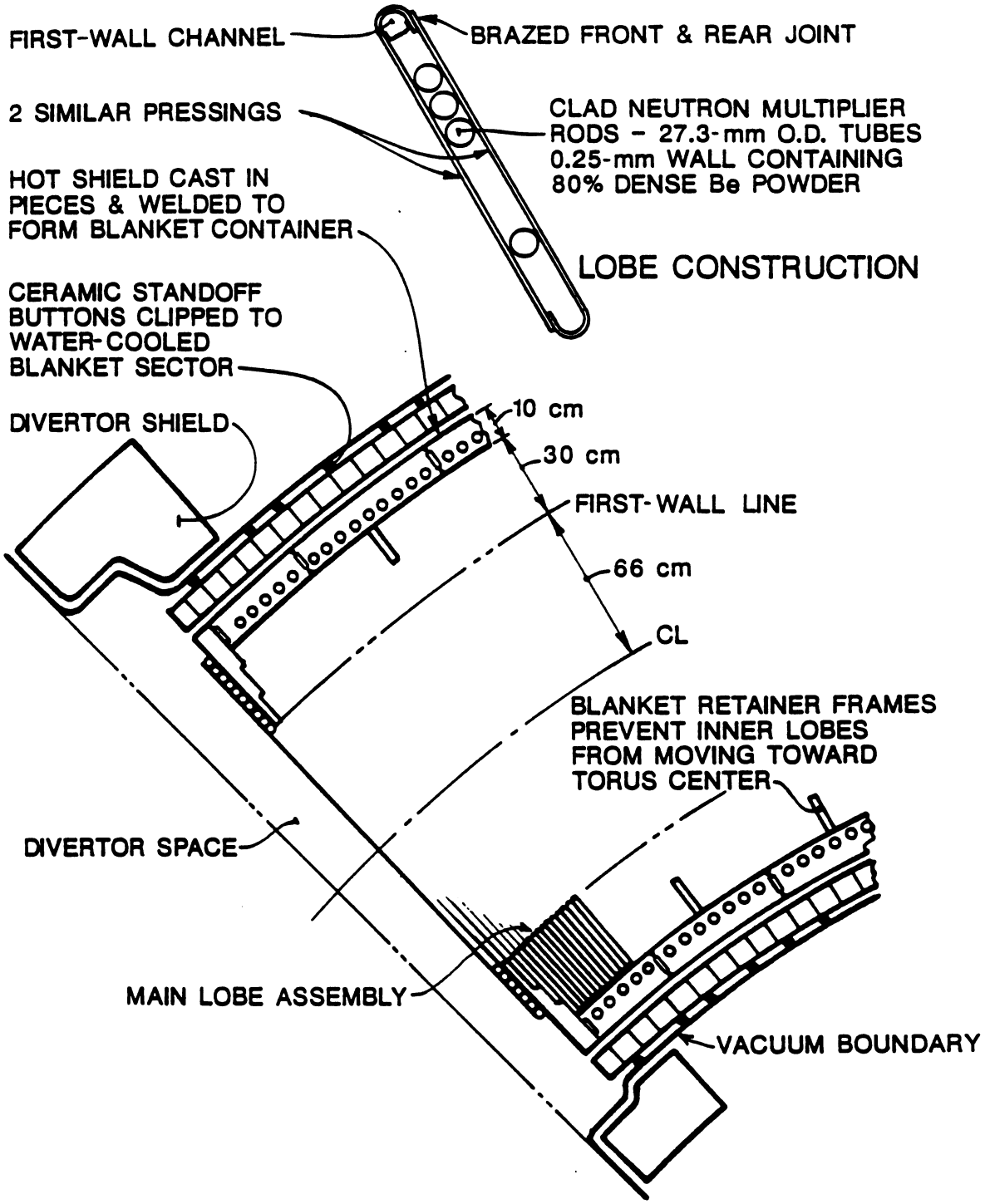

Figure 16.1-3. Equatorial-plane cross section of a TITAN-II blanket module.

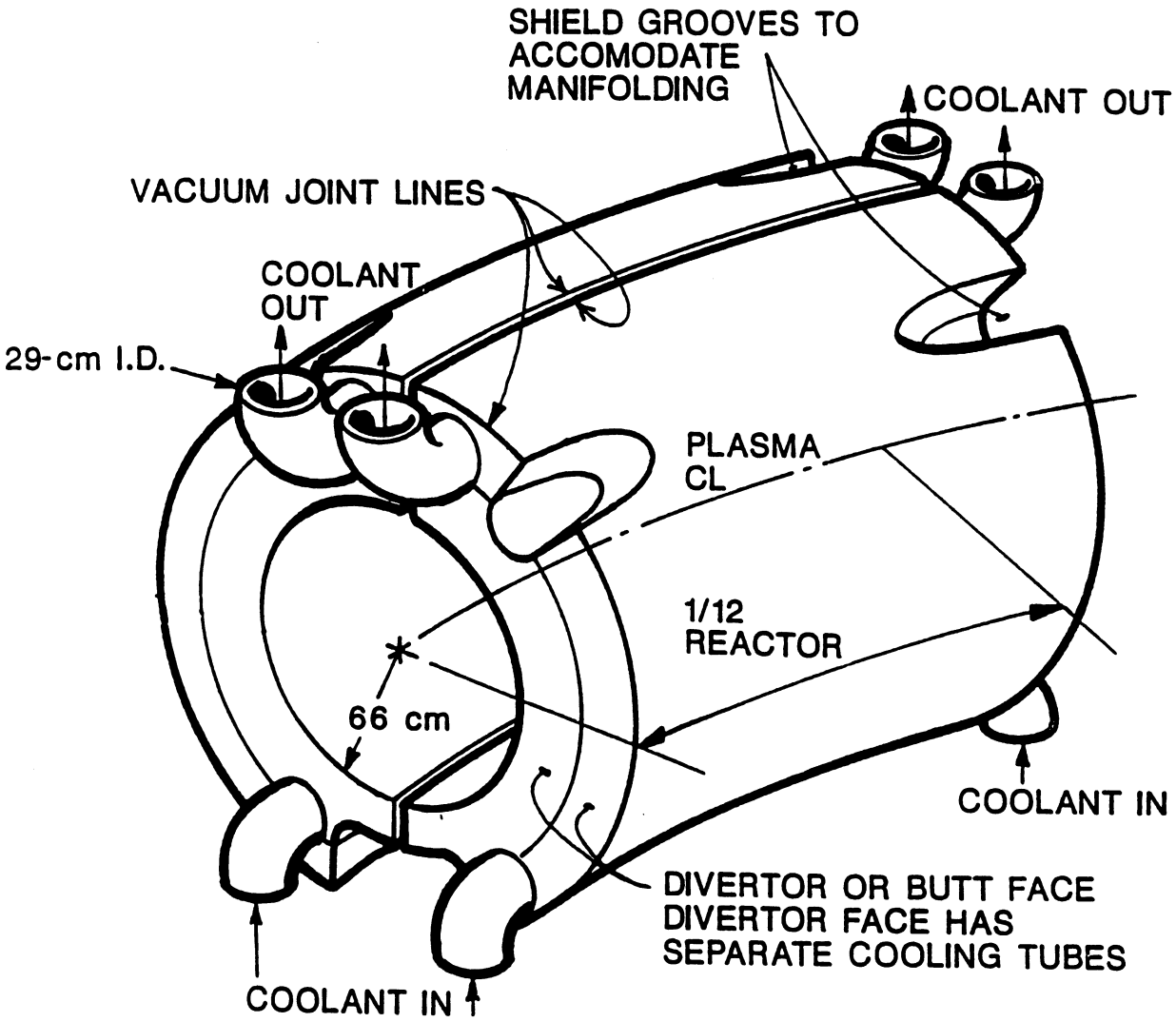

Figure 16.1-4. Isometric view of a TITAN-II blanket module.

tenance) are presented in subsequent sections. The engineering aspects of TITAN-II magnets are not covered because these magnets are based on present-day technology. Furthermore, TITAN-II magnets are, in principle, similar to those of the TITAN-I design except that water is used to cool the TITAN-II ohmic-heating (OH) coils instead of helium gas which cools the TITAN-I OH coils (Section 10.5).

The emphasis of the TITAN study has been on the investigation and demonstration of the feasibility of the compact, high-power-density reactors and also the identification of the critical issues for these devices. Therefore, some of the engineering issues that were not considered crucial to the design were for the most part not covered in detail in this study.

16.2. MATERIAL SELECTION

The attractiveness of commercial fusion-power devices depends, to a large extent, on material performance. Components of a fusion reactor are exposed to a unique set of stress, thermal, radiation, electromagnetic, and chemical loads and should function properly for the duration of the design lifetime. Material options are even more limited for a compact, high-power-density reactor such as TITAN because of high heat and radiation fluxes. The following sections will highlight various material selection issues for the TITAN-II FPC components.

The material issues in an aqueous-solution-cooled fusion reactor are quite different from those of a liquid-lithium-cooled FPC such as the TITAN-I design. The most significant differences between water-cooled and liquid-metal-cooled devices arise from the much higher coolant pressure in the water-cooled system, the electrochemical corrosion mechanisms of aqueous solutions, and the radiolysis of water by ionizing radiation.

In the TITAN-II design, tritium breeding is accomplished in a lithium salt which is dissolved in the primary coolant (water). Both lithium-hydroxide (LiOH) and lithium-nitrate ($LiNO_3$) salts were considered because they are highly soluble in water. The $LiNO_3$ salt was selected as the reference salt material because: (1) LiOH is more corrosive than $LiNO_3$ (Section 16.2.1), and (2) radiolytic decomposition of water which results in the formation of highly corrosive substances is minimized when nitrate salts are added to water. The nitrates act as scavengers reducing the probability of survival of highly reactive radicals in the water during exposure to radiation. The radiolysis of aqueous solutions in a fusion device has been acknowledged as a potential problem. A description of fundamental radiolytic processes and a literature survey of the radiolysis effects are

given in Section 16.2.2. The thermophysical properties of the aqueous solutions can be very different from those of pure water and are reviewed in Section 16.2.3.

The choice of aqueous lithium-salt solution as the primary coolant requires a structural material capable of withstanding the combined corrosive and irradiation environment of the FPC. Furthermore, one of the goals of the TITAN study has been to satisfy Class-C waste disposal criteria and achieve a Level-2 of safety assurance (Section 19). The requirement of low activation further constrains structural material choices. The vanadium allow, V-3Ti-1Si, is chosen as the structural material for the liquid-lithium-cooled TITAN-I design. But this alloy does not possess adequate water-corrosion resistance because of the lack of chromium content. Water corrosion resistance of most alloys results from the formation of a highly water-insoluble chromium-oxide layer. Chromium-containing vanadium alloys such as V-15Cr-5Ti have very good water corrosion resistance, however, their radiation behavior indicates a much higher susceptibility to helium embrittlement than other vanadium alloys (Section 10.2.2).

Among the ferrous alloys, the low-activation ferritic steel, 9-C [2], was identified as the most suitable structural material candidate for the TITAN-II design (Section 16.2.4). First, ferritic steels possess superior swelling resistance when compared to austenitic steels. In addition, with a high enough chromium content, the corrosion resistance of ferritics is comparable to that of chromium-rich austenitic steels. The available data on the effects of the $LiNO_3$ salt solution on corrosion of ferrous alloys are reviewed in Section 16.2.1. Hydrogen embrittlement of ferrous alloys has always been a concern, and therefore, Section 16.2.5 is devoted to this topic.

The TITAN-II design requires a neutron multiplier to achieve an adequate tritium-breeding ratio. Beryllium is the primary neutron multiplier for the TITAN-II design and the anticipated behavior of beryllium is presented in Section 16.2.6. The effects of radiation on the TITAN-II primary insulating material, spinel ($MgAl_2O_4$), have previously been discussed in Section 10.2. A detailed study of the lifetime of spinel for the TITAN-II radiation field was not performed, since small variations in the neutron spectrum would not markedly affect the radiation-damage response of spinel. Major findings are summarized in Section 16.2.7.

16.2.1. Corrosion in Aqueous Solutions

Corrosion has a far-reaching economic impact. It is estimated that the annual cost of corrosion and of corrosion protection is in the neighborhood of 8 billion dollars in the

United States [3]. Corrosion-related incidents appearing in piping and other components can impact plant availability, economics, reliability, and plant safety. Major corrosion-related problems encountered by the utility industry and nuclear-steam-system suppliers include the intergranular stress-corrosion cracking (IGSCC) of welded austenitic stainless-steel pipes in boiling-water reactors (BWRs) and the steam-generator corrosion in the pressurized-water reactors (PWRs) [4]. Despite the differences in operating conditions and coolant environments, the primary material problem for both BWRs and PWRs is stress-corrosion cracking (SCC).

Corrosion can be a uniform or localized (pitting) process. It is not uncommon for both forms of corrosion to occur at the same time, although one form usually predominates. Combined with other forms of attack such as erosion, fatigue, and SCC, corrosion can produce severe damage. Uniform attack may be rapid or slow and may leave the surface clean or coated with corrosion products. Uniform attack is easily evaluated and measurements are generally given in milligrams per square decimeter per day (mdd), in inches per year, or mils per year. Pitting corrosion, on the other hand, is difficult to evaluate and has to be measured by careful microscopic examination of a number of pits. Pits may start at an inclusion, a grain boundary, or at some other imperfection on the surface such as a dislocation.

The following subsections discuss the issues of corrosion by the aqueous salt coolant. A brief background on the electrochemical nature of corrosion is given first and some of the basic corrosion fundamentals are discussed (Section 16.2.1.1). Commonly used methods of mitigating corrosion are summarized in Section 16.2.1.2. Then, the data on SCC are reported and recent results of SCC mitigation efforts in the nuclear industry are summarized in Section 16.2.1.3. The corrosion issues of ferritic and austenitic steels in nitrate-salt solutions are discussed in Section 16.2.1.4. The effects of hydrogen and oxygen on corrosion and cracking are reviewed separately in Section 16.2.5.

16.2.1.1. Electrochemical nature of corrosion

Most metals exist in a combined state in nature and some energy has to be exerted to bring the metals into the metallic state. Thus, the metallic state represents a high-energy state of the metal and all metals tend to revert to a lower-energy state by combining with other substances, accompanied by release of energy. This decrease in free energy is the driving force of corrosion reactions. Grain boundaries, in particular, are high-energy areas, since the most stable configuration of the metal is its particular crystal structure. Grain boundaries constitute areas of lattice mismatch and are therefore slightly more

active chemically than the grain faces. The release of this stored mismatch energy leads to a higher corrosion attack along grain boundaries.

The change in the free energy by corrosion is mathematically related to the electromotive force (EMF) of the reaction. An electrochemical-corrosion reaction can be divided into anodic and cathodic parts, each with its own potential. Any reaction that can be divided into two or more partial reactions of oxidation and reduction is termed an electrochemical process. For example, in the anodic part, "oxidation" of a metal to form metal ions and free electrons takes place, while in the cathodic part, "reduction" of the metal ion to a metal occurs. The difference in these potentials is the EMF of the overall reaction which provides the driving force of corrosion.

The anodic reaction occurring during corrosion processes is the oxidation of a metal to its ion. However, the cathodic reactions can involve the reduction of hydrogen, oxygen, or metal. Examples of possible reduction equations in aqueous solutions are given in Table 16.2-I. More than one oxidation and more than one reduction reaction may occur simultaneously during corrosion. For example, in oxygenated acidic solutions, the evolution of hydrogen and the reduction of oxygen can occur simultaneously. Thus, aerated acidic solutions tend to accelerate corrosion because of an increase in reduction reactions (higher consumption of electrons).

Table 16.2-I.

POSSIBLE REDUCTION EQUATIONS IN AQUEOUS SOLUTIONS

Hydrogen evolution	$2H^+ + 2e \rightarrow H_2$
Oxygen reduction (acid solutions)	$O_2 + 4H^+ + 4e \rightarrow 2H_2O$
Oxygen reduction (neutral, basic solutions)	$O_2 + 2H_2O + 4e \rightarrow 4OH^-$
Metal-ion reduction (to ions)	$M^{+3} + e \rightarrow M^{+2}$
Metal-ion reduction (to neutrals)	$M^+ + e \rightarrow M.$

Galvanic coupling

Galvanic coupling can occur when two dissimilar metals are in contact with the same corrosive medium (*e.g.*, zinc and platinum in an acidic solution). Platinum is inert (noble) and will not undergo anodic reactions (no dissolution). However, the addition of platinum effectively increases the area for hydrogen evolution (*i.e.*, the cathodic reaction area). Also, hydrogen evolution occurs much more readily on platinum than on zinc, resulting in an increased cathodic reaction rate (higher hydrogen production). Since the anodic reaction rates are coupled to the cathodic reaction rates, an increase in one rate results in an increase of the other. Consequently, more zinc has to be dissolved to keep up with the increase in electron consumption because of hydrogen evolution on the platinum surface. Thus, platinum has effectively increased the oxidizing power of the solution (*i.e.*, consumption of electrons).

Most alloys are either solid-solution or heterogeneous. In solid-solution alloys (*e.g.*, stainless steels), the alloying elements are fully soluble in each other, while in heterogeneous alloys (*e.g.*, low-carbon steels) different phases can form because of the alloying elements. The presence of different phases in heterogeneous alloys can also lead to galvanic-coupling effects (*i.e.*, to an increase in corrosion rates). This is one of the reasons that solid-solution alloys are generally more corrosion resistant than heterogeneous alloys.

Because of phase formations in many alloys, the use of the standard EMF series to determine galvanic coupling between alloys can be misleading. Therefore, measurements have been made using common alloys to determine galvanic series, as shown in Table 16.2-II, which are based on potential measurements and galvanic corrosion tests in unpolluted seawater by The International Nickel Company at Harbor Island, N.C. [3]. It should be noted that galvanic coupling does not always lead to an increase in corrosion rates and in some cases it can lead to a decrease.

Polarization

Electrochemical reactions can be polarized or retarded by various physical or chemical environmental factors. Two types of polarization have been identified, activation and concentration, and both lead to decreased corrosion rates by reducing the rate of cathodic reactions. The polarization mechanism can be described by considering the hydrogen evolution in the water. Generally hydrogen ions diffuse through the fluid to the metal surfaces, are adsorbed to the surface, and pick up electrons to form atoms. In the

Table 16.2-II.

GALVANIC SERIES OF COMMERCIAL ALLOYS IN SEAWATER[a] [3]

↑ Noble or Cathodic	• Platinum
	• Gold
	• Graphite
	• Titanium
	• Silver
	• Chlorimet 3 (62 Ni, 18 Cr, 18 Mo)
	Hastelloy C (62 Ni, 17 Cr, 15 Mo)
	• 18-18 Mo stainless steel (passive)
	18-8 stainless steel (passive)
	Chromium stainless steel 11%-30% Cr (passive)
	• Inconel (passive) (80 Ni, 13 Cr, 7 Fe)
	Nickel (passive)
	• Silver solder
	• Monel (70 Ni, 30 Cu)
	Cupronickels (60-90 Cu, 40-10 Ni)
	Bronzes (Cu-Sn)
	Copper
	Brasses (Cu-Zn)
	• Chlorimet 2 (66 Ni, 32 Cr, 1 Fe)
	Hastelloy B (60 Ni, 30 Mo, 6 Fe, 1 Mn)
	• Inconel (active)
	Nickel (active)
	• Tin
	• Lead
	• Lead-tin solders
	• 18-18 Mo stainless steel (active)
	• 18-8 stainless steel (active)
	• Chromium stainless steel, 13% Cr (active)
	• Cast iron
	Steel or iron
	• 2024 aluminum (4.5 Cu, 1.5 Mg, 0.6 Mn)
Active or Anodic ↓	• Cadmium
	• Commercially pure aluminum (1100)
	• Zinc
	• Magnesium and magnesium alloys

(*a*) Seawater is generally oxygenated and slightly acidic.

activation polarization process, the hydrogen atoms diffuse along the metal surface and two hydrogen atoms eventually combine to form a molecule which leaves the surface. Usually, the surface diffusion of hydrogen atoms is the rate-limiting process. In the concentration polarization process, the hydrogen atoms leave the surface to combine with another hydrogen atom inside the fluid and form a molecule (surface diffusion of hydrogen is not required). The factor that controls the hydrogen evolution rate is the diffusion of hydrogen ions through the fluid to the metal surface and, therefore, the hydrogen reduction rate is limited by hydrogen-ion concentrations. This type of polarization occurs mostly in dilute acids or in aerated, dilute salt solutions.

From the point of view of corrosion prevention, the distinction between activation and concentration polarizations is important. In the case of concentration polarization, environmental changes that lead to an enhancement of the diffusion of hydrogen ions to the metal surface (*e.g.*, velocity, agitation, and temperature) will reduce polarization and will cause an increase in the corrosion rate. Activation polarization, on the other hand, will not be affected by similar environmental changes.

Passivation

Under certain environmental conditions, some metals can become essentially inert and behave like noble metals. As the oxidizing power (consumption of electrons) of a solution increases, the anodic reactions (transforming metal atoms into their ions) also increase and result in a higher corrosion rate. In this "active" state, the corrosion rate increases exponentially. Increasing the oxidation power of the solution beyond a characteristic threshold value, however, will "passivate" the metal. Most common engineering metals are susceptible to passivation. Stainless steel and titanium, for example, are easily passivated metals.

In the passive state, the metal will show a sudden decrease in the corrosion rate. During the transition from the active to the passive region, a 10^3 to 10^6 reduction of the corrosion rate is usually observed. The precise processes responsible for this passivation and sudden decrease in corrosion are not known. It is, however, speculated that some form of activation polarization is producing a film on the metal surface which is stable over a considerable range of oxidation power of the solution [5]. Further increases in the oxidizing power of the solution to very high levels will eventually break down the protective film and corrosion again proceeds at about the same rate as during the active state. This latter state is termed "trans-passive." Active-passive characteristics are shown in Figure 16.2-1.

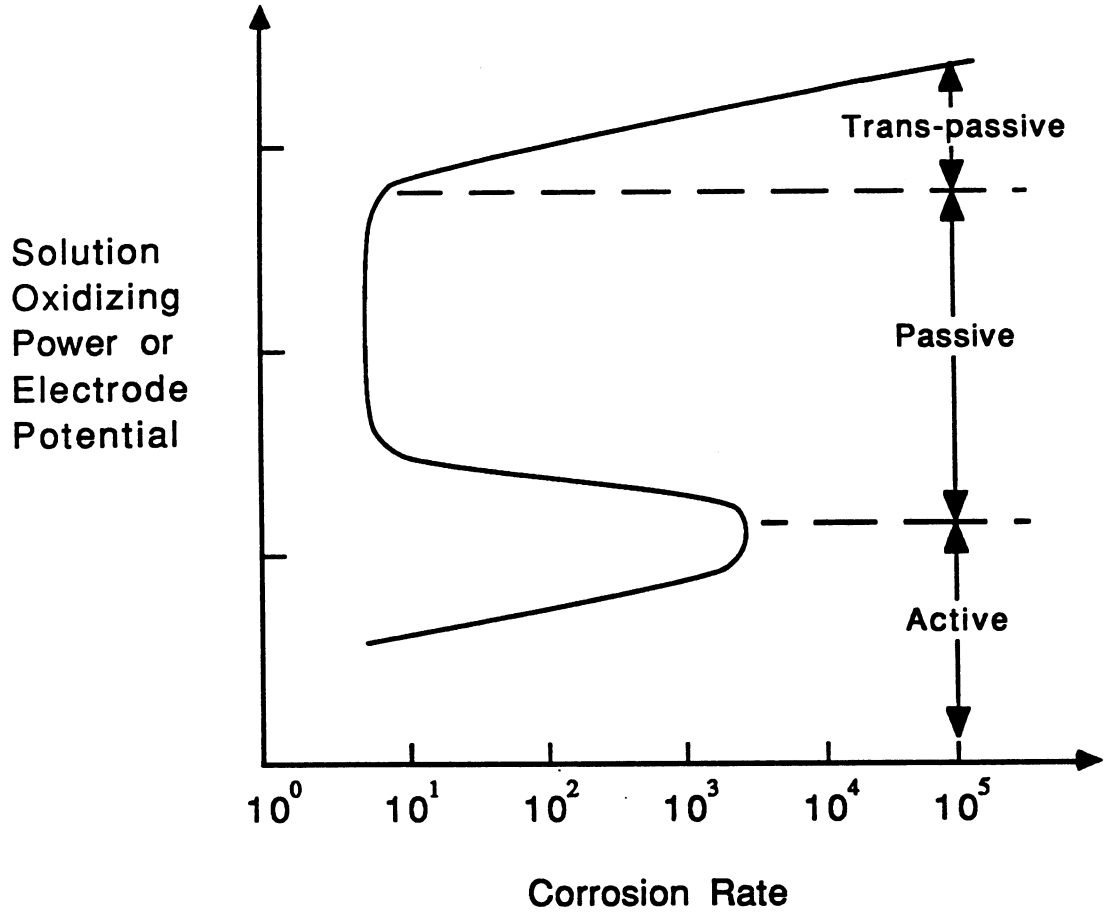

Figure 16.2-1. Corrosion characteristics of an active-passive metal as a function of the oxidizing strength of the solution [3].

Potentiodynamic polarization curves

Electrochemical studies called "potentiodynamic polarization" tests are routinely conducted to obtain mechanistic information on the corrosion rates. These tests measure the current density versus an applied potential. Results of these tests are usually shown as the potentiodynamic polarization curves (PPCs) similar to Figure 16.2-2. In a corrosion process, the rate constant can be replaced by an equivalent value of the polarizing current density [6].

Typically, the PPCs show three major zones where the current density increases, distinguishing two passive ranges. The first and second zones are called, respectively, the primary and the secondary passivation zones (Figure 16.2-2). In the passive zones, the current density remains fairly constant over a wide range of potentials. The corrosion

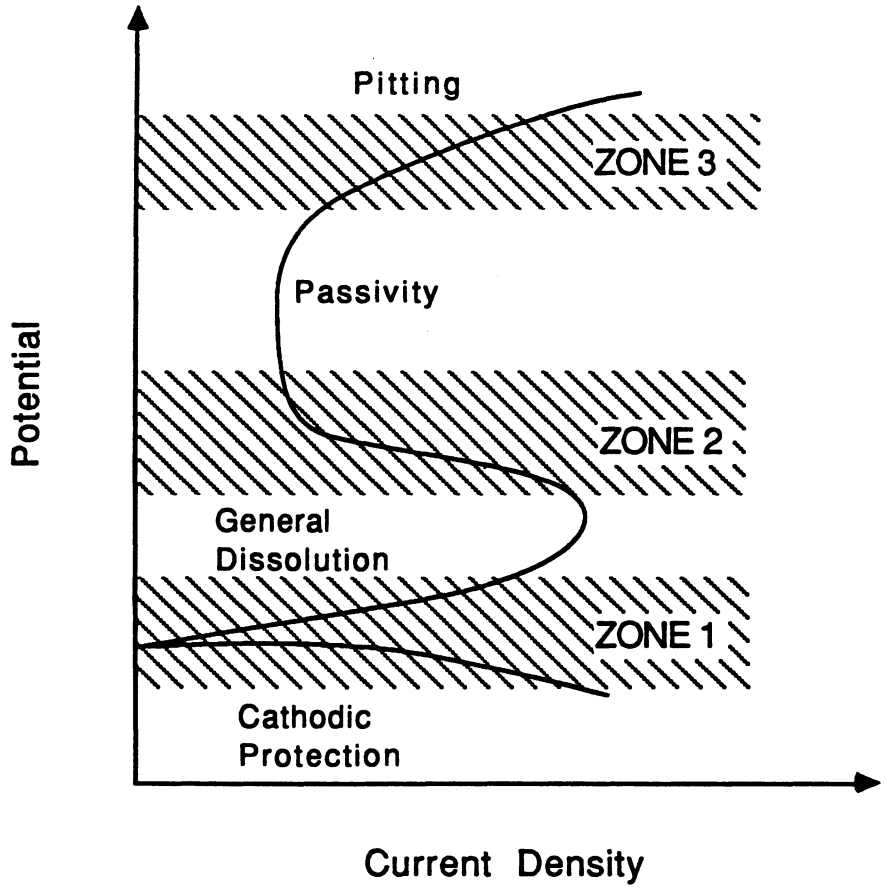

Figure 16.2-2. A typical potentiodynamic polarization curve (PPC).

rates in these passive zones are generally quite low. The transition zone between two passive zones is usually very susceptible to corrosion believed to be associated with the dissolution of one of the alloying elements. For example, chromium has been shown to play a significant role in corrosion processes in steels and chromium-enriched grain boundaries have been determined to be the major reason for the primary passivation zone on the PPCs [3].

At potentials much higher than those that cause the secondary passivation, the current density increases very sharply. This zone is associated with very rapid corrosion, such as pitting or the onset of gaseous oxygen formation by the electrolysis of water. It should be noted that the PPCs do not indicate the corrosiveness of material, only the spontaneity of corrosion processes.

Effects of temperature and oxygen concentration

It is found that corrosion processes and rates often depend strongly on the thermal history of the alloy. Chromium additions above $\sim 10\,\text{wt.}\%$ to steel are responsible for most of the corrosion resistance of steels. At temperatures above $\sim 950\,^{\circ}\text{C}$, the chromium content along grain boundaries is effectively lowered through the formation of $Cr_{23}C_6$ molecules. These chromium carbides are virtually insoluble and precipitate out of solid solution, resulting in a depletion of solid-solution chromium and carbon. These steels are found to be susceptible to intergranular corrosion and are said to have become sensitized (the reduction in chromium sensitizes the grain boundaries to corrosive media).

Oxidation reactions play an important role in the corrosion process. A measure of the corrosiveness is the corrosion potential as a function of oxygen concentration that determines which corrosion reaction is favored thermodynamically. Stress-corrosion cracking (SCC) of sensitized stainless steel under boiling-water-reactor (BWR) conditions [7 - 9], rippling in boiler tubes [10,11], and erosion-corrosion on unalloyed steels [12] are some examples which are correlated to oxygen/corrosion potential.

The corrosion potential for stainless steels has been measured as a function of temperature and typical values of the oxygen content of the boiler water [14]. Figure 16.2-3 shows the values of the corrosion potential of AISI 304 SS as a function of oxygen concentration in high purity water [7]. Although the values of corrosion potentials are not fully identical for various experiments, in general, the potential increases from about $-600\,\text{mV}$ at zero oxygen content to about $+50$ to $100\,\text{mV}$ at 10,000 ppb (parts per billion) of oxygen (Figure 16.2-3). The larger the potential value, the higher will be the anodic character of the metal (the electron sink strength is increased), causing a higher oxidation rate of the iron into Fe^{+2} ions. Highly negative corrosion potentials correspond to very low corrosion rates. While an increase in the oxygen content increases the corrosion potential, an increase in temperature decreases the potential for oxygen content in the range of 10 to 1,000 ppb in stainless steels (Figure 16.2-3).

16.2.1.2. Corrosion prevention

Mitigation of corrosion is possible by proper material selection, altering the environment, using corrosion inhibitors, and by using protective coatings. Some of these preventive measures are discussed below. The use of protective coatings, however, is not included because the stability of a particular coating in the TITAN-II nuclear environment should first be demonstrated.

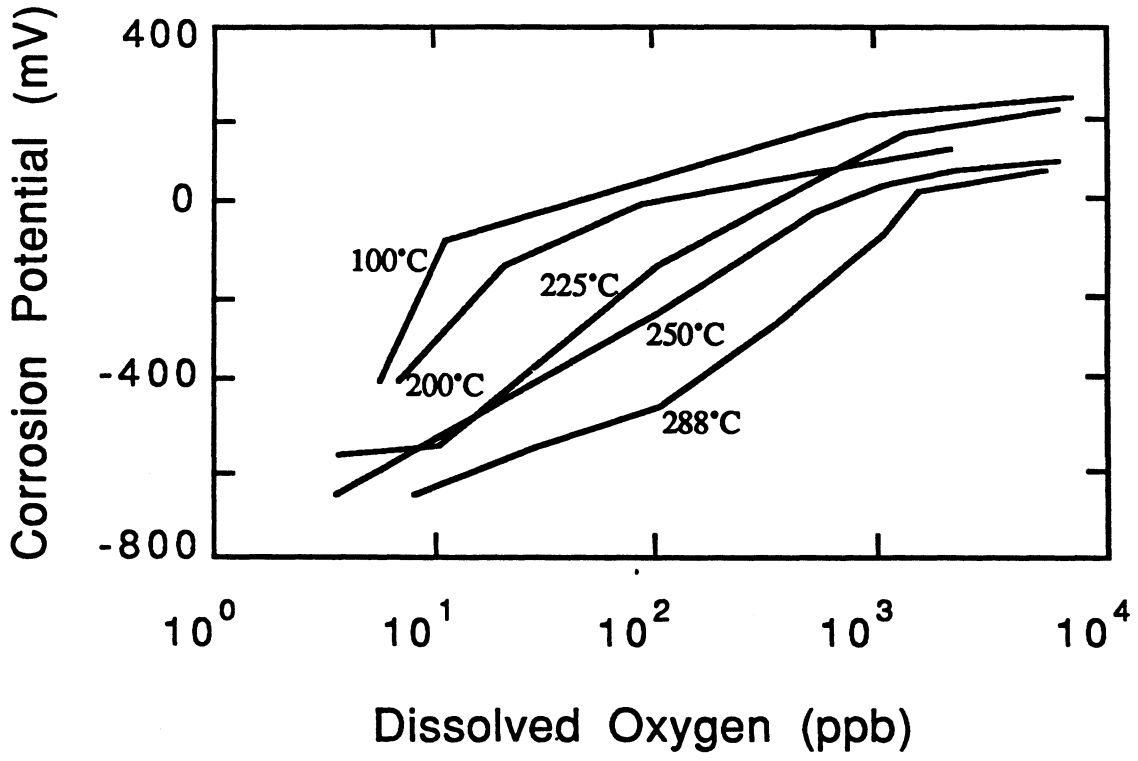

Figure 16.2-3. The corrosion potential of AISI 304 SS as a function of oxygen concentration at different temperatures in high-purity water [13].

Material Selection

The most important method of corrosion prevention is the selection of the proper material for a given environment. Stainless steels are frequently chosen as one of the primary structural materials. Under certain conditions (*e.g.*, chloride-containing mediums and stressed structures), however, stainless steels are less resistant than ordinary structural steel [15]. Also, stainless alloys are more susceptible to localized corrosion such as intergranular corrosion, stress-corrosion cracking, and pitting attack than ordinary structural steels [15]. On the other hand, stainless steels are found to have excellent resistance to nitric acid under a wide range of exposure conditions (the TITAN-II FPC is cooled by an aqueous $LiNO_3$ solution).

In general, for oxidizing conditions, chromium-containing alloys are used. For reducing environments (air-free acids and aqueous solutions), nickel, copper, and their alloys show good corrosion resistance. The most corrosion-resistant material is tantalum which resists most acids at all concentrations and temperatures.

To guide the material selection, corrosion engineers have lists of "natural" metal-corrosive combinations such as [3]:

- Nickel and nickel alloys – caustic,
- Monel – hydrofluoric acid,
- Hastelloys – hydrochloric acid,
- Lead – dilute sulfuric acid,
- Aluminum – nonstaining atmospheric exposure,
- Tin – distilled water,
- Titanium – hot strong oxidizing solutions,
- Tantalum – ultimate resistance,
- Stainless steels – nitric acid,
- Steel – concentrated sulfuric acid.

Altering the environment

Depending on the system, the corrosion rate can be drastically affected by physical changes in the environment (*e.g.,* temperature, velocity, and oxidizer concentration).

Temperature. Lowering the temperature usually results in a sharp decrease in the corrosion rates. In some cases, however, lowering the temperature may have the opposite effect. For example, increasing the temperature of pure or seawater from hot to boiling decreases the oxygen solubility in water and causes a decrease in the corrosion rate.

Velocity. The effects of velocity on corrosion are very complex and are highly dependent on the metal-environment combination. In corrosion processes that are controlled by activation polarization, velocity has little effect on the corrosion behavior (Section 16.2.1.1). On the other hand, when the corrosion rate is controlled by cathodic diffusion, then velocity or agitation will lead to an increase in the corrosion rate. If cathodic diffusion prevails and the metal is readily passivated, then an increase in velocity

can result in an active-to-passive transition (Section 16.2.1.1). Stainless steels and titanium, for this reason, are often more corrosion resistant when the velocity of the corrosive medium is high.

Some materials will form visible protective corrosion layers that retard any further corrosion. These films are unlike the passivation films and can be damaged and removed by high-velocity medium flow. This type of corrosion falls under the category of "erosion-corrosion" and can be highly velocity dependent. An increase in the velocity may have no effect or slightly increase the corrosion rate until a "critical" velocity is reached. Further increase in the velocity will result in a drastic increase in the erosion-corrosion rate. Table 16.2-III shows typical corrosion rates at three velocities for some common alloys.

Increased velocities may, in some cases, lead to a decrease in corrosion by preventing silt deposition. This is only true when silt or dirt buildup causes "crevice" corrosion. Crevice corrosion is a form of attack primarily associated with small volumes of stagnant solution caused by crevices under bolts and rivet heads, gaskets, surfaces, lap joints, surface deposits, and holes. The main cause of crevice corrosion is believed to be the depletion of oxygen in the trapped and stagnant fluid. Crevice corrosion is a serious problem and methods and procedures for minimizing it include the use of welded butt joints instead of riveted or bolted joints, closing of crevices in existing lap joints by continuous welding, and by frequent removal of deposits.

Oxidizers. Removing oxidizers is a very old corrosion-control technique. Techniques for removing oxygen include vacuum treatment, inert gas sparging, or the use of oxygen scavengers. Examples of oxygen scavengers include sodium sulfite and hydrazine which remove oxygen as indicated by the following reactions:

$$2Na_2SO_3 + O_2 \rightarrow 2Na_2SO_4\,, \tag{16.2-1}$$

$$N_2H_4 + O_2 \rightarrow N_2 + 2H_2O\,. \tag{16.2-2}$$

Monel and copper exhibit a distinct increase in the corrosion rate when oxidizers are added to acid solutions. Neither of these materials passivate. However, materials that require oxidizers to form and maintain a protective film would show an increase in the corrosion rate if deaeration was performed. For example, when oxidizers are added to the solution, active-passive alloys such as 18Cr-8Ni stainless steels experience an increase, followed by a rapid decrease, and finally arrive at an oxidizer-concentration-independent corrosion rate.

Table 16.2-III.

CORROSION RATES OF METALS EXPOSED TO SEAWATER[a]

Material	Seawater Flow Velocity					
	1 ft/s[b]		4 ft/s[c]		27 ft/s[d]	
Carbon steel	34	(0.16)	72	(0.33)	254	(1.18)
Cast iron	45	(0.23)	–		270	(1.37)
Silicon bronze	1		2		343	
Admiralty brass	2		20		170	
Hydraulic bronze	4		1		339	
G bronze	7		2		280	
Al bronze (10% Al)	5	(0.02)	–		236	(1.1)
Aluminum brass	2		–		105	
90-10 Cu Ni (0.8% Fe)	5	(0.02)	–		99	(0.40)
70-30 Cu Ni (0.05% Fe)	2	(0.008)	–		199	(0.81)
70-30 Cu Ni (0.5% Fe)	< 1	(0.004)	< 1		39	(0.16)
Monel	< 1	(0.004)	< 1		4	(0.017)
316 SS	1	(0.004)	0		< 1	
Hastelloy C	< 1	(0.009)	–		3	(0.028)
Titanium	0		–		0	

(*a*) Corrosion rates are given in mdd (mg/dm^2) and in mm/y (values in parenthesis).

(*b*) Immersed in tidal current.

(*c*) Immersed in seawater flume.

(*d*) Attached to immersed rotating disk.

The effects of oxygen on corrosion rates depend on both the medium and the metal used. Nesmeyanova *et al.* [16] showed that the addition of oxygen markedly increased the corrosion of low-alloy steels (having less than 12% total alloy content) and stainless steels in distilled water at 300 °C, while Maekawa *et al.* [17] and Ito *et al.* [18] found that the corrosion rate of austenitic stainless steel is generally greater in deaerated (oxygen free) water than in air-saturated water.

More recently, the role of dissolved oxygen on the corrosion behavior of mild and stainless steel in aqueous solutions at temperatures above 100 °C were studied by Fujii *et al.* [19]. They concluded that: (1) The passivity which appeared in deaerated solutions was caused by the formation of a protective magnetite film. On the other hand, the rather poorly protective oxide obtained under air-saturated conditions was identified as α-Fe_3O_3 together with small amounts of Fe_3O_4. (2) The corrosion potential of stainless steel was raised into the trans-passive state (higher corrosion rates) with increased temperature and amount of dissolved oxygen. (3) The pitting of stainless steel in high-temperature water containing chloride ions is attributable to the effect of dissolved oxygen. These results show that removal of oxygen at high operating temperatures is beneficial in minimizing corrosion of stainless steels.

Corrosion inhibitors

Another corrosion-control technique is the addition of "corrosion inhibitors" to the solution. The most commonly used are adsorption-type inhibitors which suppress metal dissolution by adsorbing to the surface and thereby reduce both anodic and cathodic processes. The majority of inhibitors are organic amines (*e.g.*, glycine, lysine, and tryosine). Hydrogen-evolution poisons (*e.g.*, antimony and arsenic ions) are very effective as corrosion inhibitors for acid solutions because they retard hydrogen evolution. In closed spaces such as the interior of machine rooms, vapor-phase inhibitors are sometimes applied. These inhibitors consist of high-vapor-pressure organic substances that are put in the vicinity of surfaces to be protected and act similar to adsorption-type inhibitors by building protective layers through sublimation on surfaces.

Inhibitors have to be chosen specifically for a certain metal, environment, concentration, and temperature range. Lists of appropriate inhibitors and their application ranges have been compiled and are available [20]. Table 16.2-IV lists some of the reference inhibitors. Only nitrite and nitrate inhibitors are listed to point out their corrosive-inhibiting potentials for use in reactor designs.

The types and quantities of inhibitors to be used have to be determined empirically. Corrosion processes are very sensitive to the operating conditions. It is particularly important to determine the exact amounts of inhibitors to be used because too little can often lead to an increase in the localized attack (rather than prevent it). The general rule of corrosion engineers is to use inhibitors in abundance. In some cases, two or more inhibitors are added, resulting in a larger reduction in the corrosion rate than if these inhibitors were used individually. One such "synergistic" corrosion-inhibiting effect has been well documented for nitride and molybdate ions. Sodium nitride has long been used to inhibit ferrous-metal corrosion in closed cooling systems [21]. Sodium molybdate was

Table 16.2-IV.

REFERENCE LIST OF CORROSION INHIBITORS

Metal	Environment	Inhibitor
Aluminum	Alcohol antifreeze	Sodium nitrite or molybdate
Aluminum	Ethylene glycol	0.01% to 1.0% sodium nitrate
Aluminum	Hydrogen peroxide	Alkali metal nitrates
Aluminum	Methyl alcohol	Sodium nitrite or chromate
Copper & brass	Tetrahydrofurfuryl alcohol	1% sodium nitrate or 0.3% sodium chromate
Monel	Sodium chloride	0.1% sodium nitrite
Monel	Tap water	0.1% sodium nitrite
Steel	Tetrahydrofurfuryl alcohol	1% sodium nitrite or 0.3% sodium chromate
Steel	Water-saturated hydrocarbons	Sodium nitrite
Tin plate	Alkali cleaning agents	Diethylene diaminocobaltic nitrate
Tin plate	Alkaline soap	0.1% sodium nitrite
Tin plate	Sodium chloride	0.2% sodium nitrite

also shown to be an effective corrosion inhibitor of steel in aerated open or fully closed cooling-water systems [22]. Table 16.2-V indicates the individual corrosion-inhibiting effects of NO_2^- and MoO_4^{-2} ions of a fairly corrosive media. The test water contained 250 mg/l chloride, 520 mg/l sulfate, 250 mg/l calcium and 15 mg/l magnesium at 60 °C.

Recently, it was shown that sodium nitride interacts synergistically with sodium molybdate [21]. Figure 16.2-4 shows the synergistic effect on the corrosion rate. The synergistic interaction of the two inhibitors is evident at all of the weight ratios of MoO_4^{-2}/NO_2^-, with optimum synergism occurring at inhibitor ratios ranging from 50/450 to 250/250 mg/l. The PPC of MoO_4^{-2}/NO_2^- system were studied and it was found that the current densities in each of the passive regions were lower than the corresponding passive current densities with either molybdate or nitride ions used separately. The primary passive region near -500 mV is attributed to molybdate, while the secondary passive region near 0 mV results from nitride.

16.2.1.3. Stress-corrosion cracking

During stress-corrosion cracking (SCC), a metal is virtually unattacked over most of its surface while fine cracks progress through the bulk of the material. The alloy becomes brittle with little or no macroscopic plastic deformation. Although many alloys are susceptible to SCC in at least one environment, SCC does not occur in all environments. Moreover, an environment that induces SCC in one alloy does not necessarily induce SCC in another. Stress-corrosion cracking has serious consequences since it can occur at stresses within the range of typical design stresses. Stress-corrosion cracking can occur both in transgranular (across grains) or intergranular (between grains) modes. Intergranular stress-corrosion cracking (IGSCC) is found to be the dominant failure mechanism in sensitized austenitic stainless steels, while transgranular SCC (TGSCC) has been reported to occur primarily in ferritic and low-alloy steels [23]. Three requirements must be fulfilled simultaneously for SCC to occur: (1) the steel must be sensitized, (2) the steel must be under tensile stress, and (3) the environment must have specific corrosion properties (*e.g.*, oxygen).

The typical oxygen content in BWRs during full-power operation is about 200 to 400 ppb. The source of oxygen is the radiolysis of water in the reactor core. Oxygen contents that result in corrosion potentials below -300 mV have been shown not to produce any IGSCC [7]. This corresponds to an oxygen content of not more than 10 ppb at temperatures above 200 °C (Figure 16.2-3). Operating a BWR at full power with less

Table 16.2-V.

CORROSION RATE OF SAE 1010 STEEL[a]

Test Water[b]	Oxygen Concentration (mg/l)			
	0	1	2.5	5
Uninhibited	0.1 (0.00)	6.6 (0.17)	16.3 (0.41)	40.1 (1.02)
500 mg/l MoO_4^{-2}	0.1 (0.00)	5.0 (0.13)	12.8 (0.32)	1.7 (0.04)
1000 mg/l MoO_4^{-2}	0.1 (0.00)	4.1 (0.10)	7.6 (0.19)	1.9 (0.05)
500 mg/l NO_2^-	0.1 (0.00)	4.9 (0.12)	8.6 (0.22)	9.6 (0.24)
1000 mg/l NO_2^-	0.1 (0.00)	0.5 (0.01)	0.4 (0.01)	0.4 (0.01)

(*a*) Corrosion rates are given in mils per year and in mm/y (values in parenthesis).

(*b*) Uninhibited and inhibited test water at 60 °C and a pH of 9.

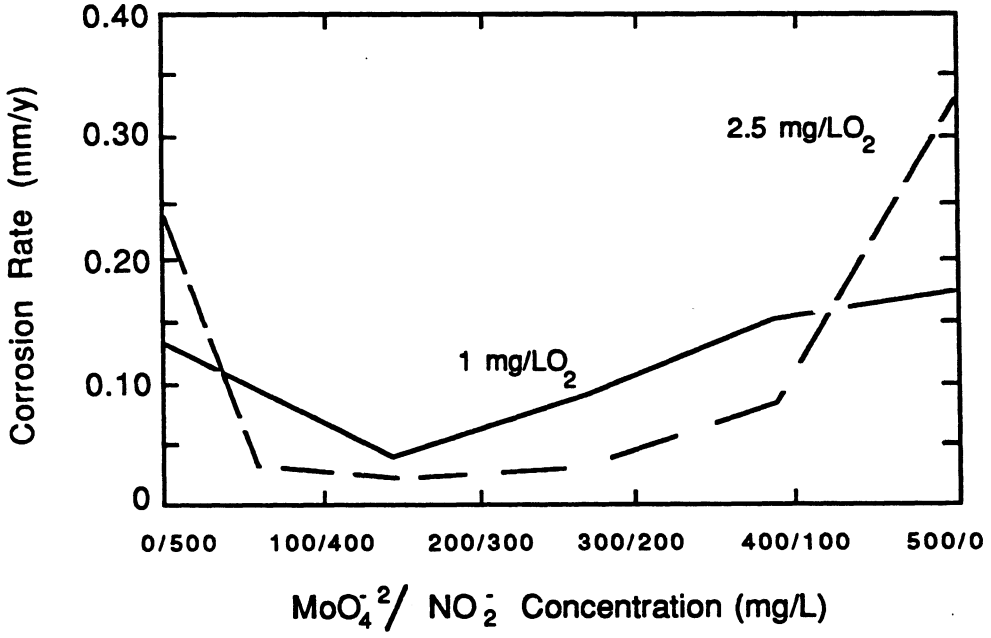

Figure 16.2-4. Corrosion rate of SAE 1010 steel in 60 °C test water showing the synergistic effect on corrosion inhibition with MoO_4^{-2}/NO_2^- combinations.

than 10-ppb oxygen content was achieved in the Swedish reactor OSKARSHAMM-2 [24]. The oxygen content was kept at 3 to 5 ppb by the addition of hydrogen to the feed water.

The Swedish researchers [23] were able to correlate IGSCC average crack-propagation rates to the corrosion potential at low strain rates (5×10^{-8} s^{-1}). The tests were conducted on austenitic stainless steels at 275 °C. For oxygen contents of about 400 ppb, the crack-propagation rate was around 5×10^{-6} mm/s while for tests with oxygen contents less than 10 ppb, the propagation rate was as low as 10^{-7}mm/s. These measurements indicate a high sensitivity of IGSCC to the oxygen content of the coolant water.

Ljungberg *et al.* [23] tested 20 different steels including ferritic steels. Their results indicate that ferritic steels are sensitive to TGSCC under pure-water conditions (PWC). However, with hydrogenated water (alternate-water conditions, AWC), no TGSCC was observed (oxygen contents < 10 ppb). They concluded that TGSCC in ferritic and martensitic steels may be inhibited at a somewhat greater oxygen content in the reactor water than that needed for inhibiting IGSCC in sensitized stainless steel. The test results on ferritic and martensitic steels are summarized in Figure 16.2-5.

The fact that the AWC mitigates TGSCC in ferritic and martensitic steels with a somewhat broader margin of acceptable oxygen levels than for IGSCC in sensitized austenitic steels was also observed and reported by DRESDEN-2 experimentalists [25]. It should be noted that TGSCC of the type measured in the above experiments has never occurred in an operating BWR. Presumably, it is specific to the extreme mechanical conditions prevailing in the above-mentioned tests, with a constant extension rate such as the TGSCC observed in austenitic stainless steel with AWC.

Gordon *et al.* [26] also investigated the corrosion resistance of ferritic steels through hydrogen addition to BWR coolants. At a test temperature of 288 °C, the oxygen content was held close to 20 ppb by dissolving 125 ± 25 ppb hydrogen at a pressure of 8.69 MPa. Low-alloy- and carbon-steel samples were characterized by no crack growth under constant load-stress intensities of up to 50.9 MPa-$m^{1/2}$. Under cyclic loads, these samples showed a 7 to 20 times lower crack-propagation rate compared with samples exposed to nominal BWR environment (200 ppb oxygen). Furthermore, the addition of hydrogen to the test water did not show any evidence of hydrogen stress cracking or hydrogen embrittlement in low-alloy and high-strength, wrought martensitic stainless steels.

In addition to the control of the water chemistry, another remedy to SCC has been to develop alternative SCC-resistant materials. The most important materials of this type are the nuclear-grade stainless steels such as AISI 304 NG and 316 NG. These steels have a low carbon content (0.2 wt.%) to avoid sensitization, but contain nitrogen (between

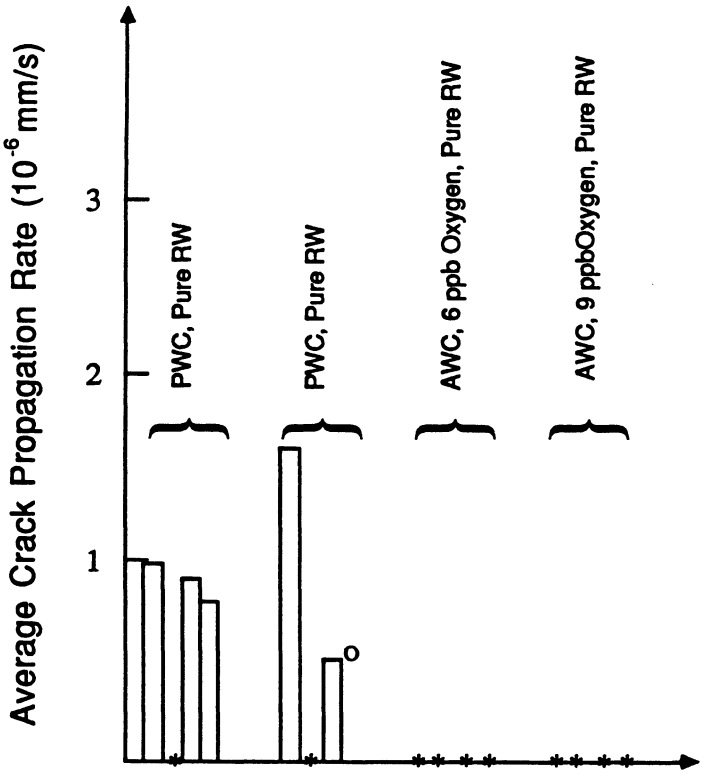

Figure 16.2-5. Summary of RINGHALS-1 CERT test results on ferritic and martensitic steels. For each test condition, the bars and symbols represent the result for the following alloys from left to right: A 204, SA 533, SA 508, and AISI 431. Symbol * denotes no cracking and symbol O denotes the result for the sample accidentally tested at constant load [23].

0.06 and 0.1 wt.%) to maintain the strength required by the ASME Boiler and Pressure Vessel Code. These nuclear-grade materials have been found to be much more IGSCC resistant than the regular AISI 304 and 316 stainless steels [27].

16.2.1.4. Corrosion in nitrates

Nitrates are known to be effective corrosion inhibitors (Table 16.2-IV) for stainless steels. In this section, the effects of nitrates on ferritics and austenitic steels are discussed.

Ferritic steels

In contrast to the voluminous literature on cracking in austenitic stainless steels, little information has been published concerning ferritic stainless steels. Until recently, it was

Table 16.2-VI.

THRESHOLD STRESSES (MPa) OF MILD STEELS IN BOILING NITRATE SOLUTIONS [30]

	Solution Concentration[a]			
Nitrate	8 N	4 N	2 N	1 N
NH_4NO_3	15.5	23.	54.	92.5
Ca $(NO_3)_2$	38.5	54.	92.5	177.5
$LiNO_3$	38.5	62.	146.5[b]	177.5
KNO_3	46.5	69.5	108.	185.5
$NaNO_3$	62.	146.5	170.	201.

(*a*) Normality, N, is in grams of solute per liter.

(*b*) Concentration was 2.5 N for this case.

more or less assumed that ferritic steels would not undergo SCC under similar environments which cause SCC in austenitic steels [28]. However, in the late 1960s, Bond [29] showed that the addition of nickel, copper, or cobalt can cause ferritics to become susceptible to SCC. In molybdenum-free steels, on the other hand, even 1.5-wt.% nickel did not produce susceptibility to SCC. The dependency of SCC on various interstitial components is very complex and strongly depends on the concentration of these components [28].

In an extensive study of SCC in low-strength ferritic steels, Parkins [30] investigated the susceptibility of low-carbon steels to SCC in the presence of a variety of nitrate solutions. Table 16.2-VI demonstrates the varying susceptibility of mild steels to cracking according to the nature of the cation and the concentration of the solution in boiling (atmospheric pressure) nitrate solution. The results show a marked reduction in the threshold stress as the solution concentration is increased. Table 16.2-VI also indicates a variation in the threshold stress with different cations at a constant concentration. According to this data, $NaNO_3$ is the least potent and NH_4NO_3 the most potent solution, with $LiNO_3$ somewhere between these two limits.

The effects of various cations in nitrate solutions have been related to the cation influence on the acidity of the solution. Recent studies have shown that acidic impurities accelerate the crack initiation, while essentially all impurities accelerate the crack growth rate which is governed by the concentration of the anion [31]. Therefore, the potency of the solution can be varied by changes in the pH value. Indeed, constant strain tests in 4 N $NaNO_3$ showed that acidification reduces the time-to-failure, while raising the pH value above 7 (*e.g.,* through addition of NaOH) causes marked increases in the time-to-failure [30 - 33]. This finding, although not substantiated for $LiNO_3$, would indicate an advantage in buffering the pH of the $LiNO_3$ solution to above neutrality to reduce SCC of ferritic steels. On the other hand, for a $Ca(NO_3)_2$ solution, a marked decrease in the time-to-failure below or above a pH value of 4 is observed [30]. Thus, a decrease or an increase in the pH value from a specific range could lead to an order-of-magnitude reduction in the time-to-failure.

An extensive investigation into ion-mitigating SCC of ferritic steel through the addition of various substances was performed by Parkins and Usher [32]. They concluded that oxidizing agents such as $KMnO_4$, $MnSO_4$, $NaNO_2$, and $K_2Cr_2O_7$ generally accelerate crack formation, while compounds such as Na_2CO_3, H_3PO_2, Na_2HPO_4, and $CO(NH_2)_2$ that form insoluble iron products, retard failure. This is an important point, since from a radiolytic point of view, oxidizing agents such as $KMnO_4$ have been shown to reduce the formation of molecular decomposition products such as H_2O_2, OH^-, and H_3O^+. Thus, in a nuclear environment, the two opposing effects of the addition of oxidizer agents to the aqueous coolants have to be optimized. Stress-corrosion cracking is minimized by removing oxidizing agents while radiolytic decomposition is reduced by adding oxidizers.

The effects of halide additions to nitrates have also been studied [34]. Fluoride additions showed no effect, while chlorides and bromides both increased the time-to-failure. Small amounts of chloride added to a 4 N $Ca(NO_3)_2$ solution increased the time-to-failure by orders of magnitude. Addition of chloride to NH_4NO_3 solution had little or no effect on the time-to-failure. The effects of chloride addition to $LiNO_3$ solutions have not been reported. Based on data reported in Table 16.2-VI, no marked effect is expected.

The effects of temperature on the cracking of steels in nitrate solutions follows a typical Arrhenius plot: a logarithmic dependence of failure time on the reciprocal of the temperature, as is seen in Figure 16.2-6 [35]. The slope of the Arrhenius plot is a measure of the activation energy of SCC. Values for the SCC activation energy vary, depending on the cation type and kind of steel used and are very sensitive to the nature of the films that form on the surface of the metals. Therefore, cracking does not depend only on temperature but also on precise electrochemical conditions which may in turn depend

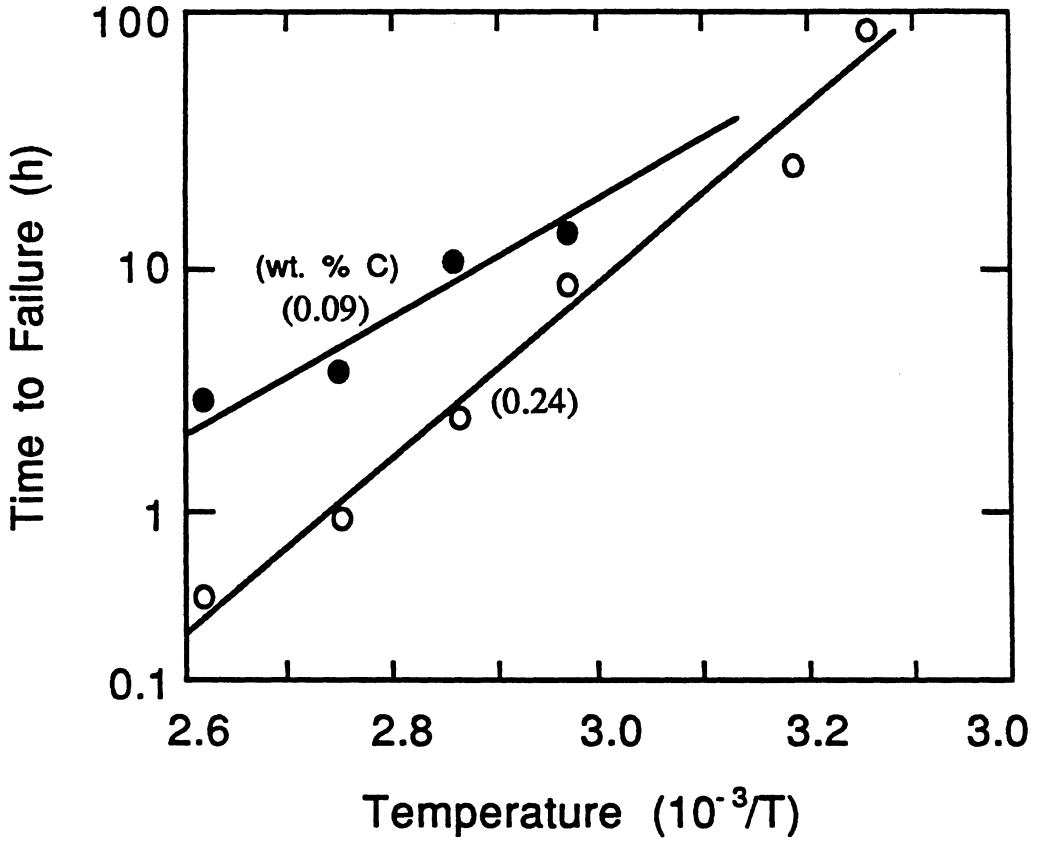

Figure 16.2-6. Effect of the temperature on the time-to-failure of carbon steels in a 60% $Ca(NO_3)_2$ + 3% NH_4NO_3 solution [35].

on the pressure and substances other than the NO_3^- ions. Szklarska *et al.* [33] point out that their measured activation energy for cracking agrees with the dissolution energy of iron in the corresponding nitrate solution. Because of discrepancies, the use of reported activation energies for cracking appears to be limited.

Austenitic steels

The main concern with the use of nitrates is SCC of unalloyed carbon steels. An extensive literature search was carried out by Waeben *et al.* [36] to determine the compatibility of lithium salts with steels as a function of water temperature and salt concentration. They note that no specific corrosion problems are reported for stainless steel in the presence of nitrate solutions, indicating no appreciable difficulties in practice with such systems. Their major findings on the effects of nitrates on corrosion are: (1) The threshold stress to cause failure decreases with an increase in the nitrate concentration.

(2) The failure times change logarithmically with the reciprocal of temperature. (3) The aggressiveness of nitrates with choice of cation decreases in the following order: NH_4, Ca, Li, K, and Na. (4) At a pH value above 7 to 8, the susceptibility of steel to SCC diminishes. (5) The susceptibility to SCC is the highest for steels with about 0.01 to 0.05-wt.% carbon content. (6) Alloying elements such as chromium and molybdenum show a beneficial effect on SCC, but nickel shows little or no effect.

Potentiodynamic polarization curves for 316 SS in water with $LiNO_3$ concentrations of 0.0296 and 0.296 g/cm^3 at 95 and 250 °C have been constructed by Waeben *et al.* [36]. The most significant finding was the lack of a marked transition between the primary and secondary passive regions which indicates that dissolution of a passive layer of alloying elements does not set in abruptly and, thus, a good passive behavior is observed over the entire potential range. Furthermore, the anodic currents are almost independent of the $LiNO_3$ concentration but are strongly temperature dependent. Microscopic examination of the 316 SS showed that a smooth oxide film was formed on the metal surface in $LiNO_3$ solution, with a roughness which was independent of solution concentration and temperature. Some crystallographic attack/deposit and small pits were found on both austenitic and martensitic stainless steels. The duration of the test was too short (200 h) to conclude that stainless steels are susceptible to pitting corrosion in $LiNO_3$ solutions.

16.2.1.5. Discussion

Fundamentals of the nature of corrosion were reviewed briefly to demonstrate that corrosion is primarily an electrochemical process. The electromagnetic environment of a fusion device can, therefore, have unforseen effects on the corrosion rates by the aqueous solution that are not experienced in conventional environments. The complexity of various environmental factors such as temperature, velocity, oxidizers, and other impurities was pointed out. The interdependence of these environmental factors is too great to allow any decisive conclusions regarding approximate corrosion rates. Lack of knowledge of the effects of irradiation and the effects of radiolytic decomposition products on corrosion mechanisms will undoubtedly further complicate the understanding and extrapolation of existing data.

Most recent experience with SCC in the nuclear environment was presented. The most significant finding was that a reduction of oxygen content through the addition of hydrogen to the coolant can reduce SCC in most ferritic and austenitic alloys. The effects of alloying elements on SCC were investigated. The high chromium content of the 9-C alloy (11.84 wt.%) is very helpful in reducing the susceptibility of this alloy to SCC.

The carbon content of the 9-C alloy (0.097 wt.%) is outside the range of highest SCC susceptibility but is high enough for sensitization to occur (> 0.02 wt.%) if the alloy is heated to temperatures above $\sim 950\,^{\circ}$C.

Experience with various aqueous nitrate-salt solutions shows that the choice of the cation will affect the degree of corrosion attack. The aggressiveness of nitrates decreases with choice of the cation in the following order: NH_4, Ca, Li, K, and Na. Thus for the $LiNO_3$ salt, the aggressiveness of NO_3^- ions is in the medium range. The effect of the cation choice on SCC has been related to the acidity of the solution. Investigations into buffering the $LiNO_3$ salt solutions to an optimum pH value could lead to marked reduction in the aggressiveness of the solution. Reduction of the oxidizing strength of the salt solution has been found to retard failure of test samples by SCC. On the other hand, an increase in the oxidizing power of the solution decreases radiolytic decomposition rates. An optimum oxidizing strength has to be established experimentally since the number of factors involved are too large to make analytical predictions.

Recent experiments [36] on the corrosion rates of $LiNO_3$ salt solutions with 316 SS and with a martensitic alloy at 95 and 250 °C show a lack of a marked transition between the primary and secondary passive regions. These data imply that a relatively stable passive layer is formed in this salt. Microscopic examination of the 316 SS showed that a smooth oxide film was formed on the metal surface in $LiNO_3$, with the roughness independent of solution concentration and temperature. Recently, electrochemical corrosion tests were performed for aqueous LiOH and $LiNO_3$ solutions in contact with AISI 316 L stainless steel [37]. It was found that stainless steels, particularly low-carbon steels, exhibit better corrosion resistance in an $LiNO_3$ solution than in LiOH.

It should be noted that most of the above experimental findings regarding corrosion and SCC of steels in $LiNO_3$ salt solutions were obtained without any control of the oxygen content of the solution which plays a significant role. In a fusion environment, the production of tritium will undoubtedly affect the oxygen content of the aqueous solution through recombination. Thus, breeding of tritium in the aqueous solution can potentially reduce corrosion and SCC of the structural material used in the FPC.

The investigation of the corrosion of ferritic steels in an aqueous $LiNO_3$ salt solution does not show unexpectedly high corrosion rates or high susceptibility to SCC. In addition, the latest experimental findings do not indicate any unforeseen catastrophic corrosion attack. However, an extensive research effort needs to be undertaken to confirm these observations. Furthermore, the effects of high-energy-neutron irradiation on corrosion mechanisms and rates should be examined.

16.2.2. Radiolysis of Aqueous Solutions

When water or aqueous solutions are used as the coolant in a fusion reactor, water will undergo extensive radiolysis because of the exposure to high levels of ionizing radiation. Various products such as H_2 and H_2O_2 will be formed, depending on the composition, temperature, pH, and impurities in the coolant. The radiolysis of water causes two major areas of concern. First, radiolysis can create large quantities of explosive gas mixtures. Second, the radiolytic decomposition products, in particular H_2O_2, can enhance the corrosion rate of structural materials.

The TITAN-II FPC is cooled by an aqueous $LiNO_3$ salt solution. The presence of lithium atoms undergoing (n,α) reactions in the coolant introduces high-energy α and tritium recoil ions. These energetic ions, together with neutrons, interact with the surrounding water molecules causing the decomposition of water molecules. Thus, contributions from both the ionizing radiation and the nuclear reactions in the aqueous solution should be included in the analysis.

It is desirable to quantify the radiolytic products as a function of water chemistry, impurity levels, temperature, and the characteristics of the radiation field. However, the complex interrelationship between environmental factors and the formation rates of the decomposition product makes this task very difficult. Furthermore, very little experimental data are available on production and recombination rates of radicals in aqueous $LiNO_3$ salt solutions.

In this section, an introduction to radiation chemistry is given (Section 16.2.2.1), followed by a qualitative description of radiolytic processes. Effects of $LiNO_3$ additions on radiolysis are reviewed. In conclusion, the findings and uncertainties due to the radiolysis of the salt solution are summarized.

16.2.2.1. Background

Ever since Roentgen discovered the X ray, the effects of nuclear radiation which cause chemical changes have been investigated as a branch of chemistry (radiation chemistry). During the 1960s, radiation chemistry received a great deal of attention and identified intermediate species in gases and liquids, the mechanism of energy loss of free-radical and ion-pair formation and distribution, and transient species. International conferences are still being held, mostly in Europe, with heavy contribution from eastern block scientists. While the literature of the 1960s is rich in research performed on various nitrate solutions,

$LiNO_3$ solutions have only been studied in the last decade and mostly by scientists in the USSR.

Interaction of highly energetic particles and photons with matter can be divided into two categories: light particles (electrons and photons), and heavy particles. It is important to note that the chemical effects produced in the water by this variety of radiation is much the same. The main difference lies in the geometrical distribution of the intermediate products that are formed by the interaction of the radiation with matter.

Photons

Photons produce free electrons by interacting with matter through three processes:

Photoelectric effect. All of the photon energy is given to one electron. The most tightly bound electron in water, the K-electrons of oxygen, requires 532 eV to become ionized and removed from the molecule. The excess energy of the photon will, therefore, appear as kinetic energy of one electron.

Compton effect. The photon only gives up part of its energy to an electron. The remainder is carried by a scattered photon of longer wavelength which eventually will be absorbed by the photoelectric effect.

Pair formation. For photons with energies above 1 MeV, the pair-formation process becomes significant. When a high-energy photon passes near an atomic nucleus, a pair of positive (positron) and negative electrons may be formed. The probability of pair formation is directly related to the charge of the nucleus. For water, the pair-formation process is negligible.

Electrons

The rate at which a moving electron loses energy, $-dE/dx$, is called "stopping power" by physicists and "linear energy transfer" (LET) by radiobiologists. For nonrelativistic electrons having energies below 50 keV the energy loss equation is [38]:

$$-\frac{dE}{dx} = \frac{2\pi e^4 NZ}{E} \ln\left(\frac{E}{I}\sqrt{\frac{\epsilon}{2}}\right), \qquad (16.2\text{-}3)$$

where e is the charge of the electron, E is the energy of the moving electron, NZ is the number of electrons per unit volume of irradiated material, $\epsilon = 2.71828$ is the base of natural logarithms, and I is a number characteristic of each material (sometimes called "stopping potential"). Parameter I depends on the atoms present in the material but is independent of the chemical bound of the atoms. For water, the value of I has been estimated between 66 [39] to 69 [40]. For $I = 66$, Equation 16.2-3 can be reduced to

$$-\frac{dE}{dx} = \frac{1019}{E} \log\left(\frac{E}{56.6}\right), \tag{16.2-4}$$

where $-dE/dx$ is in units of eV/Å. At higher energies, Equation 16.2-4 is modified to include the relativistic change of mass of the electron, resulting in a minimum value of $-dE/dx$ of 0.018 eV/Å for electron energies in the range of 1 to 2 MeV.

Another quantity of interest is the energy loss of the electron in each event. Although the probability of energy loss decreases exponentially with increasing electron energy, at low energies, the probability depends on the binding energy of the electron in the material and becomes difficult to calculate. Pollard [41] has determined the average energy loss per event to be 110 eV ± 30% in a low-pressure cloud chamber. The true value may be different in liquid water than in the gas cloud chamber.

If the electron energy greatly exceeds the ionization potential, another fast electron will be produced which is called a secondary or tertiary electron. These secondary electrons may carry enough energy to cause ionization along their path lying within a few Å of the primary ionization event and leading to the formation of a cluster of ions. These groups, referred to as "spurs," will form along the main track of the primary electron.

Figure 16.2-7 shows the LET for electrons in water as a function of electron incident energy. While passing through matter, electrons change direction frequently as a result of collisions with atomic nuclei. The loss of energy with distance refers to the actual distance traveled, not to the distance between beginning and end of path.

Heavy charged particles

Ions travel at slower speeds than an electron of equal energy because ions are much heavier. The LET equation for ions is similar to that for electrons, except that it also depends on the magnitude of ion charge:

$$-\frac{dE}{dx} = \frac{2\pi e^4 Z_i^2 NZ}{E} \frac{M}{m} \ln\left(\frac{4E}{I}\frac{m}{M}\right), \tag{16.2-5}$$

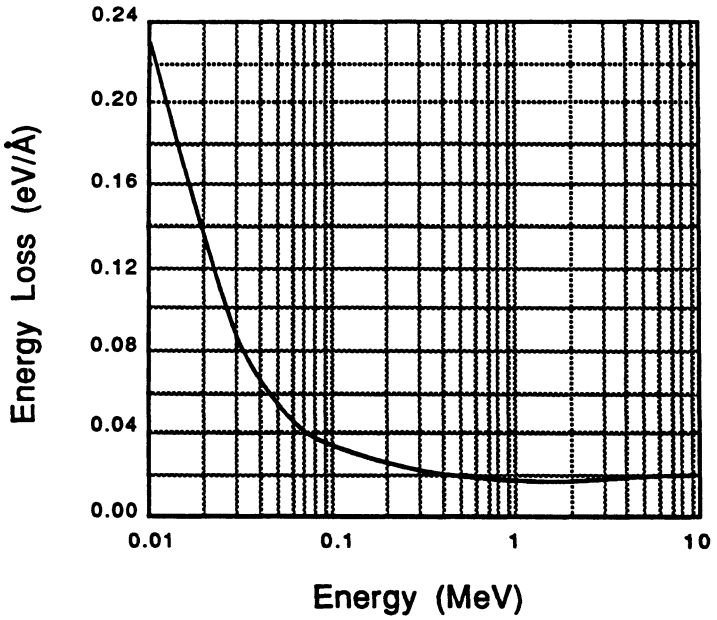

Figure 16.2-7. The LET for electrons in water [42].

where M and Z_i are, respectively, the mass and atomic number of the moving ion. Assuming $I = 66$ for water, the LET equation for protons reduces to:

$$-\frac{dE}{dx} = \frac{1.876}{E} \log\left(\frac{E}{0.0605}\right), \tag{16.2-6}$$

and for α particles to

$$-\frac{dE}{dx} = \frac{29.735}{E} \log\left(\frac{E}{0.1203}\right), \tag{16.2-7}$$

where E is units of MeV and $-dE/dx$ in units of eV/Å. The LET for helium ions (α particles) in water is shown in Figure 16.2-8.

Towards the end of the track, where the charged particle energy is reduced, it may capture electrons from the surroundings and become a fast-moving neutral atom (*e.g.*, for α particles with energies below $\sim 0.5\,\text{MeV}$). As the neutral atom travels through the media, it may lose one, or all, of its electrons and recapture them a later time. The net energy loss of a neutral during these electron loss and capture processes is, therefore, much lower than that of a charged particle. The energy of the fast-moving neutrals is transferred primarily by direct collisions or "knock-ons" to the target nuclei.

Since the LET is proportional to the fourth power of the charge of the particle, α particles have small LET values. Therefore, an α particle retains its charge over a large part of the track, maintaining a fairly constant stopping power until it reaches the knock-on mode.

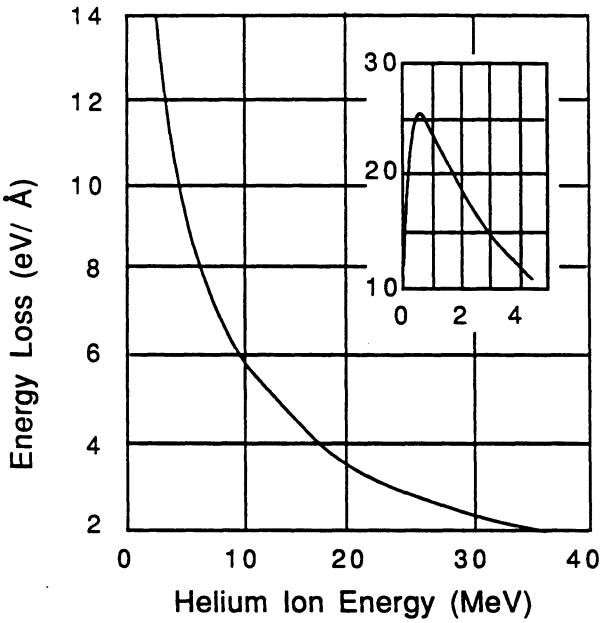

Figure 16.2-8. The LET for helium ions (α particles) in water [42].

Neutrons

Fast neutrons lose their energy by collision with the atoms in the material. In water, the hydrogen atom will take up most of the energy (on average, about half the energy of the neutron). The recoil hydrogen atom starts to travel at a very high velocity, is immediately stripped of its electrons, and becomes a fast proton. Therefore, irradiation by fast neutrons actually results in irradiation by fast protons.

16.2.2.2. Products of the radiolysis

The water decomposition products are often termed "molecular decomposition products" to distinguish them from the short-lived free radicals. The overall process can be broken up into three stages. During the first stage (lasting $\leq 10^{-13}$ s), mainly H_2O^+ ions and excited water molecules, H_2O^*, are produced. These products undergo a series of transformations during the second stage (lasting $\sim 10^{-11}$ s). These second stage transformations result in the formation of hydrogen atoms, hydrated electrons, OH radicals, and some H_2 and H_2O_2. Only during the third stage do the radicals undergo a variety of chemical reactions. If the radical concentration is high (*e.g.*, in or close to spurs),

radicals recombine to form molecular products H_2 and H_2O_2. This stage is completed within 10^{-9} to 10^{-8} s after irradiation. Radicals which do not recombine in the spurs will recombine in the bulk of the solution or, if present, with solutes. These reactions will be completed within 10^{-7} to 10^{-2} s [43].

In describing the system of reactions occurring during water decomposition, the hydrated electron is used. The solvated electron, called "hydrated" electron (e^-_{aq}), is trapped in a solvation shell. The discovery of hydrated electrons showed that electrons in water were chemical entities, as distinct from possessing purely physical characteristics. They have diffusion properties, size and sphere of influence, associated ion atmosphere, and reaction rate parameters, all comparable to normal chemical reagents [44]. The hydrated electron, e^-_{aq}, reacts with a hydrogen ion and produces a hydrogen atom:

$$e^-_{aq} + H^+ \rightarrow H\,. \tag{16.2-8}$$

Today it is widely accepted that the hydrated electron is the precursor for the formation of the hydrogen atom.

Interactions between the hydrated electron and water, and between the radicals constitute the following molecular product equations:

$$e^-_{aq} + e^-_{aq} + 2H_2O \rightarrow H_2 + 2OH^-\,, \tag{16.2-9}$$

$$e^-_{aq} + OH \rightarrow OH^-\,, \tag{16.2-10}$$

$$H + H \rightarrow H_2\,, \tag{16.2-11}$$

$$OH + OH \rightarrow H_2O_2\,, \tag{16.2-12}$$

$$H + OH \rightarrow H_2O\,. \tag{16.2-13}$$

The radicals that escape reactions with other radicals have a chance to diffuse away from the spurs and react with other molecular products. These reactions are denoted as "chain reactions" since they result in radicals that could again react with other molecules:

$$H_2O_2 + H \rightarrow H_2O + OH\,, \tag{16.2-14}$$

$$H_2 + OH \rightarrow H_2O + H\,. \tag{16.2-15}$$

Although some hydrogen and hydrogen peroxide is produced by direct association of water through

$$H_2O + H_2O^* \rightarrow H_2 + H_2O_2\,, \tag{16.2-16}$$

it has been established that most of the H_2 and H_2O_2 is formed by the radical recombination reactions (Equations 16.2-11 and 16.2-12). The molecule H_2O^* denotes an excited water molecule.

Oxygen is found among the water decomposition products, although it seems to be formed not directly from water but as a result of action of the radicals on hydrogen peroxide. Thus, the radiation decomposition of water is generally described in terms of the amounts of molecular H_2 and H_2O_2, the free radicals H and OH, and the free-radical decomposition products such as O_2 and HO_2. The HO_2 molecule forms mostly with heavy-particle irradiation and has to be included as another quantity to be considered. When solutes are present, subsequent reactions of these entities with the dissolved material are also included.

It is important to note that although the free radicals are generally denoted as H and OH, their actual molecular constitution is not absolutely known. It is clear that H is a powerful oxidizing agent while OH is a powerful reducing agent, and that they can react with each other to form H_2 and H_2O_2. In a polar medium (*i.e.*, water), solutes are often found to exist in acidic or basic forms. The radical OH might be present in its basic form (O^-) or in its acidic form (H_2O^+), and the H radical may actually exist as a solvated electron (basic form of H) or acidic form H_2^+ (loss of a proton is termed "basic," gain of a proton is termed "acidic"). So the ionization process of a water molecule results in a free electron and an H_2O^+ ion. This ion is the "basic" form of the H radical or the "acidic" form of the OH radical.

16.2.2.3. Molecular and radical yields in water

Reaction yield for a product, P, is denoted by $G(P)$ and refers to the number of radicals or molecules which are produced by radiation and determined by chemical analysis. Reaction yields expressed in this manner are different from the number of molecules and radicals which are produced directly by the radiation because these products may decompose further by reacting with the free radicals. Reaction yields are expressed in terms of numbers of molecules or radicals produced per 100 eV of energy absorbed by the media.

Gamma rays

Highly pure water irradiated with X or γ rays appears to be stable, showing no decomposition at all. The apparent stability arises from the reaction of free radicals with

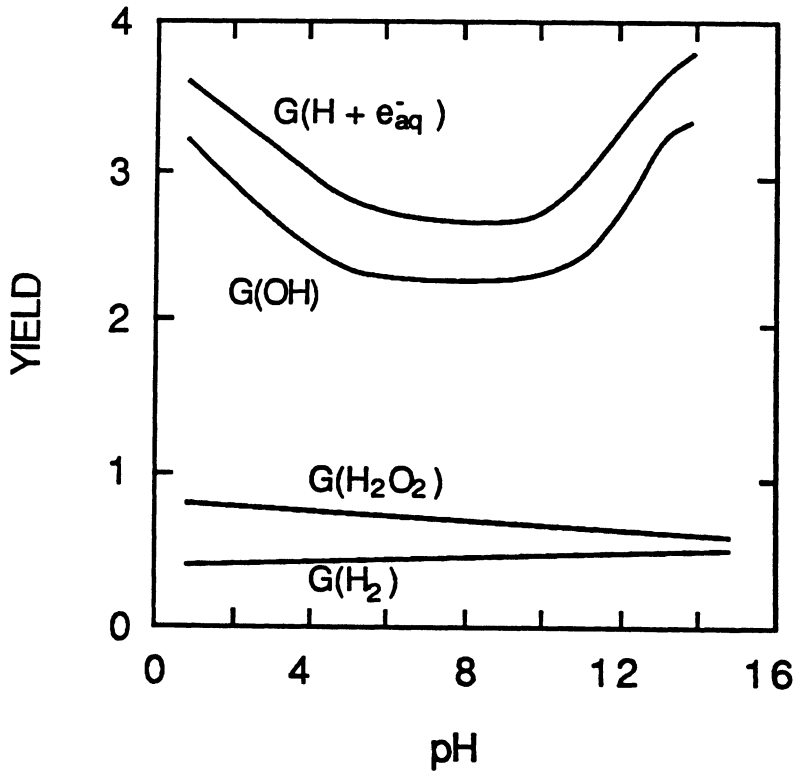

Figure 16.2-9. Variation of the primary yields of γ-irradiated water with the pH value.

molecular products (H_2 and H_2O_2) leading to recombination back to water. The net stability of water is seen to depend on whether the hydrogen gas is retained in the water to be acted on by the radicals, or allowed to escape. This was shown through experiments in which the hydrogen gas could escape to evacuated volumes [45].

The effect of pH on γ-ray yields of ordinary water has been well documented [42,43]. Figure 16.2-9 shows that the primary yields for gamma irradiation varies little in the pH range of 4.5 to 10.5 [46].

Alpha particles

When pure water is irradiated with α particles (high LET), the number of molecular decomposition products formed is too great to be converted back into water, resulting in a continuing net decomposition of water. Heavy-particle radiation, therefore, leads to extensive decomposition of the water into hydrogen gas, hydrogen peroxide, and oxygen, while the effect on dissolved solutes is considerably less for a given energy than with the light-particle radiation [47].

As early as 1913, a careful study of the decomposition of water in three phases (ice, liquid, and steam) by α particles from radon was published by Duane and Scheuer [48]. They reported considerable formation of hydrogen peroxide, oxygen, and hydrogen. More recently, Lefort [49] showed that the hydrogen yield from the action of α particles on a larger number of solutions to be about the same, with value of $G(H_2) \simeq 1.7$. Since the OH radicals are the prime radicals that convert the molecular hydrogen back to water, the α-particle yield of free OH must be very small. One explanation is that the free radicals must be produced so densely in the track of the α particle that nearly all undergo initial recombination to form H_2 and H_2O_2, or to go back to water [50].

Since the track density (of radicals) is directly related to the LET, the ratio of radicals to molecular yield should increase with decreasing LET. Another possible reaction in dense tracks is the encounter of an H_2O_2 with a third OH radical:

$$OH + H_2O_2 \rightarrow H_2O + HO_2 \,. \tag{16.2-17}$$

Consequently, for particles of high LET, there are five primary yields: G_H, G_{OH}, G_{H_2}, $G_{H_2O_2}$, and G_HO_2. Quick estimates for high-LET radiation can be found from curves that display yields as a function of initial LET. Figure 16.2-10 shows typical yield curves for neutral solutions [50].

Jenks [51] has estimated the LET and the associated yields for γ rays, fast neutrons, and α particles from $^{10}B(n,\alpha)^7Li$ reactions. These values are summarized in Table 16.2-VII together with estimates for α-particle yield from $^6Li(n,\alpha)T$ reaction, derived from Figure 16.2-10.

16.2.2.4. Molecular and radical yields in concentrated solutions

Gamma rays

Over the past decade, considerable information has been accumulated on γ-ray yields in concentrated solutions, particularly for solutions containing nitrates such as $NaNO_3$, $LiNO_3$, $Ca(NO_3)_2$, and KNO_3. Until recently, no satisfactory (*i.e.*, quantitatively and qualitatively self-consistent) account could be given of the radiolytic behavior of these systems [50]. In order to explain radiolysis mechanisms of concentrated solutions, Kiwi and Daniels [52] progressively measured the yields of various nitrated solutions as a function of solute concentrations under γ irradiation. The radiolysis of nitrate solutions is characterized by a yield of nitrite ions (NO_2^-), increasing continuously with nitrate concentration up to the solubility limit and the occurrence of O_2 as a major product.

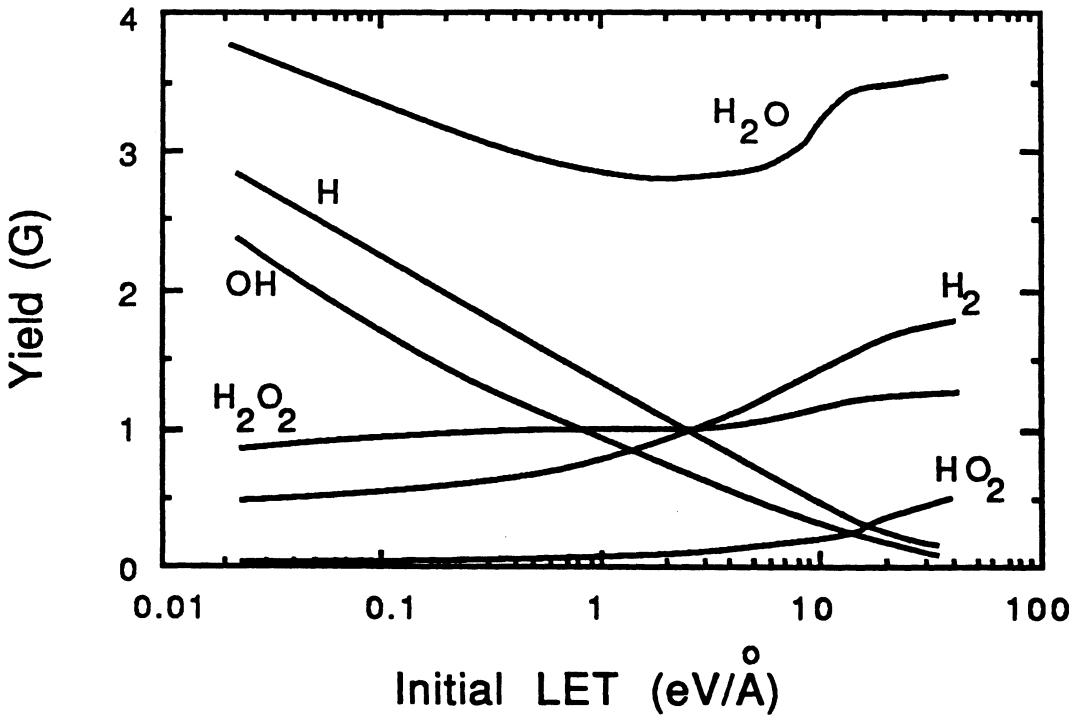

Figure 16.2-10. Water-decomposition yields in neutral solution as a function of initial LET of α particles [50].

Table 16.2-VII.

YIELDS AND LET FOR GAMMA RAYS, FAST NEUTRONS, AND ALPHA PARTICLES IN WATER [51]

Energy Source	Initial LET (eV/Å)	Yields (No./100 eV)				
		H_2	$H + e^-_{aq}$	H_2O_2	OH	HO_2
γ ray	0.02	0.44	2.86	0.70	2.34	0.00
Neutrons	4.0	1.12	0.72	1.00	0.47	0.17
$^{10}B(n,\alpha)^7Li$	24.	1.70	0.20	1.30	0.10	0.30
$^6Li(n,\alpha)T$ (a)	4.	1.2	0.7	1.0	0.4	0.2

(a) Estimated based on the data of Figure 16.2-10.

Nitrites are formed via the reaction of nitrate ions with reducing radicals [43]:

$$NO_3^- + H \rightarrow NO_2 + OH^- , \quad (16.2\text{-}18)$$

$$NO_3^- + OH \rightarrow NO_3 + OH^- , \quad (16.2\text{-}19)$$

$$NO_3^- + e_{aq}^- \rightarrow NO_3^{2-} , \quad (16.2\text{-}20)$$

$$2NO_2 + H_2O \rightarrow NO_2^- + NO_3^- + 2H^+ , \quad (16.2\text{-}21)$$

$$2NO_3^{2-} + H_2O \rightarrow NO_2^- + NO_3^- + 2OH^- . \quad (16.2\text{-}22)$$

While the above reactions are termed "indirect" reactions, "direct" reactions can also occur:

$$2NO_3^- \rightarrow 2NO_2^- + O_2 , \quad (16.2\text{-}23)$$

$$NO_3^- \rightarrow NO_2^- + \frac{1}{2}O_2 . \quad (16.2\text{-}24)$$

Kiwi and Daniels [52] have measured the yields for H_2, H_2O_2, O_2, and NO_2. The experimental data are difficult to explain because nitrite is formed indirectly (Equations 16.2-18 to 16.2-22) and directly (Equations 16.2-23 to 16.2-24). Kiwi and Daniels were able to explain and distinguish between the direct and indirect yields using an electron fraction model [50]. They concluded that for all of the nitrate solutions such as $NaNO_3$, $LiNO_3$, $Ca(NO_3)_2$, and KNO_3, and with more than 1 molar concentration, the major products are nitrite, peroxide, and oxygen. Table 16.2-VIII lists the various yields as a function of salt concentration in $LiNO_3$ solutions. Figures 16.2-11 and 16.2-12 present these results and show that, as the molarity of the solution increases, $G(H_2O_2)$ and $G(H_2)$ decrease drastically, while $G(NO_2^-)$ and $G(O_2)$ values stay fairly flat, increasing only slightly with increasing salt concentration.

The experimental yields were explained by assuming that the phenomena characteristic of concentrated solutions originates independently of water radiolysis [50]. Hence, the yield for a product (P), formed both in dilute and concentrated solutions, can be written as:

$$G(P) = G(P)_{H_2O} \times f_{H_2O} + G(P)_{NO_3^-} \times f_{NO_3^-} , \quad (16.2\text{-}25)$$

where $G(P)$ is the measured yield and $G(P)_{H_2O}$ and $G(P)_{NO_3^-}$ are constant yield characteristics of dilute and concentrated solutions, respectively. The values of the weighting coefficients are estimated to be 0.331 and 0.342 for $f_{NO_3^-}$ and 0.646 and 0.635 for f_{H_2O} for $LiNO_3$ solution with 7 and 7.2 mol/liter concentration, respectively [50]. No yields for

Table 16.2-VIII.

YIELDS FOR GAMMA RADIATION IN $LiNO_3$ SOLUTIONS [a] [52]

Molarity[b]	H_2O_2	H_2	NO_2^-	O_2
1	0.63	0.15	1.4	0.35
2	0.53	0.09	1.5	0.75
3	0.45	0.05	$\sim$ 1.55	$\sim$ 0.8
5	0.35	0.03	$\sim$ 1.6	$\sim$ 0.85
7	0.33	$<$ 0.01	$\sim$ 1.7	$\sim$ 0.6
9	0.26	$<$ 0.01	$\sim$ 1.8	–

(*a*) In units of No./100 eV.

(*b*) Molarity, M, is defined in units of mol/liter of $LiNO_3$.

OH as a function of molarity were reported, since it was shown that $G(OH)$ will be fairly independent of the concentration of the nitrate solutions [50]. Thus, for all practical purposes, the corresponding value for water can be used.

Scavenging

For concentrated solutions, it is found that oxidizing agents will gradually decrease the H_2 yield as the concentration of the oxidant is increased, and reducing agents will decrease the H_2O_2 yield [53]. This effect is expected, because solute molecules that are present in the spur may react with the radicals before they have a chance to encounter a radical of the same kind. Thus, the probability of molecular product formation decreases as the solute concentration increases. The process of picking up and destroying radicals by solutes is referred to as "scavenging." Some experience has been gathered in the fission industry by using copper as a scavenger to reduce the molecular-product yield [54].

The scavenger effects on the molecular-product yields for γ rays has been studied closely since the mid-1950s [53,55,56]. Sworski [55] measured the hydroxide peroxide

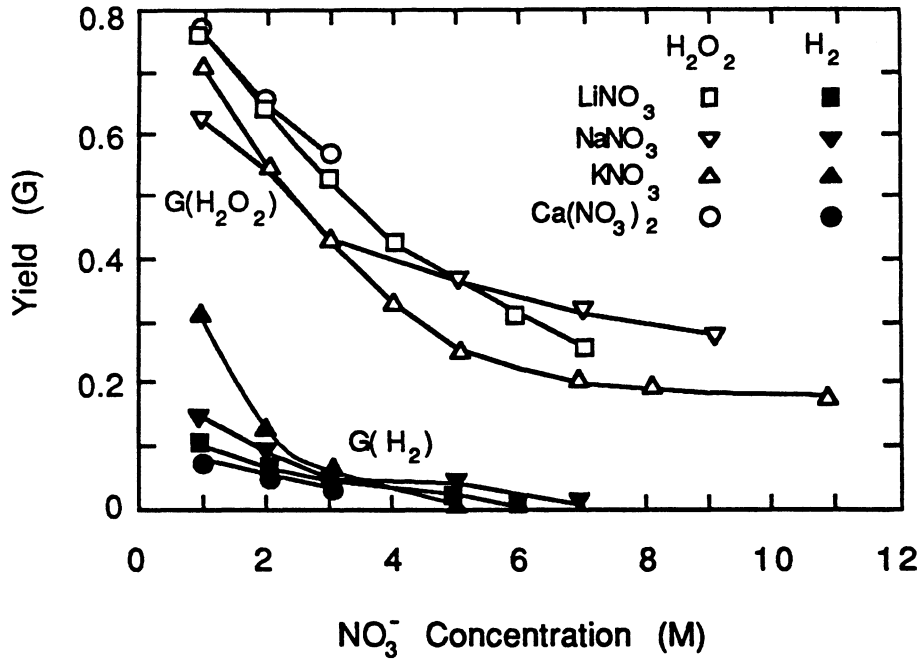

Figure 16.2-11. Yields of hydrogen, $G(H_2)$, and hydrogen peroxide, $G(H_2O_2)$, as functions of molarity (mol/liter) of the nitrate salt solution.

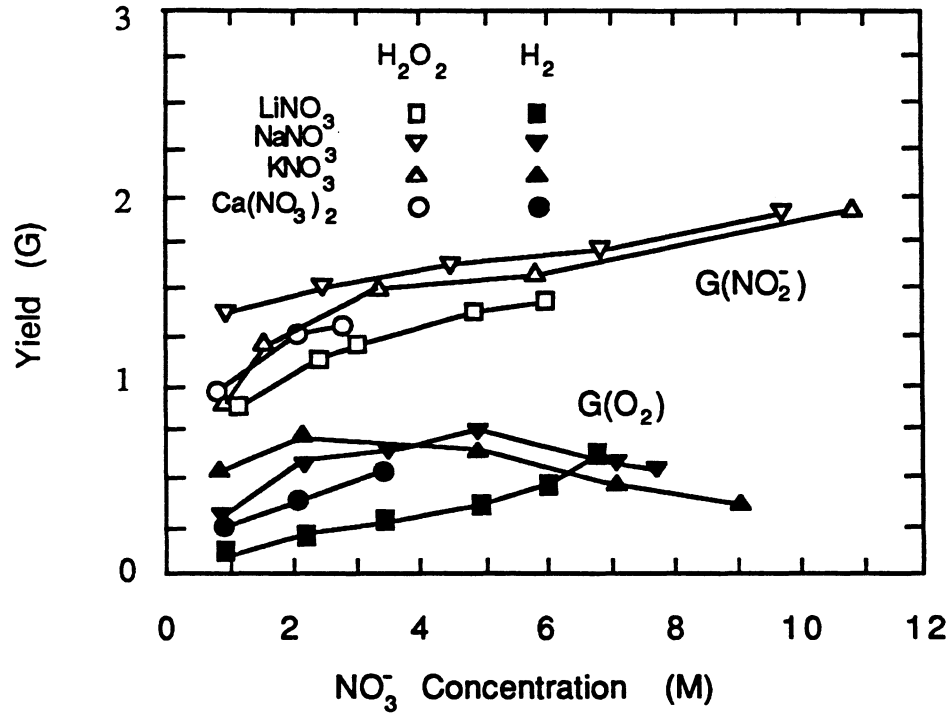

Figure 16.2-12. Yields of oxygen, $G(O_2)$, and nitrate ion, $G(NO_2^-)$, as functions of molarity (mol/liter) of the nitrate salt solution.

yield, $G_{H_2O_2}$, in aerated acid solutions as a function of bromide concentration (X). As the bromide concentration increased, $G_{H_2O_2}$ decreased linearly in the cube root of the bromide solution, or:

$$G_{H_2O_2}(X) \simeq G^{\circ}_{H_2O_2} + G_c \times (X)^n , \tag{16.2-26}$$

where $n = 1/3$ for γ-ray irradiation, G° is the molecular yield (molecules/100 eV of radiation absorbed in very dilute solutions), G_c is a constant, and X is the concentration (molarity) of the solution. Schwarz [53] discovered that the hydrogen yield and the peroxide yield could be greatly reduced by concentrations of potassium nitrite and copper sulfate.

Nitrate ions at high concentrations were found to reduce the H_2 yield under nuclear reactor radiation to values less then 0.05 [57]. This result verifies that molecular hydrogen does not form directly by splitting of the hydrogen from the water molecule by

$$H_2O + e^-_{aq} \rightarrow H_2 + O^- , \tag{16.2-27}$$

but by the combination of H atoms. Ferric ions are among other scavengers that reduce G_{H_2} in acid solutions [53]. In general, substances that react readily with H atoms reduce G_{H_2}, while those reacting with OH reduce $G_{H_2O_2}$.

Alpha particles

While the γ-ray yields are well known as a function of $LiNO_3$ salt concentration, the α and tritium recoil yields have not been studied to this extent. The effect of scavenger concentrations was investigated by Burton and Kurien [58]. They concluded that: for γ rays, the exponent n of Equation 16.2-26 is about 1/3; for 50-keV X rays, $n \sim 0.26$; and for 3.4-MeV α particles, $n \sim 0.15$. These results indicate that higher LET radiation yields are more sensitive to solute concentrations than are low LET radiation yields. H_2 and H_2O_2 yields can be approximated as a function of nitrate concentration by:

$$G^{(3.4\,MeV\ \alpha)}_{H_2,H_2O_2}(X) \simeq G^{\circ}_{H_2,H_2O_2} + G_{c1} \times X^{0.15} . \tag{16.2-28}$$

Unfortunately the power law has not been investigated for yields of H, OH, and HO_2. The effect of scavenger concentration on these yields can be estimated using a mass balance equation resulting in:

$$G^{(3.4\,MeV\ \alpha)}_{H,OH}(X) \simeq G_{H,OH} \times (2X)^{-0.15} , \tag{16.2-29}$$

$$G^{(3.4\,MeV\ \alpha)}_{HO_2}(X) \simeq G_{HO_2} \times (3X)^{-0.15} . \tag{16.2-30}$$

Using Equations 16.2-28 through 16.2-30 and the water decomposition yields from Figure 16.2-10, the various yields as a function of salt concentration for the high LET radiation from ^{6}Li(n,α)T reactions can be estimated. Table 16.2-IX shows these estimated values.

16.2.2.5. Temperature effects

In general, the stability of non-boiling water to radiolysis increases as the temperature is increased, caused by the increase in the reaction rates between various radicals. Burns [59] has estimated the temperature dependance of reaction rate constants, k,

$$k(T) = k(T_o) \exp\left[-Q\left(\frac{1}{T_o} - \frac{1}{T}\right)\right], \qquad (16.2\text{-}31)$$

where T is temperature in K, T_o is the room temperature, and Q is the activation energy. Equation 16.2-31 can be used to estimate reaction-rate constants at higher temperatures.

Most of the experimental data of nitrate solutions reported in this section do not include the effect of temperature on various yields. However, Cohen points out that

Table 16.2-IX.

YIELDS FOR ^{6}Li(n,α)T REACTIONS IN $LiNO_3$ SOLUTION[a]

Molarity[b]	H_2	H_2O_2	H	OH	HO_2
0	1.2	1.	0.7	0.4	0.2
2	1.08	0.9	0.57	0.32	0.15
3	1.00	0.85	0.53	0.31	0.14
5	0.95	0.79	0.50	0.28	0.13
7	0.90	0.75	0.47	0.27	0.13
9	0.86	0.72	0.45	0.26	0.12

(*a*) Yields (No./100 eV) are based on the power-law measurement by Burton [58].

(*b*) Molarity, M, is defined in units of mol/liter of $LiNO_3$.

experiments in the High-Flux Irradiation Facility (HFIR) show a decrease of about an order of magnitude in yields for H_2 and H_2O_2, and about a factor of two decrease for HO_2 and O_2 yields as the temperature rises from room temperature to 200 °C [46]. In high-temperature coolants of power reactors, oxygen cannot be detected until hydrogen concentrations fall below the normally maintained levels of 25 cm^3/kg.

16.2.2.6. Tritium issues

The breeding of tritium in the coolant of a fusion reactor will lead to high-LET radiation which forms HO_2 molecules. These molecules are precursors of free-oxygen formation. Experiments with power reactors have shown that if oxygen is added to the coolant at high-power levels, rapid recombination with the existing hydrogen will occur [46]. Out-of-pile experiments with stainless-steel tubes at 260 °C have shown that excess oxygen will disappear with characteristic half-life of about 1.5 h, independent of hydrogen concentration [60], most probably reacting on the metal surface. Therefore, although the aqueous solution containing $LiNO_3$ salt will produce more oxygen than the salt-free coolants of fission power reactors, the production of tritium should enhance oxygen-hydrogen recombination under non-boiling conditions.

The nuclear reaction ^{6}Li(n,α)T causes tritium atoms to recoil with 2.73 MeV of energy. Tritium atoms have been shown to react chemically while still possessing some of the kinetic energy. The high-energy tritium, "hot hydrogen," is believed to undergo a hydrogen abstraction reaction:

$$T + HOH \rightarrow HT + OH\,, \tag{16.2-32}$$

or an isotopic exchange reaction:

$$T + HOH \rightarrow TOH + H\,. \tag{16.2-33}$$

The activation energies for reactions 16.2-32 and 16.2-33 are, respectively, energies of 24 kcal/mol and 18 kcal/mol.

Thermal hydrogen atoms (low-energy tritium) will undergo reactions with the H and OH radicals to form HT or TOH by:

$$T + H \rightarrow HT\,, \tag{16.2-34}$$

$$T + OH \rightarrow TOH\,. \tag{16.2-35}$$

Table 16.2-X.

HT/HTO RATIOS OF NEUTRON-IRRADIATED SOLUTIONS [61]

Solution	HT/HTO Ratio
1.5 M $LiNO_3$, 0.1 M NaOH	0.06
1.5 M $LiNO_3$, 0.1 M NaOH	0.08
0.6 M LiOH	0.04
0.7 M LiCl, pH 14	0.048
1.0 M LiCl, 1 M NaOH	0.07

Kambara *et al.* [61] have made a detailed study of the HT/HTO ratio formed during neutron irradiation of various lithium-containing solutions. They studied aqueous solutions of $LiNO_3$, LiOH, and LiCl at pH values ranging from 1 to 11 irradiated to a total flux of 10^{14} to 10^{15} neutrons/cm^2. They found all HT/HTO ratios fall in the range of 0.04 to 0.12 with an average ratio of 0.10 ± 0.01. Table 16.2-X shows the HT/HTO ratios of some of the solutions studied.

An LiCl solution saturated with $KMnO_4$ showed an HT yield of zero. The NO_3^- ion is known to be an excellent scavenger for thermal hydrogen atoms through the following reaction:

$$H + NO_3^- \rightarrow NO_2 + OH^- . \tag{16.2-36}$$

In fact, nitrate scavenging of thermal hydrogen atoms competes very successfully with hydrogen-atom recombination. Sowden [57] has shown that a 15.9-M $CaNO_3$ solution irradiated by fast neutron and γ rays shows a 75-fold reduction in hydrogen yield, $G(H_2)$, compared to that observed in water. However, it can be seen from Table 16.2-X that LiCl and LiOH also introduce strong H scavengers into solution. Thus the choice of lithium salt will have little effect on the HT/HTO ratio.

16.2.2.7. Discussion

Radiolysis of pure water and of aqueous $LiNO_3$ salt solutions by light and heavy particles was investigated. Gamma-ray radiolysis yields of $LiNO_3$ salt solutions are known as a function of salt concentration. At high concentrations, the H_2 yields are very small and the H_2O_2 yield decreases by a factor of about 3 relative to pure water. Oxygen yields of light-particle radiation are fairly independent of the salt concentration.

Energetic α particles (3.4 MeV) are produced by nuclear reactions with lithium in the aqueous $LiNO_3$ salt solution. Reaction yields were estimated as a function of salt concentration based on the power-law measurements of 3.4-MeV α particles. The oxygen production by heavy-particle radiation increases while the yields of H_2, H_2O_2, H, OH, and HO_2 all decrease with increasing salt concentration. The increase in oxygen production due to radiolysis may be balanced by the production of tritium atoms. It has been shown that oxygen added to non-boiling fission-reactor coolants at high-power levels rapidly combines with any hydrogen present. The decrease in the yield of free radicals in concentrated $LiNO_3$ solutions makes this salt more favored than LiOH solutions.

The effect of elevated temperature on radiolysis was investigated. From experience gained in the fission industry with pure water, it can be ascertained that the stability of non-boiling water to radiolysis increases as temperature increases. The apparent stability is actually caused by an increase in radical recombination rates at elevated temperatures.

In conclusion, although many uncertainties remain and much research is required in the area of radiolysis, the use of a highly concentrated, aqueous $LiNO_3$ salt solution should not lead to the formation of volatile or explosive gas mixtures. The effects of radiolytic decomposition products on corrosion, however, remain uncertain and experimental data on the behavior of radiolytic decomposition products in a fusion environment are needed.

16.2.3. Properties of $LiNO_3$ Solutions

The physical properties of concentrated solutions of $LiNO_3$ at high temperatures differ from those of pure water. Therefore, a fairly detailed investigation of the physical properties of the aqueous solutions was made, including an extensive literature survey, to ensure that reliable data were used in analyzing the performance of the TITAN-II FPC. The physical properties of $LiNO_3$ solutions as functions of temperature and salt concentration are given in the following subsections. During the TITAN-II design period, it proved convenient for the neutronics analysis to specify the salt concentration as the

atomic percentage of Li atoms present. As other measures of concentration are also commonly used, the relationships between the molality of the solution, m (the number of moles of solute per 1 kg of solvent), and the weight percentage of the solute, W, as a function of the atomic percentage of Li, A_{Li}, are given in the following equations:

$$m = \frac{3000 A_{Li}}{M_w(100 - 5A_{Li})}, \tag{16.2-37}$$

$$W = \frac{300 A_{Li} M_s}{3A_{Li}M_s + M_w(100 - 5A_{Li})}, \tag{16.2-38}$$

where M_w and M_s are the molecular masses of the water (18.02) and of the solute (68.94 for natural $LiNO_3$), respectively. Figure 16.2-13 shows these relationships over the concentration range of interest.

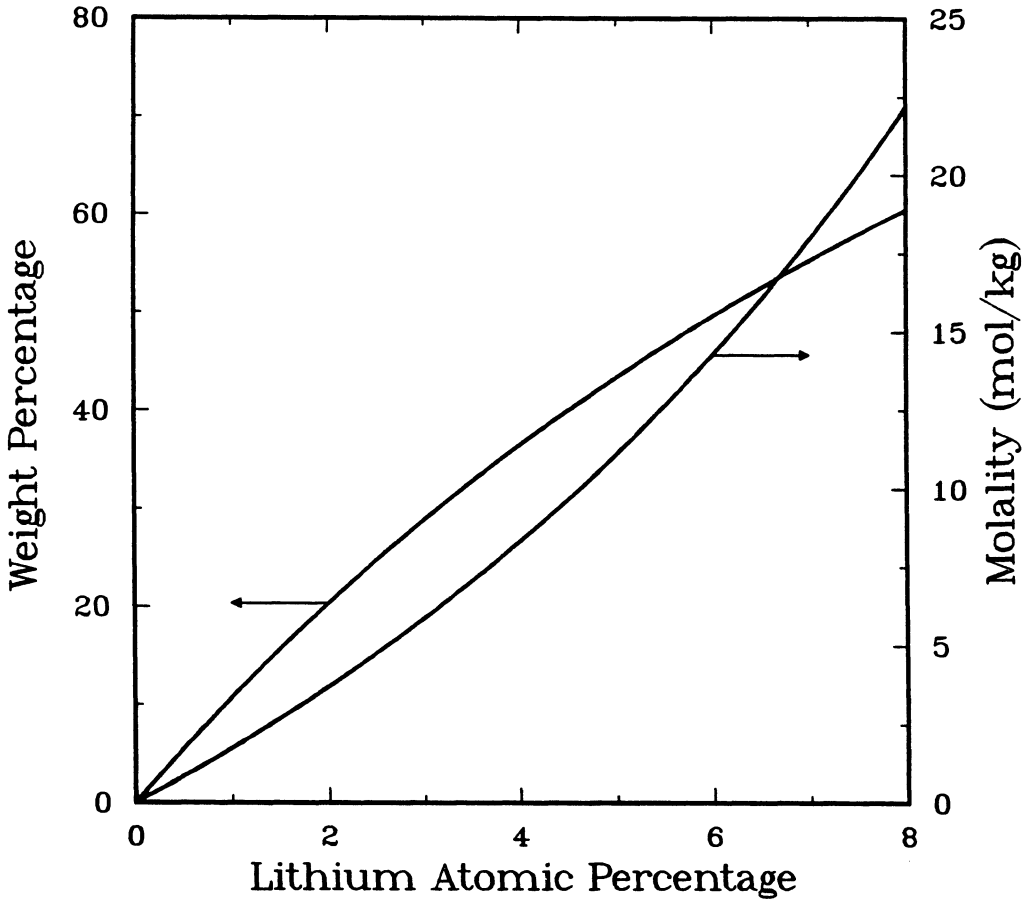

Figure 16.2-13. Relationship between molality and weight percentage of solute as a function of atomic percentage of Li for $LiNO_3$ solutions.

In many cases, experimental data for some physical properties of interest for $LiNO_3$ solutions are not available at high temperatures. Where this is the case, and reasonable extrapolations cannot be made, the corresponding data for NaCl solutions have been used because the NaCl–H_2O system has been much more widely studied than any other solution and many solutions of 1-1 electrolytes (*e.g.,* NaCl, KBr, and $LiNO_3$) have similar properties at the same concentrations. It is expected that such estimates should be accurate to about 20% [62], which is adequate for a worthwhile assessment of the thermal performance of the blanket.

16.2.3.1. Density

A full experimental data set is available for the density of $LiNO_3$ solutions for temperatures up to 350 °C and for concentrations from pure water to pure $LiNO_3$ [63,64]. In Reference [63], an expression is fitted to experimental data for weight percentages up to 40% and for temperatures up to 300 °C, the fit being accurate to better than 1.5% throughout the range. This data fit for the density, ρ, in g/cm^3 as a function of temperature, T (°C), is reproduced in the equation below:

$$\begin{aligned}\rho = \quad & 1.003 + 5.765 \times 10^{-3} W + 3.750 \times 10^{-5} W^2 \\ & - \left(1.898 \times 10^{-4} + 1.096 \times 10^{-5} W + 9.375 \times 10^{-9}\ W^2\right) T \\ & - \left(2.497 \times 10^{-6} - 6.500 \times 10^{-8} W + 4.229 \times 10^{-10} W^2\right) T^2 . \end{aligned} \quad (16.2\text{-}39)$$

In Reference [64], experimental data are given for weight percentages from 40% to 100% $LiNO_3$ and for temperatures up to 350 °C. To yield a smooth set of data over the entire range of temperatures and compositions under consideration, the fit has been used for the lower concentrations and the experimental data for the higher concentrations, with the data being slightly smoothed in the transition range between the two data sets. Figure 16.2-14 shows the density as a function of temperature for various values of the lithium-atom percentage. This figure shows that for the higher concentrations, density is significantly increased from the pure-water value, the difference being a factor of about two for a lithium-atom content of 8%.

No pressure dependence for the density was given in either of these references because the measurements were taken for saturation pressures. But the pressure dependence of the density is expected to be weak because the density of pure water rises by only $\sim 3\%$ as the pressure increases from 8.6 MPa (saturation) to 20 MPa.

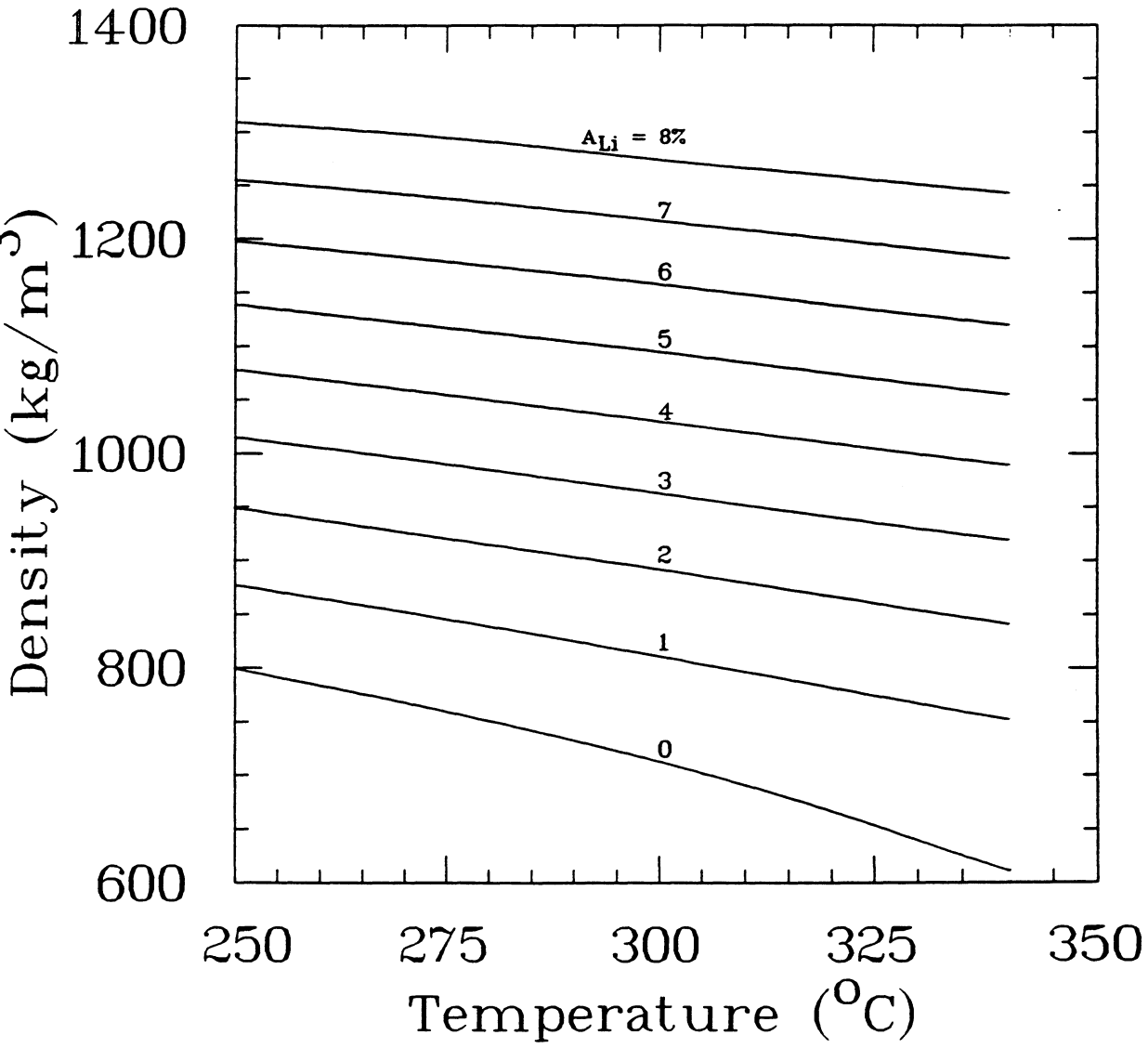

Figure 16.2-14. Density of $LiNO_3$ solutions at various temperatures and for a range of lithium-atom percentages.

A final point arising from these papers is that the authors note that $LiNO_3$ and H_2O are completely miscible at temperatures above the melting point of $LiNO_3$ (253 °C). This implies that there is effectively no upper limit to the salt concentration for high temperatures from solubility considerations.

16.2.3.2. Viscosity

The same Russian group that has published data concerning the density of $LiNO_3$ solutions at high temperatures has also reported measurements of the viscosity of these solutions. References [65,66] give experimental results for the viscosity of $LiNO_3$ solutions for temperatures up to 275 °C and for concentrations up to 10 mol/kg ($\sim$ 4.5% Li), and provide fits to these data. They quote a fit to the viscosity of the solution, η, relative to that of pure water, η_0, of the form

$$\ln\left(\frac{\eta}{\eta_0}\right) = \frac{AN}{1 - BN}, \qquad (16.2\text{-}40)$$

where A and B are temperature-dependent constants and N is the mole fraction of $LiNO_3$. Similar to the quoted fits for the density, no dependence of the viscosity on pressure was given, but since there is only an $\sim$ 5% variation in the viscosity of pure water as the pressure changes from saturation to 20 MPa at 300 °C, it appears reasonable to ignore this effect.

The fit is said to be valid [65,66] only for mole fractions up to 0.1 ($m \sim 6$ mol/kg, or $A_{Li} \sim 3\%$), although it reproduces the experimental data well up to 10 mol/kg. The relative viscosity at the high temperatures relevant to fusion blankets is almost constant with varying temperature for a given concentration. Equation 16.2-40 has therefore been applied throughout the concentration and temperature ranges of interest, using the values of $A = 4.10$ and $B = -1.8$ (for 250 °C), and the results are shown in Figure 16.2-15.

According to this fit, there is about a factor of 6 increase in the viscosity of the 8% $LiNO_3$ solution compared with that of pure water. This large change can have a significant effect on the thermal performance of the coolant, although some of the change is reduced by differences in other properties. As the data fit has been used well outside its quoted range of validity, it is important to recognize that there is a large degree of uncertainty associated with these values. However, the general trend in the values should be correct, and until better experimental data become available it is reasonable to use these estimates to assess the potential of $LiNO_3$ solutions as fusion-blanket coolants.

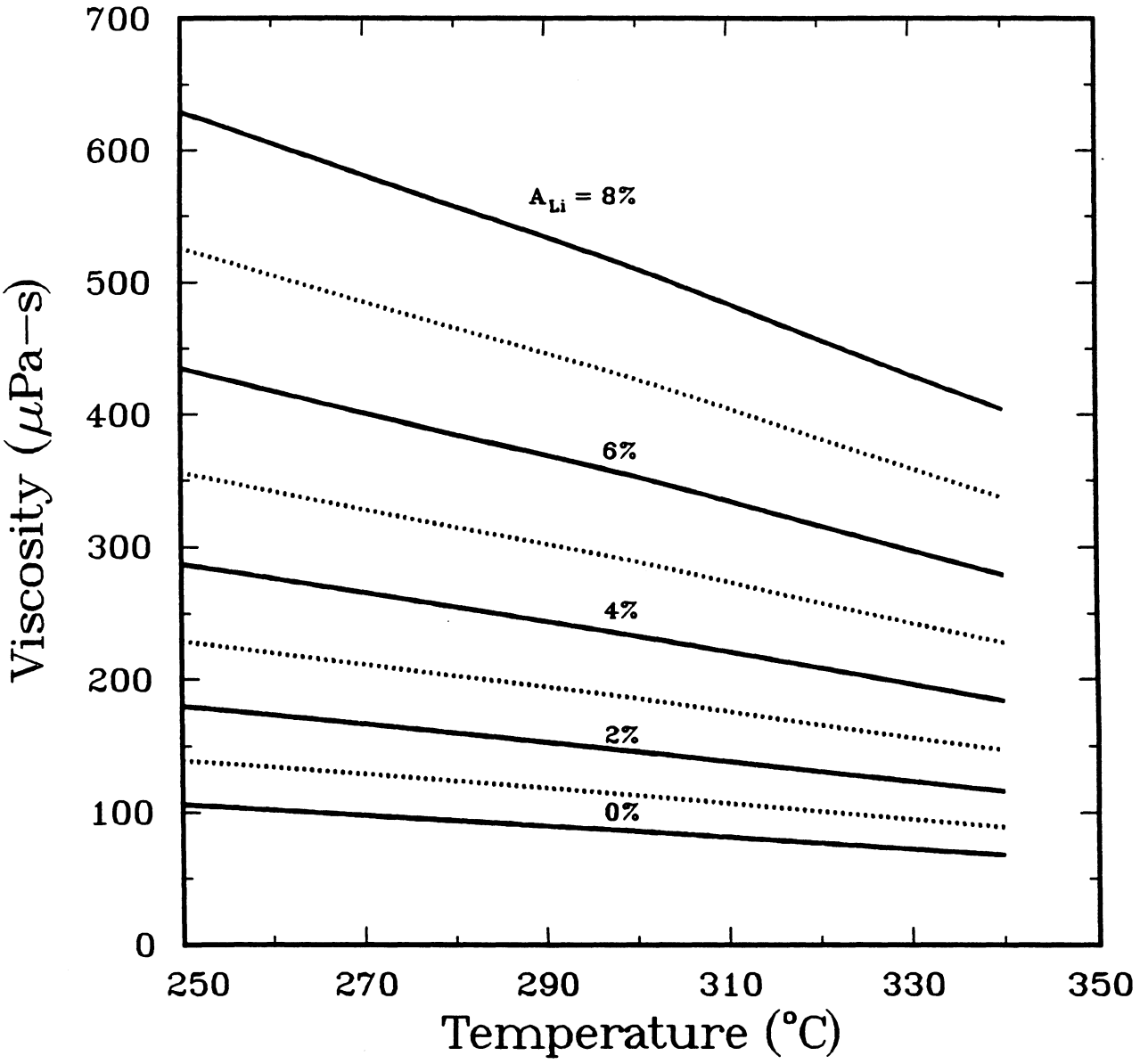

Figure 16.2-15. Viscosity of $LiNO_3$ solutions at various temperatures and for a range of lithium-atom percentages.

16.2.3.3. Specific heat capacity

The specific heat capacity is a more difficult quantity to predict by using a polynomial-type equation or by simply relating it to the value for pure water at the same temperature. The difficulty arises because the specific heat capacity of pure water becomes infinite as the critical point (374 °C and 22.1 MPa) is approached. The addition of even small quantities of a salt changes the critical temperature and pressure quite significantly. Therefore, the specific heat capacity of the solution can vary markedly from that of pure water at the same conditions. Wood and Quint have proposed a very simple way of estimating the specific heat capacity for aqueous salt solutions using a "corresponding-states" method [67]. In this method, the properties of the solution are approximated by the properties of water at the same "relative" conditions with respect to the critical point. The expression for the specific heat capacity of the solution, c_p, at temperature, T, and pressure, p, is

$$c_p(T,p) = W_0\left[c_{p0}(T',p') - c_{p0}(T',0) + c_{p0}(T,0)\right], \qquad (16.2\text{-}41)$$

where c_{p0} is the specific heat capacity of water, W_0 is the weight fraction of water, and T' and p' are, respectively, the reduced temperature and pressure and are given by

$$T' = \left(\frac{T}{T_c}\right) T_{c0}, \qquad (16.2\text{-}42)$$

$$p' = \left(\frac{p}{p_c}\right) p_{c0}. \qquad (16.2\text{-}43)$$

Here T_c and p_c are, respectively, the critical temperature and pressure of the solution and the subscript 0 refers to the properties of the pure water.

This approximation was tested for NaCl solutions up to 330 °C and 3 mol/kg and was found to give excellent agreement with experimental data, the largest error being about 3% at the highest temperatures and for the most concentrated solutions [67]. However, it should be noted that the heat capacity of the salt in the solution has been ignored in the calculation, which is likely to introduce a larger error for more concentrated solutions.

In order to use this method to estimate the specific heat capacity for $LiNO_3$ solutions, the critical temperature and pressure of the solution must be known as a function of concentration. No measurements for $LiNO_3$ salt appear to have been made, but data are available for many other salt solutions [68] and it has been found that many 1-1 electrolytes have very similar critical temperatures at the same molality. Since an extensive

data set is available for NaCl [69], these data have been used as a reasonable approximation for $LiNO_3$, although a large extrapolation has been made from the highest NaCl concentrations studied (6 mol/kg) to the most concentrated $LiNO_3$ solutions proposed.

Figure 16.2-16 shows the estimated critical temperature and pressure for $LiNO_3$ solutions. A rapid increase in the critical temperature and pressure with increasing salt concentration is evident from Figure 16.2-16, although the large extrapolation made for the higher concentrations makes these values rather uncertain. The possibility of operating an aqueous blanket at high temperatures (greater than 400 °C) is suggested by the increase in critical temperature, if the higher pressures can be tolerated and if suitable materials can be found for these conditions.

The data from Figure 16.2-16 have then been used to yield specific heat capacities of the aqueous salt solution, as illustrated in Figure 16.2-17. These data were evaluated for a pressure of 10 MPa, but the specific heat capacity varies by less than 1% for pressures up to 16 MPa, except for the case of pure water. Figure 16.2-17 shows an initial dramatic reduction in specific heat capacity as the salt is added to pure water, although there is little additional effect as the concentration is increased. The change in c_p is also offset somewhat by the associated increase in the density of the solution. It must be recognized that there is a large element of uncertainty in the specific-heat-capacity estimates, especially for the higher concentrations. This uncertainty is caused not only by the extrapolation made for the critical properties of the solution, but also by neglecting the contribution of the dissolved salt to c_p salt in the calculation. At low concentrations, this has little effect on the heat capacity of the solution, but as the weight fraction increases the contribution from the $LiNO_3$ becomes significant. The estimates presented here are, therefore, expected to be low for the higher concentrations.

16.2.3.4. Thermal conductivity

There appear to be no extensive experimental measurements of the thermal conductivity of $LiNO_3$ solutions for the temperature range of interest for fusion blankets. Data for NaCl are available, however, and Reference [70] gives smoothed values of experimental data for temperatures up to 330 °C and for concentrations up to 5 mol/kg. These data were extrapolated to 11 mol/kg ($A_{Li} \sim 5\%$) and a simple fit to the data was made. For higher concentrations, curve fits were used as the simple fit breaks down. The thermal conductivity of the solution, k (W/m K), is approximately given by

$$k = k_0 - (a - bm)\,m\,, \qquad (16.2\text{-}44)$$

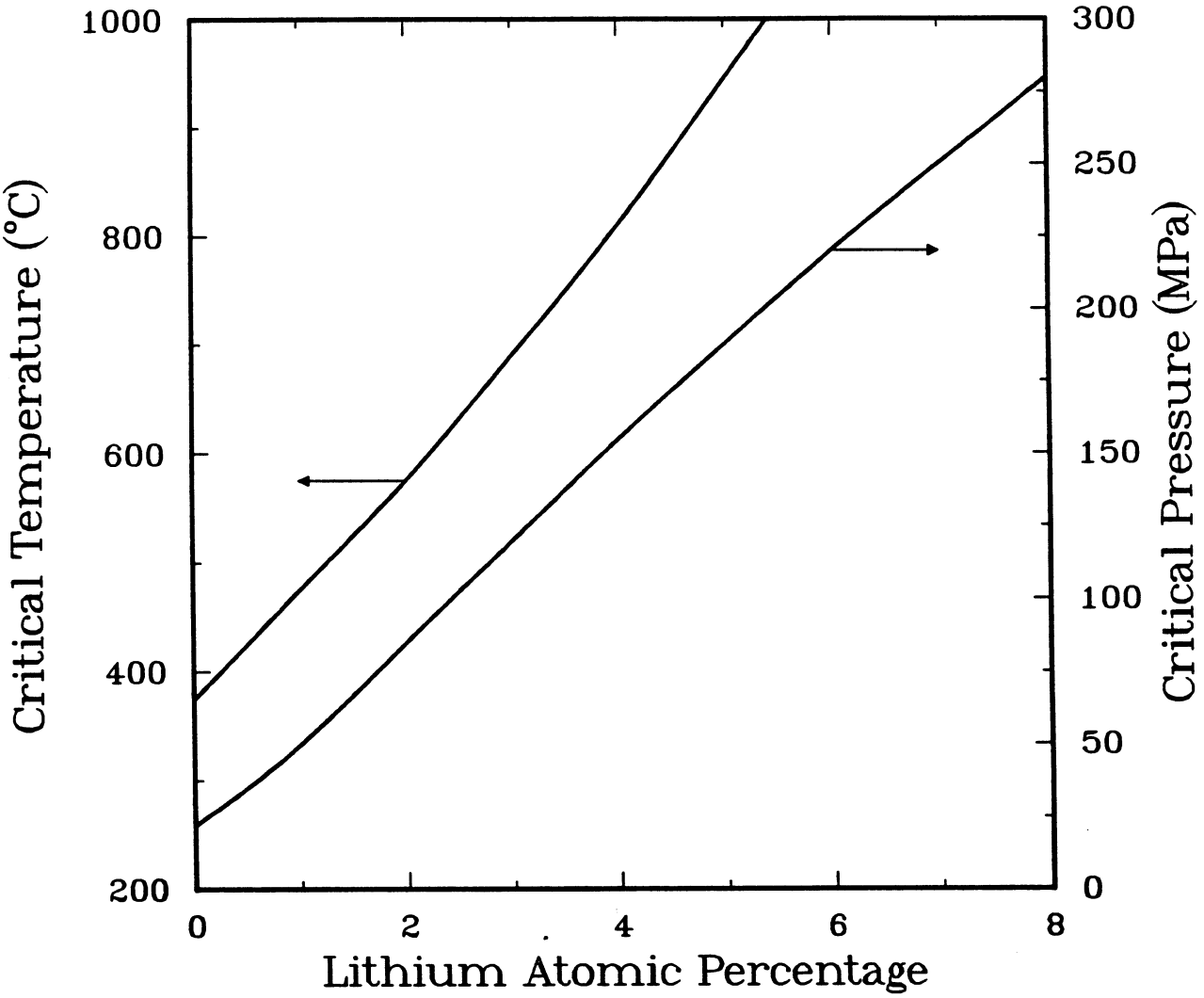

Figure 16.2-16. Critical temperature and pressure for $LiNO_3$ solutions as estimated from measurements for NaCl solutions.

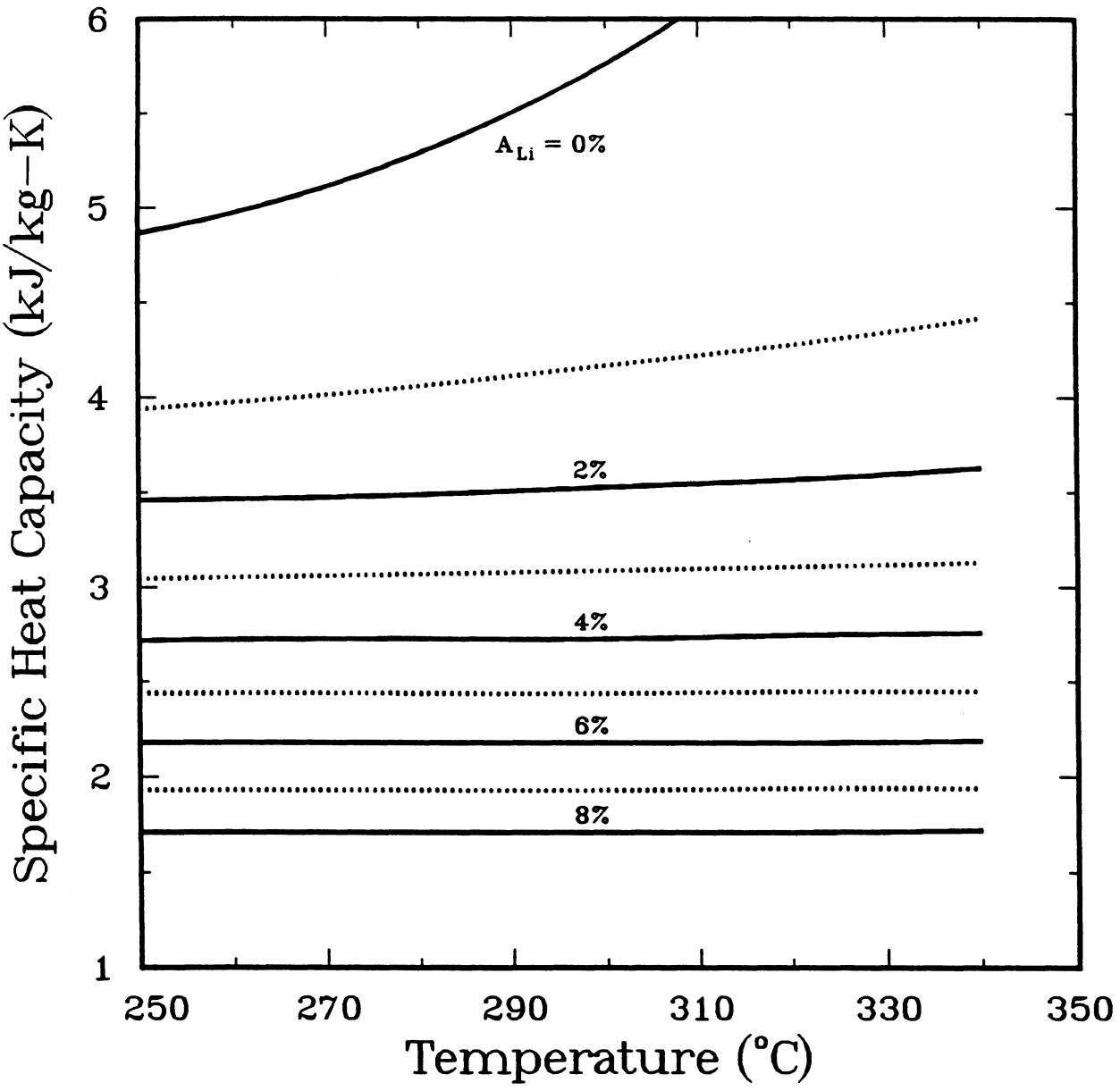

Figure 16.2-17. Specific heat capacity of $LiNO_3$ solutions at various temperatures and for a range of lithium-atom percentages.

$$a = 4.75 + 1.5 \times 10^{-2} T, \quad (16.2\text{-}45)$$

$$b = 0.185 + 5.0 \times 10^{-4} T, \quad (16.2\text{-}46)$$

where k_0 is the thermal conductivity of pure water, m is the molality in mol/kg, and T is the temperature in °C.

Estimates for the thermal conductivity are shown in Figure 16.2-18. These estimates suggest that the difference in the thermal conductivity of the solution compared with that of pure water is not as marked as for other properties. However, as the original NaCl data are not precise, and these results have been extrapolated to higher concentrations and applied to $LiNO_3$ solutions, the values shown here should be taken as indicative of the expected trends for the property rather than precise measurements. Further experimental data are required for a more exact assessment of the thermal performance of the coolant.

16.2.3.5. Boiling point

Reference [71] reported measurements of the vapor pressure of $LiNO_3$ solutions for concentrations up to 24 mol/kg and for temperatures up to 110 °C. Their results showed that the relative vapor pressure (the ratio of the vapor pressure of the solution to that of pure water) for a given concentration remained approximately constant, independent of changes in temperature. It has been assumed that this relationship is valid for higher temperatures, in the absence of relevant experimental data. The boiling point of the solution is then evaluated by finding the temperature at which the vapor pressure is equal to the applied pressure. Figure 16.2-19 shows these results for pressures ranging from 4 to 16 MPa. These estimates of the boiling point indicate that the boiling point of the $LiNO_3$ solution should be significantly higher than of pure water. For a lithium-atom percentage of 5%, the increase is 40 to 50 °C, which has a major effect on the thermal design of the fusion blanket.

Once again, a note of caution is necessary because the accuracy of these estimates is uncertain since an extrapolation was made from the lower temperature results. For example, LiOH solutions show a saturation in the boiling-point elevation with increasing concentration at higher temperatures [46], although this is caused by the association of the ions into LiOH molecules which is not expected to occur with $LiNO_3$. Further experimental data are clearly required.

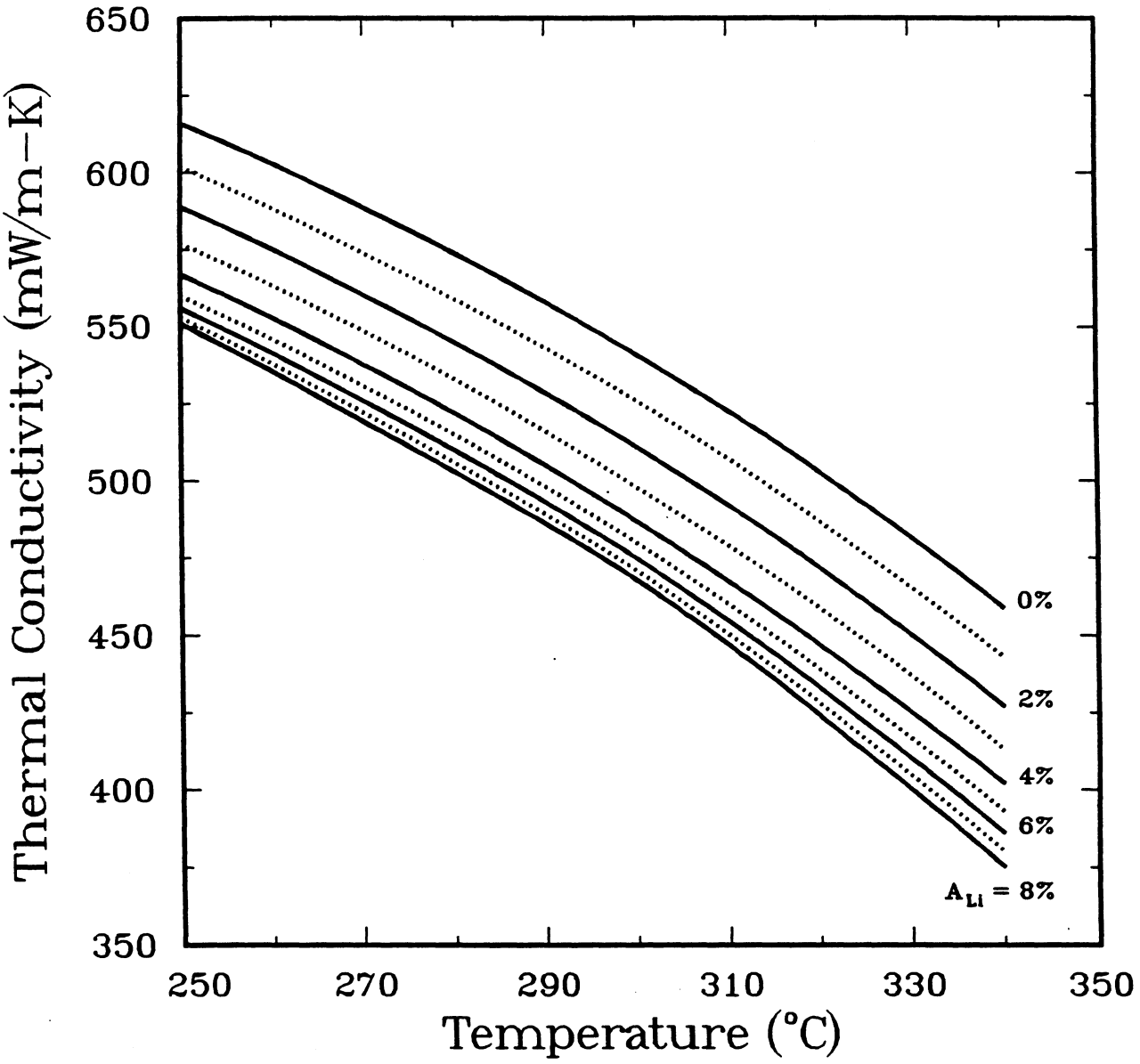

Figure 16.2-18. Thermal conductivity of $LiNO_3$ solutions at various temperatures and for a range of lithium-atom percentages.

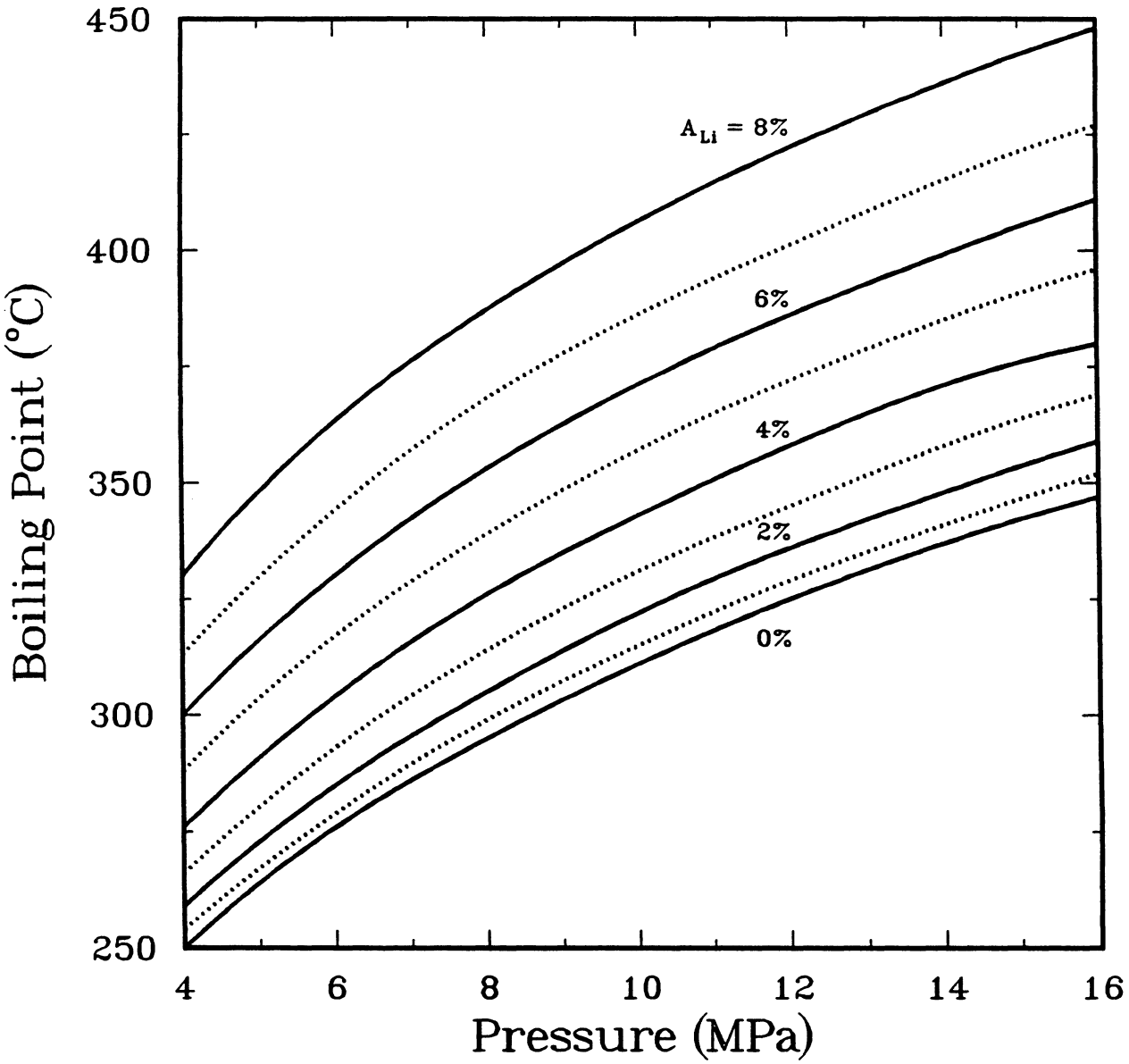

Figure 16.2-19. Boiling temperatures of $LiNO_3$ solutions at various pressures and for a range of lithium-atom percentages.

16.2.3.6. Discussion

The above estimates of the properties of $LiNO_3$ solutions at high temperatures exhibit marked differences from the properties of pure water. Therefore, the exact coolant conditions should be considered in designing the blanket. The thermal-hydraulic design of an aqueous salt blanket can be very different from that of a water-cooled design, and advantage can be taken of the differences in properties by, for example, reducing the coolant pressure or increasing the temperature without incurring an increased risk of burnout.

However, many of the estimates are extrapolations from experimental data or have been obtained from the results for other salt solutions. Although these predictions should give good indications of the expected trends for the various properties, a much expanded experimental data base is required for the salts and conditions proposed before the thermal performance of an aqueous salt blanket at high temperature can be confidently predicted.

16.2.4. Structural Material

One of the goals of the TITAN study has been to satisfy Class-C waste-disposal criteria [72] and achieve a high level of safety assurance. Among the low-activation candidate vanadium alloys, V-3Ti-1Si (the structural material for the TITAN-I design) had to be ruled out because of its poor water-corrosion resistance. Other vanadium alloys which contain chromium (*e.g.*, V-15Cr-5Ti) show excellent resistance to corrosion by water coolant but their properties are inferior to those of ferritic steels when helium-embrittlement effects are taken into account [73] (Section 10.2). Therefore, various steels were considered as TITAN-II structural material.

Irradiation of commercial steels in a fusion environment produces long-lived radioactive isotopes. Acceptable levels of activation for near-surface burial have been established by the U. S. Nuclear Regulatory Commission (U. S. – NRC). These limits are published in the U. S. Code of Federal Regulations, 10CFR61 [72]. The 10CFR61 list was compiled to establish concentration limits (Ci/m^3) for fission-reactor waste streams. In recent years, the 10CFR61 list of radionuclide concentrations have been augmented to include radionuclides important to fusion [74,75]. A list of limiting-specific activities for near-surface burial of all radionuclides with atomic numbers less than 84 was recently compiled by Fetter [76]. One should note that some discrepancies exist between Fetter's evaluations and those of 10CFR61. Furthermore, Fetter's evaluations includes nuclides

Table 16.2-XI.

10CFR61 CLASS-C DISPOSAL LIMITS OF SELECTED ALLOYING ELEMENTS OF STEELS [77]

Element	Product	Half-Life (y)	Disposal Limit (Ci/m^3)
N	^{14}C	5730	80
Ni	^{59}Ni	76000	220
	^{63}Ni	100	7000
Nb	^{94}Nb	20000	0.2
Mo	^{94}Nb	20000	0.2
	^{93}Mo	3500	30
W	^{192}Ir	241	1
	^{193}Pt	50	200000

not covered by the 10CFR61 code (Sections 13.7 and 19.5). Disposal limits of the major alloying elements used in commercial steels such as N, Ni, Nb, Mo, and W are listed in Table 16.2-XI [77].

Effort has been made to develop low-activation alloys by replacing those alloying elements that would not qualify for Class-C waste disposal with more suitable ones, without compromising mechanical properties. As a result of these reduced-activation-alloy studies, three steels have been produced: (1) Ti-modified 316 austenitic steels, (2) $2\frac{1}{4}$ Cr ferritic/bainitic steels, and (3) 9- to 12-Cr ferritic/martensitic steels. A major advantage of the ferritic steels over austenitics is their excellent resistance to void swelling. Figure 16.2-20 shows a comparison of the relative swelling rates of austenitic alloys with those of ferritic steels [78]. Furthermore, ferritic steels have a higher thermal-stress resistance compared to austenitic steels [77]. These characteristics prompted the choice of a ferritic steel as the structural material for the TITAN-II design.

Currently three major research institutions in the U. S. are developing and evaluating low-activation ferritic alloys [79]: Oak Ridge National Laboratory (ORNL), General

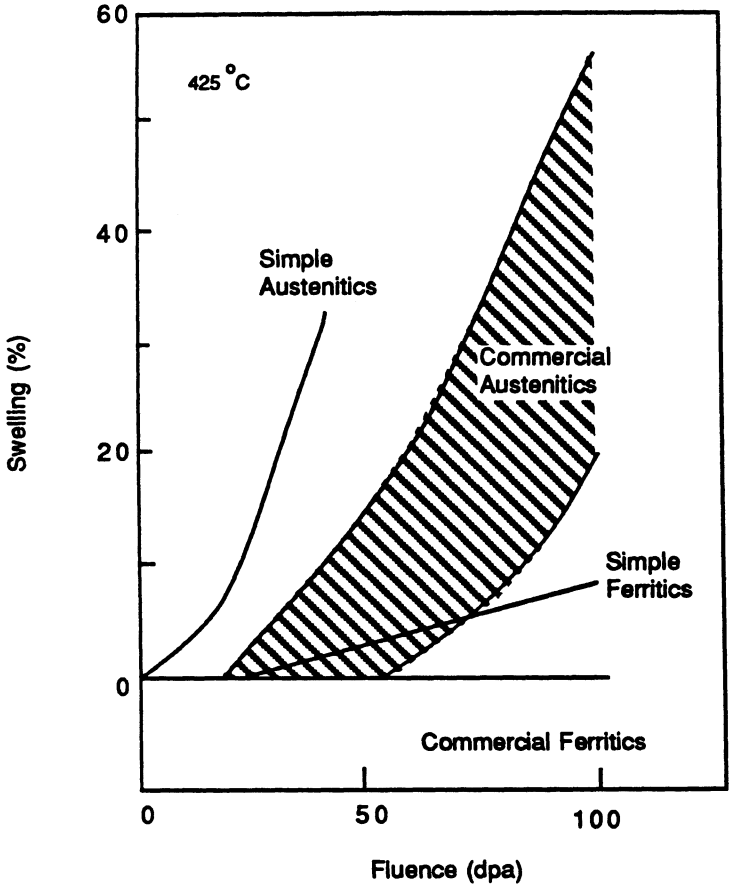

Figure 16.2-20. Comparison of swelling behavior of austenitic and ferritic steels [78].

Atomics (GA), and Hanford Engineering Development Laboratory (HEDL). The ORNL program has developed a series of low-chromium and 9%-12% Cr ferritic alloys termed fast-induced-radioactivity-decay alloys (FIRD). In the FIRD alloys, molybdenum is replaced by tungsten, which is in the same group as molybdenum. About 0.25 wt.% of vanadium is also added to increase the strength through vanadium-carbide formation. The low-chromium and 9-Cr steels were all 100% martensitic, while the 12-Cr steel contained about 26% delta-ferrite. The 12-Cr steel is, therefore, expected to have a lower hardness and a higher ductile-to-brittle transition temperature (DBTT) than the 100% martensitic steels. Tensile-behavior tests have verified the strengthening effect of vanadium and tungsten. The effects of irradiation on tensile properties of FIRD steels are being evaluated in specimens irradiated in the Fast-Flux Test Facility (FFTF) [79].

The GA program has concentrated on 9% and 12%-Cr ferritic alloys, referred to as GA3X and GA4X, respectively. Various combinations of Cr-W-V-C were developed and evaluated. The tungsten additions are as high as 2.5% and vanadium content is about

0.3%. A low-carbon concentration, below 0.15%, was chosen to ensure weldability. The low-vanadium concentration resulted in high $M_{23}C_6$ precipitate formation in tempered-steel samples. Generally, precipitate formation results in a decrease in elongation; the total elongation of the GA3X was found to be about 50% lower than that of its commercial counterpart alloy 9Cr-1Mo-V-W [80].

The emphasis of the HEDL program has been in replacing molybdenum with vanadium rather than with tungsten. These alloys are sometimes referred to as low-activation ferritic steels. To avoid delta-ferrite formation, manganese is added to the high-chromium alloys and carbon contents are kept very low (< 0.1 wt.%). To compensate for the effects of carbon as a solute strengthener, the manganese content had to be increased substantially ($\sim 6.5\%$ Mn). Compared with $2\frac{1}{4}$Cr-1Mo, the low-chromium bainitic alloy ($2\frac{1}{4}$Cr-V) has a lower yield strength, a slightly lower ultimate tensile strength, and a much higher elongation [79]. On the other hand, the 12-Cr martensitic alloys show a higher strength with comparable elongation when compared with commercial 12Cr-1Mo-V-W steels [79].

The effects of irradiation on the low- and high-chromium alloys were also investigated [2] and the latter alloys were found to be superior. Under irradiation, the $2\frac{1}{4}$Cr-V alloys showed an increase in strength and a reduction in elongation, while the 9 to 12Cr-Mn-V-W alloys exhibited only small changes in strength and elongation after irradiation at 420 °C and damage doses up to 10 dpa [2]. The radiation-hardening resistance of high-chromium alloys is also significantly different from commercial high-chromium ferritic steels such as 9Cr-1Mo-V-Nb and 12Cr-1Mo-V-W (HT-9) [79,81].

Some data on irradiation behavior of the low-activation ferritic steels are available. Specimens were irradiated up to 14 dpa in the FFTF and post-irradiation tests were performed at room temperature. Figure 16.2-21 shows a comparison of the yield strength and total elongation of low-activation ferritic steels as a function of irradiation temperature (values on the vertical axis corresponding to the unirradiated specimen). Figure 16.2-21 shows that $2\frac{1}{4}$Cr-V alloys experience an increase in strength of about 200 MPa when irradiated at 420 °C. At 585 °C, however, these alloys show a reduction of strength compared with unirradiated alloys. The high-chromium alloys show much smaller irradiation-hardening effects at 420 °C. A reduction in strength at 585 °C is also experienced by the high-chromium alloys, but the decrease is not as much as that of the low-chromium alloys. The 12Cr-0.3V-1W-6.5Mn martensitic steel shows the smallest degree of irradiation hardening and the lowest decrease in strength of all tested alloys. Figure 16.2-21 also shows the total elongation of the tested specimen. Again 12Cr-0.3V-1W-6.5Mn martensitic steel shows the smallest fluctuations in total elongation among all tested alloys.

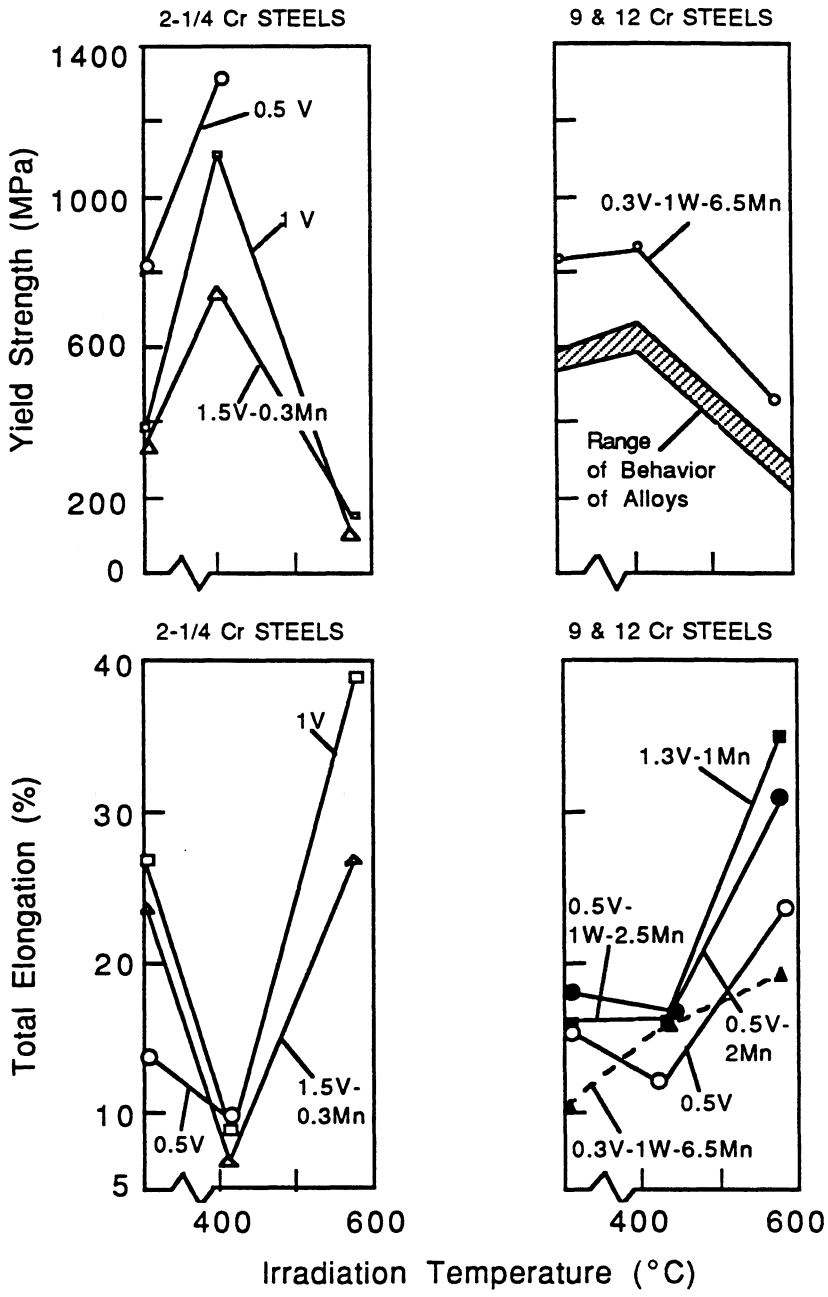

Figure 16.2-21. Results of uniaxial-tensile tests of HEDL low-activation ferritic alloys [79]. The yield strength and the total elongation are plotted as a function of the irradiation temperature. The values on the vertical axis denote the corresponding values for an unirradiated specimen.

The ductile-to-brittle transition temperature (DBTT) of some ferritic alloys may be a potential problem. The DBTT is the temperature at which the fracture stress is reached during loading of a specimen prior to the onset of the yield. When a specimen is loaded at a temperature below the DBTT, a brittle-type cleavage fracture occurs, while at temperatures above the DBTT the metal undergoes yielding before fracture occurs. Figure 16.2-22 shows changes in DBTT of 9Cr-1Mo-W-Nb and 12Cr-1Mo-W-V (HT-9) irradiated to damage levels of up to 30 dpa as a function of irradiation temperature. The change in DBTT is highest at low irradiation temperatures, and vanishes when irradiation temperatures exceed 600 °C. The commercial 9-Cr alloy shows overall smaller increases in DBTT when compared with HT-9. Recently, Lechtenberg [82] investigated the DBTT of the reduced-activation 9Cr-2W-0.15C stabilized martensitic steel. The DBTT of the unirradiated specimen was -24 °C. When irradiated at 356 °C to damage dose of 10.5 dpa, the DBTT increased to about 0 °C. The measured increase on DBTT of 24 °C is the

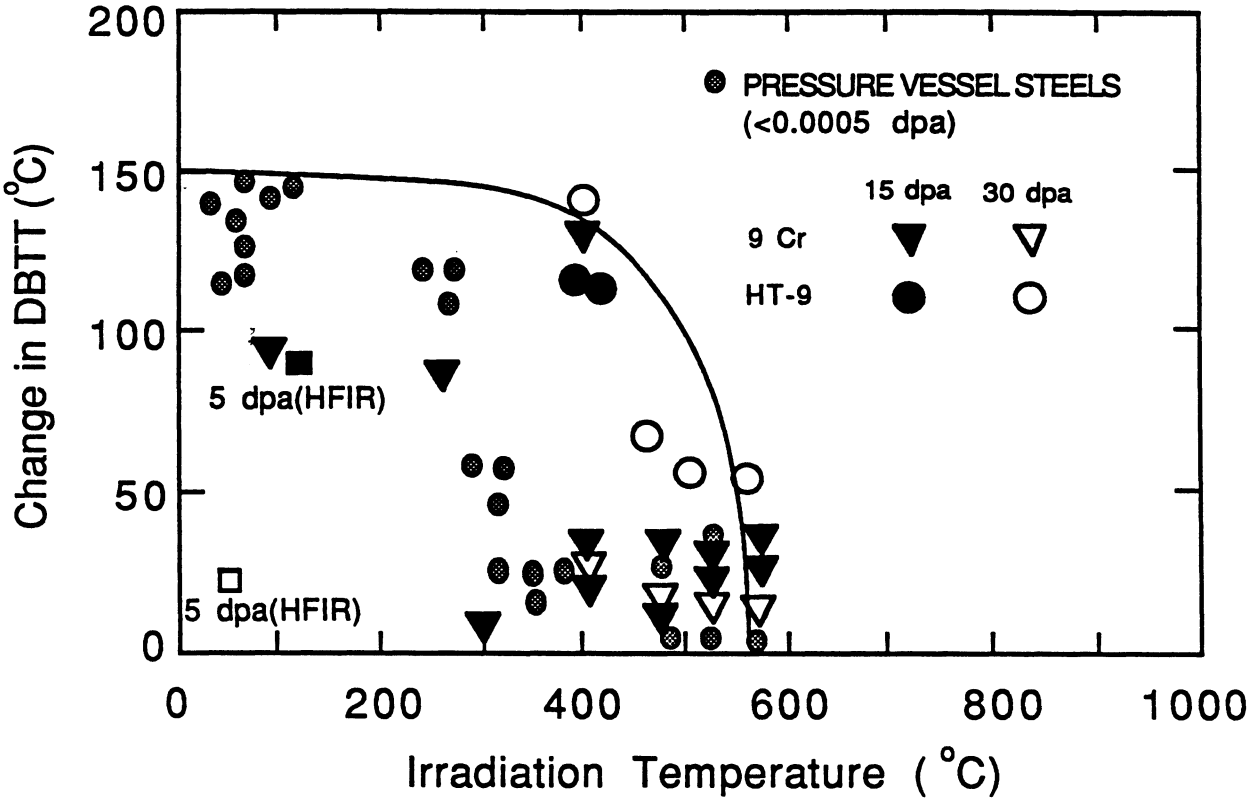

Figure 16.2-22. Change in the DBTT as a function of irradiation temperature for 9Cr-1Mo-W-Nb and HT-9 ferritic steels [82].

smallest increase reported among all the low-activation ferritic alloys studied. The DBTT of tested ferritics clearly indicates a potential problem. Until alloy-development efforts alleviate this problem, operating conditions must be chosen to minimize the rise in DBTT of ferritic steels.

16.2.4.1. Discussion

The TITAN-II FPC is cooled by a aqueous lithium-salt solution which also acts as the breeder material [1]. Among the low-activation candidate vanadium alloys, V-3Ti-1Si (the structural material for the TITAN-I design) had to be ruled out because of its poor water-corrosion resistance. Other vanadium alloys which contain chromium (*e.g.*, V-15Cr-5Ti) show excellent resistance to corrosion by water coolant but their properties are inferior to those of ferritic steels when helium-embrittlement effects are taken into account [73] (Section 10.2). Therefore, various steels were considered as TITAN-II structural material.

Reported results of the low-activation ferritic-steel development program indicate that a reduced-activation alloy can be developed without compromising mechanical properties, primarily by replacing Mo with W. However, recent evaluations of radionuclides produced from tungsten alloys indicate that W may be a potential activation-limited element [83]. Nevertheless, it should be possible to develop low-activation ferritic steels.

For the TITAN-II reactor, the HEDL/UCLA 12Cr-0.3V-1W-6.5Mn alloy (9-C) has been chosen as the structural material, primarily because of its high strength and good elongation behavior after irradiation as compared with other low-activation ferritic steels. The high-chromium content of this alloy ensures an excellent corrosion resistance, as is discussed in detail in Section 16.2.1. The low carbon content of this alloy results in good weldability, high sensitization resistance (Section 16.2.1.1), and a reduction of hydrogen-embrittlement susceptibility (Section 16.2.5). Furthermore, alloy 9-C has a low tungsten content ($< 0.9\%$) which reduces the waste-disposal concerns of the production of the radionuclide ^{186m}Re by fusion-neutron reaction with W. The high concentration of manganese in 9-C prevents the formation of delta-ferrite phases, which is responsible for high DBTT and low hardness.

Table 16.2-XII shows selected properties of the 9-C alloy which was used throughout the TITAN-II study. The composition (wt.%) of the 9-C alloy was determined by the vendor as: 11.81Cr, 0.097C, 0.28V, 0.89W, 6.47Mn, 0.11Si, 0.003N, $<$ 0.005P, and 0.005S with balance in iron.

Table 16.2-XII.

PHYSICAL AND MECHANICAL PROPERTIES OF ALLOY 9-C LOW-ACTIVATION FERRITIC STEEL [2]

Property	Temperature (°C)				
	RT	300	400	500	600
Young's modulus (GPa)	225	200	193	180	150
Poisson ratio	0.4	0.4	0.4	0.4	0.4
Shear modulus (GPA) [a]	83	75	72	68	–
Tensile strength (MPa)	1002	–	810[a]	942[b]	749[c]
Yield strength (MPa) [c]	810	810	820	650	531
Total elongation (%) [c]	10.1	13.8	15.0	17.0	19.4
Thermal-expansion coefficient (10^{-6}/°C)	9.5	10.5	11.0	11.5	12.0
Specific heat (J/kg-°C)	450	570	600	680	780
Electric resistivity ($\mu\Omega$ m)	0.6	0.82	0.9	0.99	1.05
Thermal conductivity (W/m-K)	25	26.5	26.7	27.2	27.6
DBTT at 15 dpa (°C) [a]	–	–	100	25	0
DBTT at 30 dpa (°C) [a]	–	–	140	50	55

(*a*) Data unavailable, corresponding values for HT-9 were used.

(*b*) Values at irradiation temperatures after 6 dpa.

(*c*) Values at irradiation temperatures after 14 dpa.

16.2.5. Hydrogen Embrittlement

Interaction of hydrogen with metals can lead to one of the many forms of failures collectively termed "hydrogen damage." The term "hydrogen embrittlement" has been used freely in the past to describe any one of the many forms of hydrogen damage. Specific types of hydrogen damage have been categorized by Craig [84] based on the following property degradation processes.

Hydrogen environment embrittlement. This failure mode occurs during the plastic deformation of stressed alloys exposed to hydrogen-bearing gases or during hydrogen-producing corrosion reactions. Experiments show that steels, nickel-base alloys, and titanium alloys are most susceptible to this mechanism when the strain rate is low and the hydrogen pressure and purity is high.

Hydrogen stress cracking. Normally, ductile alloys can fail by brittle fracture under sustained loads in the presence of hydrogen. Hydrogen stress cracking starts by absorption of hydrogen. The hydrogen then diffuses into regions of high triaxial stresses. The diffusion and agglomeration manifests itself in a delayed time-to-failure (incubation time). Furthermore, this failure mode is often characterized by a threshold stress below which hydrogen stress cracking does not occur. The threshold stress generally decreases as the yield strength and tensile strength of an alloy increase. Thus, hydrogen stress cracking is not seen very often in low-strength alloys.

Loss in tensile ductility. Lower-strength alloys exposed to hydrogen can show a marked reduction in area (*i.e.,* loss of ductility during tensile-stress tests). The extent of loss in ductility is a direct function of the hydrogen content of the metal.

Hydrogen attack. Hydrogen may enter the steel and react with carbon to form volatile methane gas. The alloy undergoes decarburization and shows marked crack formations. This form of hydrogen damage is a high-temperature (T >200 °C) process that occurs in carbon and low-alloy steels exposed to high-pressure hydrogen. Although the limits of alloy content for certain groups of steels are not well defined, it is assumed that a "low-alloy" steel is one having less than 12% total alloy content; above that level the term stainless steel is used [85].

Blistering. In low-strength alloys, atomic hydrogens can be trapped at internal defects and consequently form molecular hydrogen (H_2). Localized plastic deformation can occur when the pressure of the H_2 gas reaches a large value, leading to blistering and can cause rupture.

Shatter cracks. Melts of alloys possess a higher hydrogen solubility than the solids. Therefore, during forging, welding, and casting, hydrogen pickup is increased. When the melt cools down, the solubility of hydrogen decreases and results in an agglomeration of hydrogen at internal trap sites. The effects of this process are similar to those of blistering.

Micro-perforation. Steels exposed to very high hydrogen pressures at near room temperature often show the formation of networks of fissures. Consequent exposure to gases or liquids will result in a rapid permeation of the alloy.

Degradation in flow properties. The interaction of atomic hydrogen with dislocations can enhance the dislocation motion and also create dislocations at surfaces or crack tips, leading to softening of the material on a localized scale. This enhanced plastic flow has been found at ambient temperatures for iron and steels and is observed as an increase in the steady-state creep rate.

Hydride formation. Atomic hydrogen can react with metals to form corresponding hydrides (MH_x). Precipitation of metal-hydride phases results in the degradation of the mechanical properties and cracking in magnesium, tantalum, niobium, vanadium, uranium, thorium, zirconium, titanium, and their alloys. Hydride formation is enhanced under stress and leads to an increase in hydrides around the crack tip, resulting in a degradation of ductility near crack-tip regions.

Hydrogen embrittlement encompasses only the first three of the above-mentioned processes: hydrogen environment embrittlement, hydrogen stress cracking, and loss in tensile ductility. Hydrogen embrittlement is caused primarily by the atomic, diffusible, or nascent hydrogen (H) content, and not by those processes caused by the total hydrogen content which may also include molecular hydrogen (H_2). In a non-nuclear environment, there are three sources of hydrogen: steel manufacturing, corrosion in aqueous solutions

(cathodic reactions generate hydrogen atoms at the metal surface), and in-service environment. A fourth source of hydrogen is added when metals and alloys are exposed to neutron irradiation. Hydrogen is generated as a result of (n,p) nuclear reactions. Furthermore, the metal or alloy must also be under an externally applied stress for a specific type of hydrogen damage to be termed hydrogen embrittlement. There are three sources of stress: applied stress, residual stress from heat treatment, and residual stress from welding or plastic deformation. These sources of stress further complicate the identification of a specific cause of hydrogen embrittlement.

To minimize hydrogen embrittlement, the following classification is helpful: (1) internal, reversible hydrogen embrittlement, and (2) hydrogen-reaction embrittlement [86]. For hydrogen embrittlement to be fully reversible, it must occur without the hydrogen undergoing any type of chemical reaction within the lattice. By relieving the applied stress and by aging steels at room temperature, ductility can be restored if micro-cracks have not yet developed. Hydrogen-reaction embrittlement, on the other hand, is generally not reversible by aging at room temperature. After having been absorbed, hydrogen can react near the surface or diffuse further into the lattice before undergoing a reaction. Hydrogen can react with itself to form H_2, with the matrix to form a metal hydride (MH_x), or with foreign elements in the matrix to form a gas (CH_x). In carbon and low-alloy steels, the primary gas formed is methane (CH_4). The volatility of the methane gas leads to the process known as decarburization. Hydrogen can also react with oxygen to form steam (H_2O) inside the matrix. Copper alloys are highly susceptible to steam formation which results in blistering and porous metal components [86].

Much confusion exists in the relationship between stress-corrosion cracking (SCC) and hydrogen embrittlement because the crack-growth mechanism of both processes is the same. For SCC to occur, the crack has to be in contact with the aqueous solution. During the corrosion process in aqueous solutions, atomic hydrogen is generated and is then absorbed by the crack tip. Stress-corrosion cracking is, therefore, a special case of hydrogen embrittlement in which hydrogen is produced by the corrosion process occurring inside the crack.

16.2.5.1. Hydrogen embrittlement of ferrous alloys

During 1960s, the National Aeronautics and Space Administration (NASA) experienced failure of ground-based hydrogen-storage tanks. Because of these failures and the anticipated use of hydrogen in advanced rocket and gas turbines, hydrogen environment embrittlement was recognized as a serious problem and NASA initiated research efforts

in these areas. Conferences on the subject of hydrogen embrittlement are held frequently, mostly sponsored by the National Association of Corrosion Engineers (NACE) and published under the International Corrosion Conference series [87]. As a result of the research efforts over the past decades, factors influencing hydrogen embrittlement in various alloys have been identified. The following is a summary of important factors in ferrous alloys. More detailed discussions are given in References [84 - 90].

The primary factors that affect the behavior of ferrous alloys in a hydrogen-bearing environment are: (1) hydrogen concentration, (2) temperature, (3) heat treatment, (4) microstructure, (5) stress level, and (6) environment. The tendency for hydrogen embrittlement to occur increases with hydrogen concentration in the metal. Figure 16.2-23 shows that after a given length of time, cracking occurs at successively higher stresses as the hydrogen content in the metal is reduced by the baking treatment [91]. In general, increasing the concentration of hydrogen in an alloy will reduce the time-to-failure and the stress levels at which failure occurs [84].

Hydrogen concentration inside the alloy is generally a function of many factors such as the approximate concentration of hydrogen at the surface exposed to the environment, hydrogen-adsorption characteristics of the surface, and amount of trapped hydrogen inside the matrix. Trapping occurs by binding hydrogen to impurities or structural defects. Structural traps may be mobile (*e.g.,* dislocations and stacking faults) or they can be stationary (*e.g.,* voids, grain boundaries, carbide particles, and solute atoms). The trapping at structural defects is believed to be the major cause of increased hydrogen embrittlement in heavily cold-worked ferritic steels. The microstructure of the alloy can have a profound effect on the resistance of steels to hydrogen embrittlement. A quenched and tempered fine-grain microstructure is more resistant to cracking than a normalized steel [92]. The effect of the grain size on the resistance to hydrogen embrittlement is illustrated in Figure 16.2-24 which shows that as the grain size of an alloy is reduced, the resistance to hydrogen damage is increased.

Another microstructural feature which affects hydrogen embrittlement is the concentration of precipitate particles (trap sites) dispersed in the alloy. Measurements of the effective diffusion coefficient of hydrogen as a function of precipitate particles (Figure 16.2-25) show a marked decrease in the diffusion of hydrogen with an increased concentration of particles [93]. The apparent diffusion coefficient is an indirect measure of the trapping strength of the matrix since, once trapped, a diffusing species must undergo de-trapping before diffusion can proceed. In general, the most resistant microstructure is a highly tempered martensitic structure with equiaxed ferrite grains and spheroidized carbides evenly distributed throughout the matrix [84].

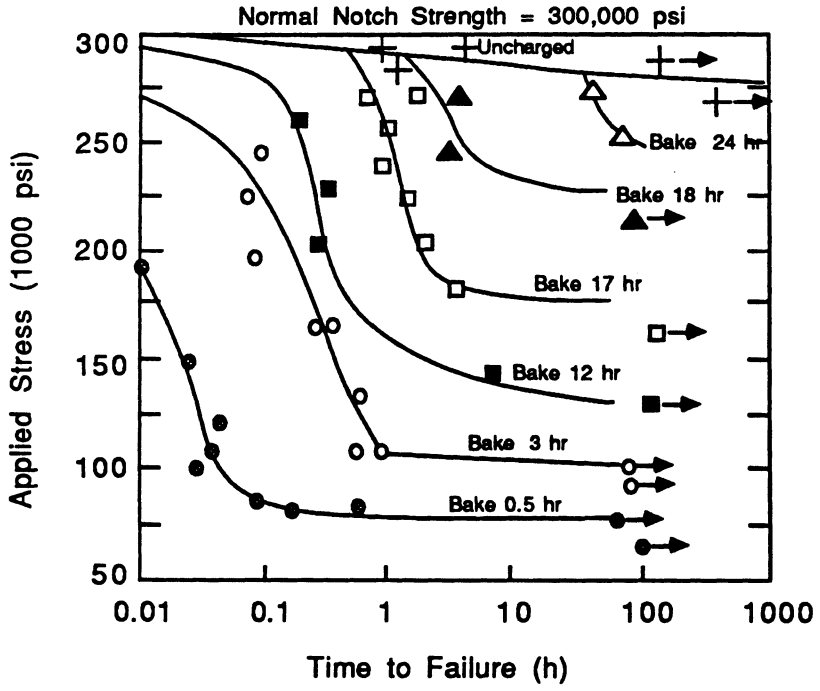

Figure 16.2-23. Static fatigue curves of AISI 4340 steels for various hydrogen concentrations obtained by different baking times at 150 °C. Arrows indicate very long time-to-failure [91].

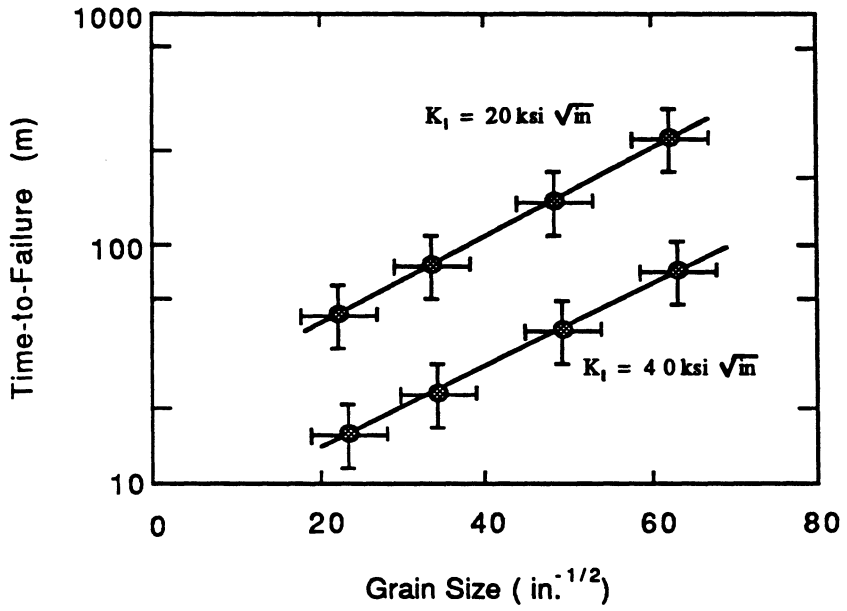

Figure 16.2-24. Effects of grain size on the resistance of AISI 4030 steels to hydrogen failure [92].

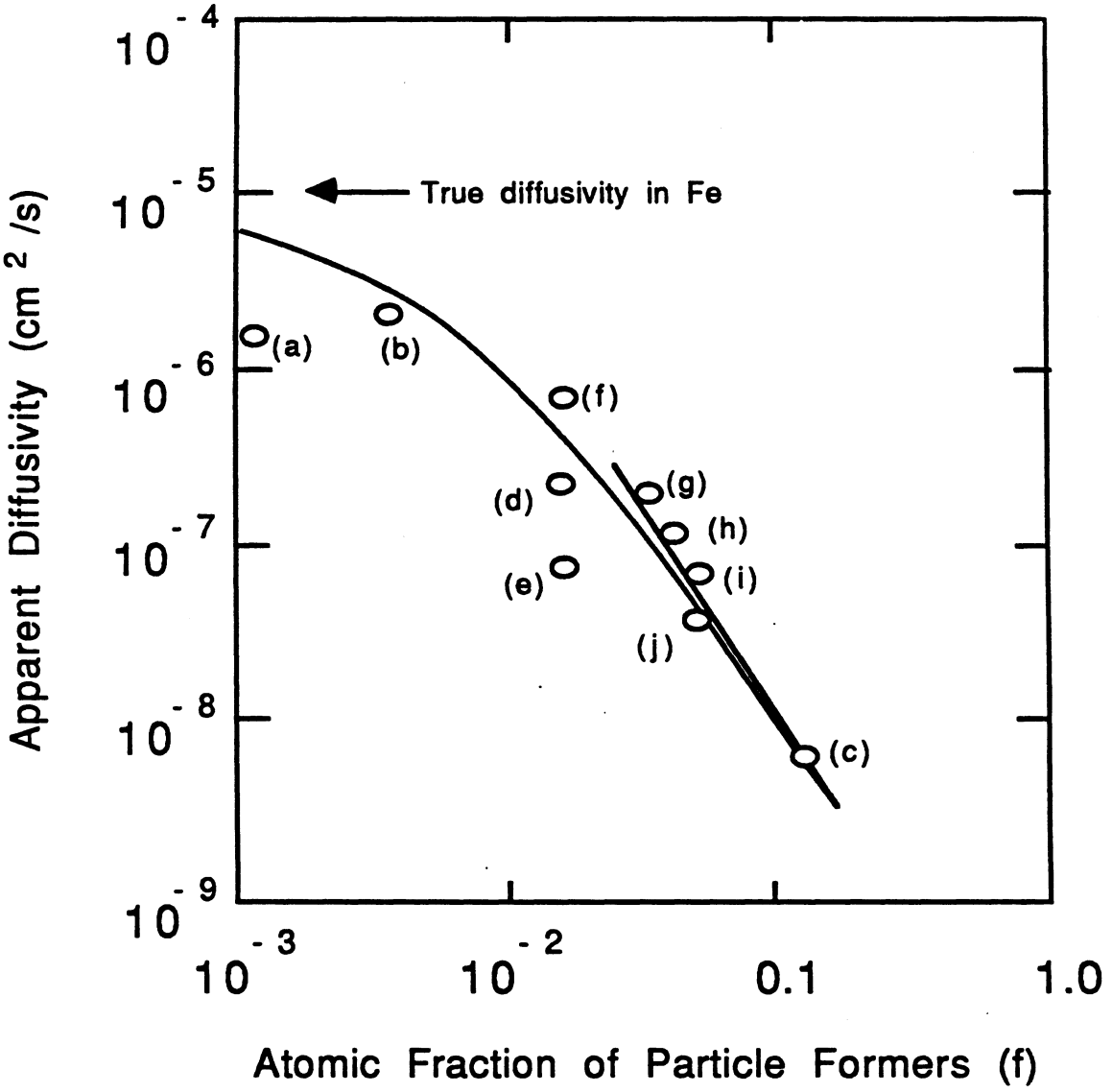

(a)	Fe-5.6% Cr	(f)	Ni-Cr-Mo
(b)	Fe-1.5% Mn	(g)	4340
(c)	Fe-0.73% C	(h)	HP-9Ni-4Co
(d)	Fe-1.1%Mn	(i)	D6aC
(e)	Fe-1.1%Mn	(j)	H-11

Figure 16.2-25. The apparent hydrogen diffusivity of various alloys as a function of the fraction of precipitate particles [93].

The effects of various elements on hydrogen embrittlement have also been studied in great detail. In general, elements such as carbon, phosphorus, sulfur, manganese, and chromium increase the susceptibility of low-alloy steels to hydrogen embrittlement. For stainless steels (high alloys), large amounts of elements such as chromium, nickel, and molybdenum are needed for manufacturing. The atom fractions of these elements in stainless steels are large enough to change the crystal structure, microstructure, and the heat treatment requirements. Since hydrogen embrittlement is sensitive to the microstructure, stainless steels with large atom fractions of Cr, Ni, and Mo, such as 15Cr-25Ni, also show almost no loss in ductility while 304 L stainless steels are the most susceptible to loss of tensile ductility when exposed to hydrogen environments [84].

The susceptibility of stainless steels to hydrogen embrittlement is also directly related to its strength. Stainless steels show extremely low resistance to hydrogen embrittlement with increasing yield strength as shown in Figure 16.2-26 for AISI 4340 steel in aqueous and gaseous hydrogen [94]. Data in Figure 16.2-26 indicate that the threshold stress intensity for crack growth generally decreases with increasing yield strength. The reason for this stress behavior is not entirely clear but it has been related to a change in hydrogen-assisted failure modes, with blistering becoming the dominant failure mechanism for low-strength steels.

Ferritic steels show an excellent resistance to hydrogen embrittlement because of their enhanced ductility and lower strength characteristics [28]. By examining a wide range of ferritic alloys that had undergone different heat treatments, Bond *et al.* [28] concluded that ferritic steels can be embrittled only after severe and extensive hydrogen charging from aqueous solutions. Furthermore, they concluded that cracking is intensified by welding, high-temperature heat treatment, and cold working. The chemical composition of the alloys was found to be less important under conditions of hydrogen charging.

The effect of temperature on hydrogen embrittlement has been investigated in detail. Hydrogen embrittlement has been observed in ferrous alloys over a wide range of temperatures, -100 to $+700\,^{\circ}\mathrm{C}$. However, the most severe embrittlement in steels occurs around room temperature [96 - 99]. The temperature dependence of the tensile strength of a high-strength steel is shown in Figure 16.2-27. At very low ($-100\,^{\circ}\mathrm{C}$) or very high ($700\,^{\circ}\mathrm{C}$) temperatures, the tensile strength of a hydrogen-charged steel approaches the values of a hydrogen-free sample [95]. This temperature dependence can be explained by noting that at high temperatures, thermal agitation may cause de-trapping of a hydrogen atom which will then diffuse rapidly through the matrix. The combination of these two effects, a higher de-trapping rate and a higher mobility, results in a low hydrogen concentration at high temperatures. At very low temperatures, on the other hand, the

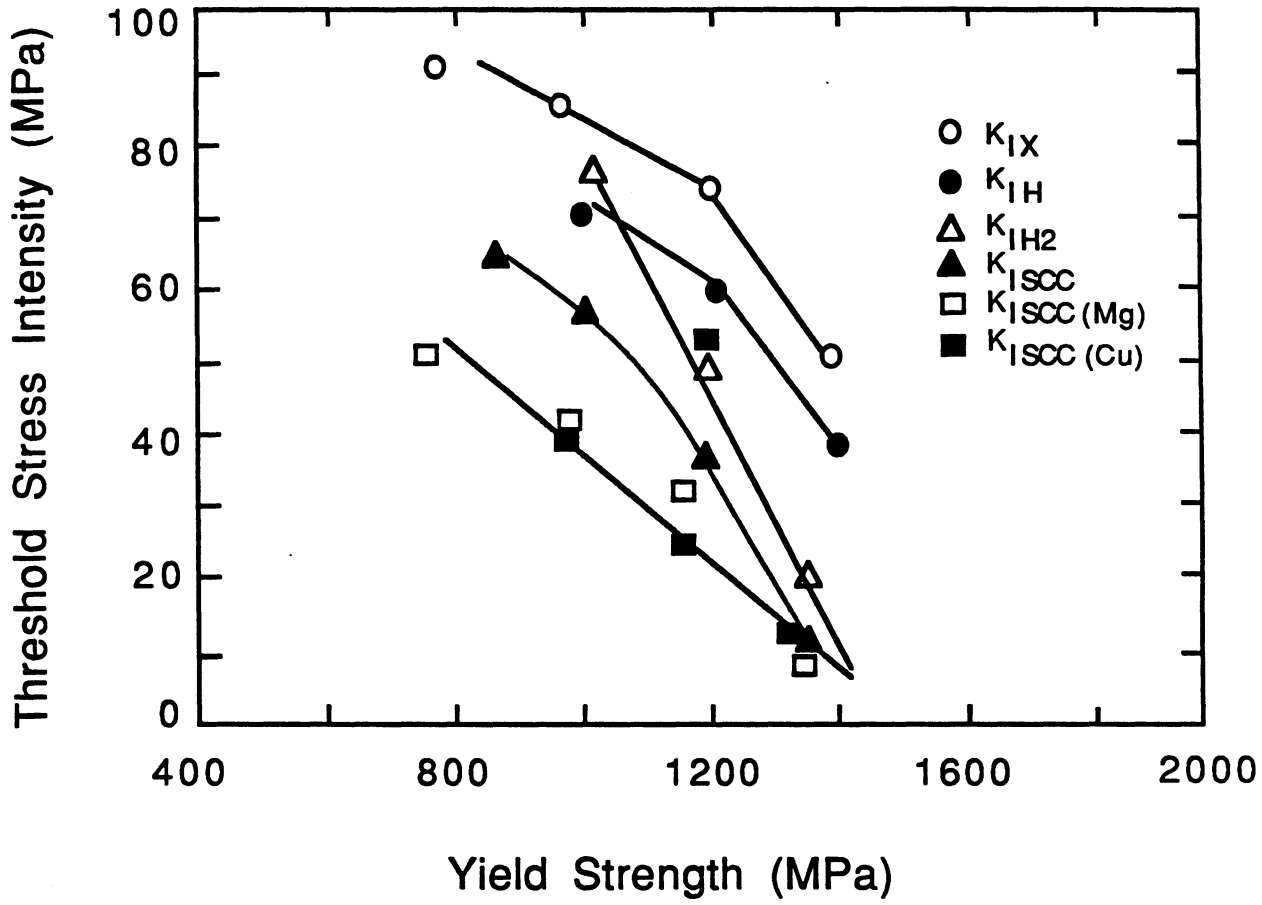

Figure 16.2-26. Effect of yield strength on some threshold stress intensity parameters for crack growth in a commercial AISI 4340 plate [94]. Here, K_{IX} is the threshold stress intensity measured in air, K_{IH} and K_{IH2} are for tests in gaseous hydrogen atmosphere, K_{ISCC}, K_{ISCC} (Mg), and K_{ISCC} (Cu) are for tests in aqueous solutions which are contact free, or are in contact with magnesium or copper, respectively.

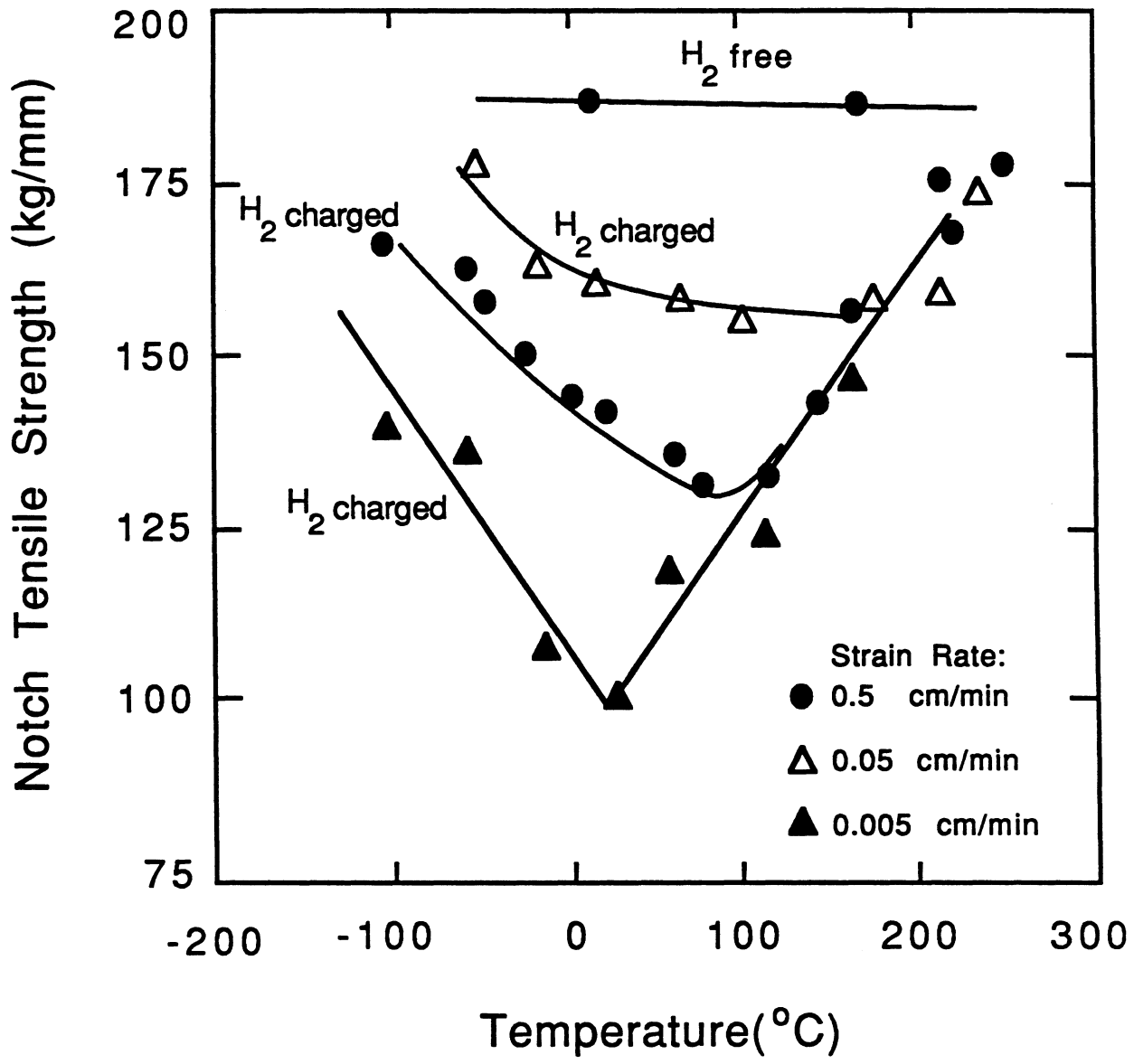

Figure 16.2-27. Tensile strength of a high-strength steel as a function of testing temperature for three strain rates [95].

diffusivity of hydrogen atoms is reduced to such a small value that trap sites would not be filled.

Figure 16.2-27 also shows that hydrogen embrittlement is highly sensitive to the strain rate. At a very high strain rate, the cracking proceeds without the assistance of hydrogen. The hydrogen mobility is not sufficient to maintain a hydrogen atom cloud around the moving dislocations. At a low strain rate, crack propagation is slow enough to keep the hydrogen concentration around the moving dislocations at levels that influence cracking. Cracking that is influenced by the presence of hydrogen falls into the category of stress-corrosion cracking (SCC). The tendency of an alloy to undergo SCC decreases with increasing temperature and drops significantly above 70 °C. Except in corrosion reactions involving hydrofluoric acid or hydrogen sulfide, SCC is usually not a problem with steels having a yield strength below 1,000 MPa [100].

16.2.5.2. Hydrogen-embrittlement prevention

The main cause of hydrogen embrittlement is the penetration of hydrogen into a metal or alloy. Techniques for in-service hydrogen-embrittlement prevention generally focus on either eliminating the source of hydrogen or minimizing stresses to below the threshold values necessary to cause cracks. For nuclear components, however, the hydrogen source from (n,p) reactions can never be totally eliminated. Nevertheless, hydrogen embrittlement may be mitigated or prevented by application of one or more of the following preventive measures.

Reducing corrosion rates. Corrosion of metals or alloys in aqueous solutions is always accompanied by the evolution of hydrogen at the surface of the metal. Corrosion-prevention measures are discussed in detail in Section 16.2.1.2. These include changes in the corrosive medium such as removing oxides or adding carefully selected inhibitors. Table 16.2-IV includes a reference list of corrosion inhibitors.

Baking. Hydrogen embrittlement is an almost fully reversible process, especially in low-carbon steels, if no hydrogen damage has yet occurred. If the hydrogen is removed, the mechanical properties of the treated material are only slightly different from those of hydrogen-free steels. Although a common way of removing hydrogen is by baking at relatively low temperatures (200 to 300 °F), high service temperatures will also ensure minimal hydrogen entrapment inside the matrix. Trapping of hydrogen atoms decreases

as the service temperature is increased above 200 °C. High-temperature hydrogen attack (*i.e.*, decarburization due to volatile CH_4 formation) is a major concern only for high-carbon or low-alloy steels.

Alloy selection. Hydrogen embrittlement strongly depends on the strength of the alloy and high-strength steels are the alloys which are most susceptible to hydrogen embrittlement. Low-strength alloys ($\sigma_Y < 1000\,\text{MPa}$) are the least susceptible to hydrogen embrittlement. Furthermore, alloying elements such as nickel and molybdenum reduce the susceptibility to hydrogen embrittlement [3].

Reduction of SCC by deaeration of boiler water. Experiments with the addition of hydrogen to water in BWRs has shown that SCC can be reduced markedly (Section 16.2.1.3).

In summary, aeration (the presence of dissolved oxygen in a liquid medium) may have profound influence on the corrosion rate of metals. Some metals and alloys are more rapidly attacked in the presence of oxygen, whereas others may show better corrosion resistance. For example, deaeration of boiler water results in a marked decrease in the corrosion of steels and cast irons. The addition of hydrogen results in a deaeration or reduction of oxygen content of the water, leading to a decrease in corrosion rate [13, 23-26]. These experiments demonstrate the different effects between nascent (monatomic, adsorbed, and diffusible) hydrogen and molecular (H_2) hydrogen. While nascent hydrogen increases SCC, molecular hydrogen decreases SCC because of recombination with dissolved oxygen.

Petrochemical plants expose metals to high temperatures and high hydrogen pressures (hydrogenation processes). The dissociation of molecular hydrogen under conditions of high pressure and high temperature is a major source of diffusible hydrogen. The reaction of hydrogen with carbon has been identified as the main cause of hydrogen embrittlement in hydrogenation processes. The petrochemical industry has adopted a practical solution to this problem by using low-alloy steels. These steels contain carbon stabilizers such as chromium, molybdenum, tungsten, vanadium, titanium, and niobium. In addition to altering the microstructure of the alloy, these alloying elements also reduce the reactivity of carbon with absorbed hydrogen. Experience in the petrochemical industry has resulted in the development of "Nelson curves" [101] which prescribe the acceptable limits of temperature and hydrogen partial pressure for common low-alloy steels. An example of these curves is shown in Figure 16.2-28. It can be seen that a higher chromium content

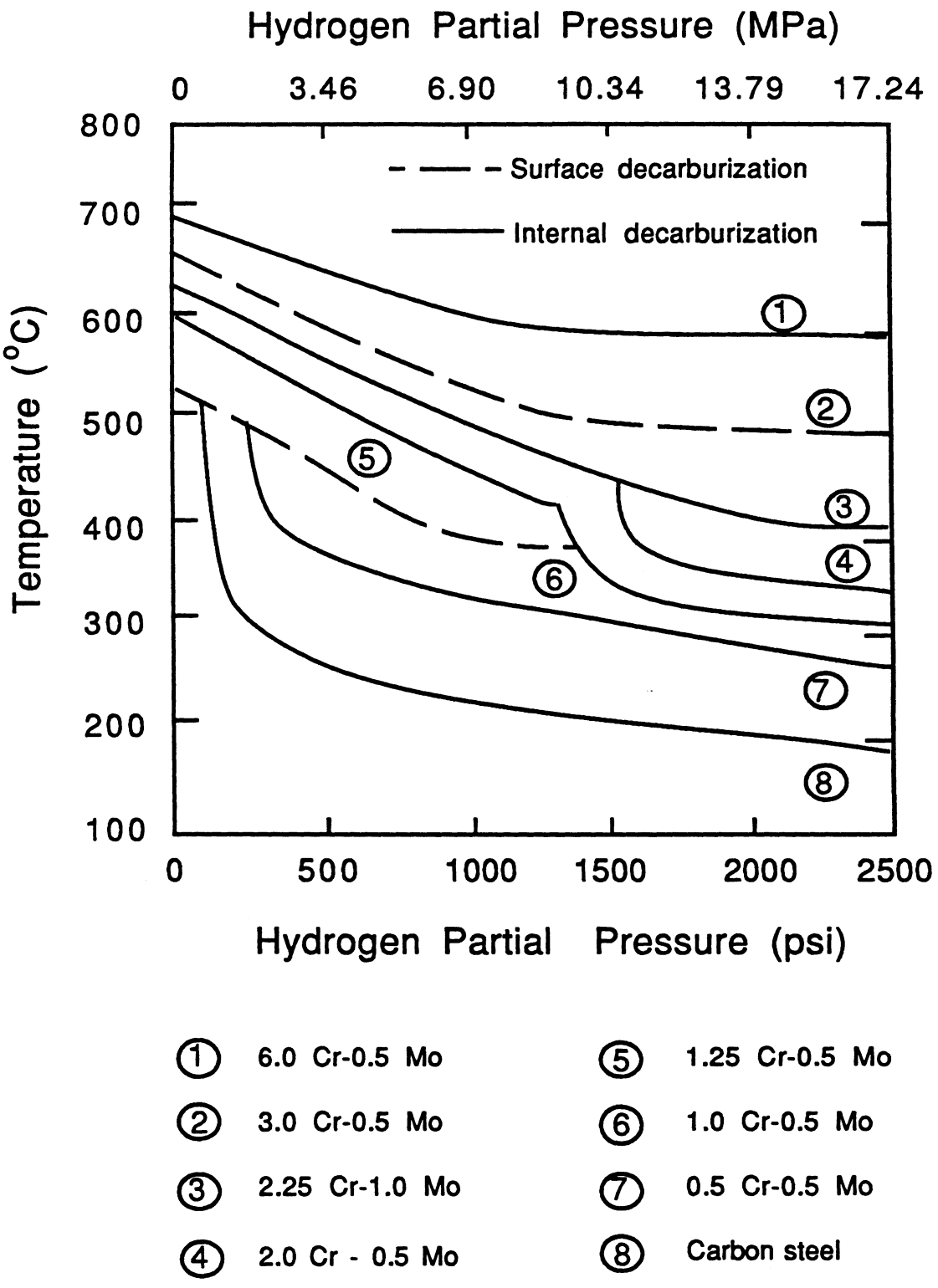

Figure 16.2-28. Operating limits (Nelson curves) for steels in hydrogen service [100].

allows higher temperatures and higher hydrogen partial pressures. The worst case is that of regular carbon steel.

16.2.5.3. Discussion

Hydrogen embrittlement is an important phenomena caused mainly by the trapping of absorbed hydrogen in metals under applied stresses. The main factor influencing hydrogen embrittlement is the hydrogen content which depends strongly on the temperature, microstructure, and strength of the alloy. Hydrogen content can be reduced by minimizing the source of nascent hydrogen (mostly due to corrosion) and by operating at high temperatures ($> 200\,^{\circ}\mathrm{C}$), provided that a low-carbon steel is used. High concentrations of chromium, nickel, or molybdenum ($> 10\,\mathrm{wt}\%$) increase the resistance of ferrous alloys to hydrogen damage. Microstructural features such as a fine-grained and annealed alloy with minimum cold work further reduce susceptibility to hydrogen embrittlement. Because of the lower strength and higher ductility of ferritic steels, these alloys are generally less susceptible to hydrogen embrittlement than austenitic steels.

The low-activation, ferritic steel 9-C is chosen as the reference structural material for the TITAN-II FPC (Section 16.2.4). The 9-C alloy contains very small amounts of carbon ($\leq 0.097\,\mathrm{wt}.\%$), but has a high concentration of carbon-stabilizing elements ($\geq 11\,\mathrm{wt}.\%$ Cr, $6\,\mathrm{wt}.\%$ Mn, $0.28\,\mathrm{wt}.\%$ V, and $0.89\,\mathrm{wt}.\%$ W). Furthermore, the addition of nitrate salts to the aqueous solution reduces the corrosion rate of ferrous alloys (Section 16.2.1.2), resulting in a reduction in the production of hydrogen atoms on the surfaces, thus reducing the nascent hydrogen content.

The production of hydrogen by nuclear reactions and by plasma-driven permeation through the first wall of a fusion device increases the hydrogen content inside the alloy matrix which may lead to unacceptable hydrogen embrittlement of the structure for operation at or near room temperature (the highest susceptibility of high-strength alloys to hydrogen embrittlement is at or near room temperature [100]). But the TITAN-II structural material operates at high temperatures ($> 400\,^{\circ}\mathrm{C}$), minimizing the effective trapping of hydrogen inside the matrix. Experiments show that above $\sim 200\,^{\circ}\mathrm{C}$, hydrogen embrittlement of ferrous alloys is reduced markedly [3]. Furthermore, the Nelson curves indicate that 2.0 Cr-0.5 Mo steel can operate at $400\,^{\circ}\mathrm{C}$ with a hydrogen partial pressure of 17 MPa without internal decarburization and hydrogen embrittlement (Figure 16.2-28).

Based on the above discussion, the ferritic alloy 9-C is expected to exhibit a high resistance to hydrogen embrittlement. The number of factors influencing hydrogen embrittlement are numerous and their interdependence is a complex function of the specific

microstructure and operating conditions of an alloy. Therefore, experimental data are needed in order to perform a complete evaluation of hydrogen embrittlement of the 9-C alloy under TITAN-II operating conditions.

16.2.6. Neutron-Multiplier Material

Beryllium is chosen as the neutron-multiplier material for the TITAN-II design mainly because of low activation. Concerns associated with beryllium are toxicity, resource limitation, and radiation damage. In this section, properties of beryllium are presented (Section 16.2.6.1) and the available data on corrosion of beryllium by the aqueous solution is reviewed (Section 16.2.6.2). Section 16.2.6.3 discusses the irradiation behavior of beryllium.

16.2.6.1. Properties

Selected properties of beryllium are given in Table 16.2-XIII. Mechanical properties of beryllium at elevated temperatures depend on the microstructure and composition (purity). Ultimate tensile and yield strengths of typical commercial beryllium (low purity) are given in Table 16.2-XIV. The average grain size of the tested beryllium was 16 μm with the principle impurities being: 200 appm oxygen, 620 appm argon, 1380 appm iron, 500 appm silicon, and 220 appm titanium.

16.2.6.2. Beryllium corrosion

The two areas of concern regarding beryllium in a fusion environment are swelling and corrosion. Beryllium that is clean and free of surface impurities (in particular carbonates and sulfates) has exceedingly good resistance to attack in low-temperature, high-purity water [102], with typical corrosion rates of less than 1 mil/y [103]. In a slightly acidic demineralized water of a nuclear test reactor, beryllium has performed without problems for over 10 years [104,105].

Beryllium exposed to chloride and sulfate-contaminated aqueous solutions is susceptible to attack. Development of corrosion-protective coatings for beryllium has been extensive [104]. Extremely thin (100 Å) chromate coatings produced by simple dip treatments have shown to hold up under 5% salt spray tests for a period of 120 h [106]. With anodized coatings, no corrosion was detected after 2000-h exposure in ASTM salt-spray

Table 16.2-XIII.

SELECTED PROPERTIES OF BERYLLIUM[(a)] [102]

Atomic weight	9.01
Density (g/cm^3)	1.85
Crystal structure	
T<1254°C	h.c.p.
T>1254°C	b.c.c.
Melting temperature (°C)	1283
Boiling temperature (°C)	2484
Heat of fusion (J/g)	1083
Heat of vaporization (J/g)	24,790
Heat capacity (J/g-°C)	
500 °C	2.25
1000 °C	2.92
1500 °C	3.59
Coefficient of thermal expansion (1/ °C)	
25– 100 °C	11.6×10^{-6}
25– 500 °C	15.9×10^{-6}
25–1000 °C	18.4×10^{-6}
Thermal conductivity (W/m-K)	
50 °C	150
300 °C	125
600 °C	90
Electrical resistivity ($\mu\Omega$ cm)	
50 °C	5
300 °C	12
600 °C	23
Bulk modulus (GPa)	115.8
Shear modulus (GPa)	157.7
Young's modulus (GPa)	278.5
Poisson ratio	0.2
Fracture mode	cleavage
Ductility	poor

(a) Properties are at room temperature except as indicated.

Table 16.2-XIV.

ULTIMATE TENSILE STRENGTH AND 0.2% YIELD STRENGTH OF A TYPICAL BERYLLIUM SHEET [102]

Temperature (°C)	Yield Strength (MPa)	Ultimate Tensile Strength (MPa)
300	180	360
500	140	260
700	100	170
900	80	120
1073	10	25

tests [104]. Uniform and adherent anodized coatings on beryllium are produced either by solutions of 50% HNO_3 with a current density of 0.20 A/ft^2 for 5 minutes, or by solutions of 7.5% NaOH with a current density of 10 A/ft^2 for 20 minutes. It is conceivable to develop an in-situ anodizing mechanism to coat beryllium in an aqueous self-cooled blanket. In particular, the TITAN-II blanket coolant contains both NO_3 and OH ions. Extensive research into this area will be required to establish the feasibility of in-situ anodizing methods.

16.2.6.3. Swelling

Irradiation-induced swelling is a major concern associated with beryllium in a fusion environment. Swelling of beryllium under neutron irradiation is mostly caused by helium-gas generation from (n,α) reactions. Helium atoms are insoluble in metals and consequently they will rapidly diffuse through the metal until they become immobilized at trap sites such as thermodynamically and irradiation-produced dislocations, cavities, and grain boundaries. This phenomena is responsible for the nucleation and growth of bubbles. Bubbles can also migrate through the matrix or along grain boundaries and coalesce to form bigger bubbles (increased swelling). The temperature has to be high enough to allow bubble migration and coalescence.

The threshold temperature below which swelling of beryllium is insignificant was determined in early post-irradiation experiments [107 - 110]. For fluences resulting in a few appm of helium-atom concentration in beryllium, the threshold temperature is around 700 °C while for fluences creating more than 50 appm of helium, swelling threshold temperature drops to about 500 °C. Beryllium located behind the first wall of a fusion device will have a helium generation rate of about 10,000 helium appm per 1 MW y/m^2. Because of these high helium-generation rates, suppression of beryllium swelling through operation at low temperatures is not feasible in a fusion blanket.

High-temperature (1000 °C), post-irradiation anneal experiments showed a maximum swelling of 30%. This maximum in swelling was attributed to interconnecting bubbles which resulted in a release of trapped helium from the bulk. The minimum swelling necessary to produce an interconnecting network of helium bubbles for gas venting was theoretically determined to be 5% to 10% [111]. Thus, beryllium exposed to high levels of fast-neutron irradiation will swell a minimum of about 10% and a maximum of 30% at high temperatures (> 750 °C).

Phenomenological swelling equation

Because it is believed that swelling has its microstructural origin in helium behavior, a swelling equation based on the following gas-behavior assumptions has been developed: (1) Van der Waal's equation of state is used, (2) all retained gas is trapped in bubbles, (3) all bubbles are of the same size, (4) bubbles are in mechanical equilibrium with the solid, and (5) irradiation-induced re-solution is neglected.

The Van der Waal's equation of state, commonly used to describe the thermodynamic state of fission gas bubbles, is:

$$p\left(\frac{1}{\rho_g} - B\right) = kT\,, \tag{16.2-47}$$

where p is the pressure of the gas of molecular density ρ_g at temperature T. The Van der Waal parameter, B, can be regarded as an expression for the volume occupied by a single gas atom. Using the mechanical-force balance on a bubble, $p = 2\gamma/R$ yields:

$$\frac{1}{\rho_g} = B + \frac{kT}{2\gamma}R\,, \tag{16.2-48}$$

where γ is the surface tension of a bubble with a radius R.

Assuming that all retained helium atoms are trapped inside bubbles of equal size, the fractional increase in volume caused by the bubbles is:

$$\frac{\Delta V}{V} = \frac{4\pi}{3} R^3 N . \tag{16.2-49}$$

The bubble number density, N, is related to the number of gas atoms per bubble, m, and the helium generation rate, $\dot{G}_{He}$:

$$m N = f_R \dot{G}_{He} t , \tag{16.2-50}$$

where f_R is the fraction of helium atoms retained in the bulk of the material and t is the time of irradiation. Using Equation 16.2-48, the number of gas atoms contained inside a bubble of radius R is:

$$m = \frac{4\pi}{3} R^3 \rho_g = \frac{4\pi}{3} \frac{R^3}{B + (kT/2\gamma)R} . \tag{16.2-51}$$

Combining Equations 16.2-49 through 16.2-51 and assuming bubbles have radii greater than 1000 Å (ignoring B) results in:

$$\frac{\Delta V}{V} = \left(\frac{3}{4\pi}\right)^{1/2} \left[\left(\frac{kT}{2\gamma}\right)\left(\frac{f_R \dot{G}_{He} t}{N^{1/3}}\right)\right]^{3/2} . \tag{16.2-52}$$

Note that the swelling rate scales as $t^{1.5}$, which is commonly found experimentally. To use Equation 16.2-52, it is necessary to know the surface tension of bubbles in beryllium, the fraction of retained helium atoms, and the bubble number density.

Recently, Beeston [112,113] measured beryllium swelling as a function of temperature and helium content. The helium content was about 30,000 appm. Beryllium was irradiated in ETR and ATR test reactors up to 3.5×10^{22} n/cm^2 by fast neutrons ($E > 0.1$ MeV). The number densities of helium bubbles were measured at annealing temperatures between 400 and 600 °C [113]. An empirical equation, given by Beeston, for the number density as a function of temperature is:

$$N = 1.4 \times 10^{14} \exp\left(\frac{0.41}{kT}\right) , \tag{16.2-53}$$

where N is given in bubbles per cm^3, k is Boltzmann constant ($k = 8.618 \times 10^{-5}$ eV/K), and T is the temperature in Kelvin. Since the effects of high-fluence 14-MeV neutrons are not known at the present time, this model should be used with caution.

No measurements for the fraction of retained helium atoms are reported. Therefore, for the purpose of using Equation 16.2-52, it is conservatively assumed that all helium

atoms produced during irradiation are trapped ($f_R = 1$). Beryllium surface-energy measurements have been performed and the values quoted range from 1 to $2\,J/m^2$ [114 - 117]. In calibrating the swelling Equation 16.2-52 to Beeston's data, a surface tension value of $1.6\,J/m^2$ leads to the best agreement between the model and the data. Table 16.2-XV shows a comparison of the experimental data with predictions of Equation 16.2-52. For the temperature range between 300 and 500 °C, good agreement between the model and measured swelling data is apparent.

To estimate the swelling of the TITAN-II beryllium rods, it is assumed that high density beryllium, which retains most of the generated helium, is used. Table 16.2-XVI shows the estimated beryllium swelling after one full-power year (FPY) of operation. The beryllium was assumed to have an average temperature of 500 °C. It can be seen that with conservative assumptions, the maximum swelling of beryllium should not be higher than $\sim 15\%$ at 0.5 cm behind the first wall.

Swelling of porous beryllium

The estimated swelling values of Table 16.2-XVI were calculated assuming no loss of helium atoms from the matrix. Loss of helium through open pores and helium trapped in closed pores affects the rate of swelling. A realistic model of beryllium swelling has to account for helium released through open pores and for the fraction that is retained in closed pores.

First, the amount of helium trapped in closed pores needs to be approximated. At high temperatures (> 250 °C), the helium bubbles will be in mechanical equilibrium ($p = 2\gamma/R$). For an average-sized closed pore of $R = 2.5\,\mu m$, the amount of helium trapped is

$$n = \frac{8\,\gamma\,\pi\,R^2}{3\,k\,T} \simeq 1.96 \times 10^9 \text{ (atom per pore)}. \qquad (16.2\text{-}54)$$

The total helium produced during 1 FPY of operation in beryllium located just behind the first wall of the TITAN-II reactor is about 6.6×10^{21} He/cm^3. Starting with a beryllium matrix having a density of about 70% theoretical density (70% TD or 30% open porosity), and assuming a 50% pore closure by self welding, the fraction of helium trapped inside closed pores after 1 FPY is estimated to be

$$\frac{1.96 \times 10^9(\text{He/pore})}{8.2 \times 10^{-12}(\text{cm}^3/\text{pore})} \times (0.3) \times (0.5) = 3.1 \times 10^{19}(\text{He/cm}^3). \qquad (16.2\text{-}55)$$

Table 16.2-XV.

EXPERIMENTAL[a] AND ESTIMATED[b] SWELLING VALUES OF BERYLLIUM

	$\Delta V/V$ (%)	
Temperature (°C)	Experiments[a]	Estimated[b]
200	1.2	0.36
300	1.5	1.29
400	3.	3.17
500	6.	6.69

(a) Specimen contained about 30,000 appm helium (3.7×10^{21} He/cm^3) [112,113].

(b) Estimated using Equation 16.2-52.

Table 16.2-XVI.

SWELLING OF SOLID BERYLLIUM IN THE TITAN-II REACTOR[a]

Distance from First Wall (cm)	Total Helium (appm)	$\Delta V/V$ (%)
0.5	53,400	14.5
4.9	34,000	7.4
9.5	20,300	3.4
14.5	11,900	1.5

(a) After 1 FPY of operation at 18 MW/m^2 neutron wall loading.

This rough estimate shows that only about 0.5% of the total generated helium is trapped inside closed pores. Only at very low temperatures can the amount of helium trapped inside closed pores be a fairly large fraction of the total amount produced.

Estimating the amount of helium that reaches open surfaces through interconnected open pores is best determined empirically. However, because of the lack of experimental data, only a rough estimate can be made. Diffusion of helium through beryllium can be estimated using self-diffusion coefficients given by [118]:

$$D_{\perp} = 0.52 \exp\left(\frac{-1.63}{kT}\right) , \qquad (16.2\text{-}56)$$

$$D_{\parallel} = 0.62 \exp\left(\frac{-1.71}{kT}\right) , \qquad (16.2\text{-}57)$$

where $D_{\perp}$ and $D_{\parallel}$ are, respectively, the diffusion coefficients perpendicular and parallel to the C-axis (in units of cm^2/s) and kT is in units of eV. Assuming an average diffusion path to open pores of $10\,\mu m$ and an average temperature of 500 °C, Equations 16.2-56 and 16.2-57 predict that it would take a helium atom from 1 to 3 days to reach the pore, depending on the crystal orientation. Thus, at elevated temperatures, a substantial fraction of untrapped helium atoms can reach open pores within a short time. If 30% of all generated helium atoms escape to open pores, about 1.9×10^{21} He/cm^3 will be vented resulting in $f_R \simeq 0.7$. Based on this estimate for f_R, the maximum beryllium swelling at 0.5 cm behind the first wall of TITAN-II is about 8.5%. The above calculations assume that the pores in the beryllium rod remain open and do not sinter during operation; sintering must be minimized to avoid pore closure and excessive swelling.

A smear density of 70% TD can be achieved using sphere-packed beryllium. The maximum operating temperature must be kept below 660 °C to prevent sintering of the spheres. Beeston [119] has conducted experimental investigations of grain growth of beryllium which indicate open porosity below 661 °C. The thermal conductivity of 70% TD beryllium at 600 °C is about 44 W/m-°C [120].

Strength

Most metals undergo hardening when exposed to neutron irradiation. Similarly, beryllium is expected to experience an increase in yield strength with irradiation [121]. Miller *et al.* [122] analyzed the effects of irradiation on the strength and fracture toughness of beryllium. Figure 16.2-29 shows the effects of temperature and irradiation on the strength of beryllium at a fluence of 1.2×10^{22} n/cm^2. Irradiation increases the strength

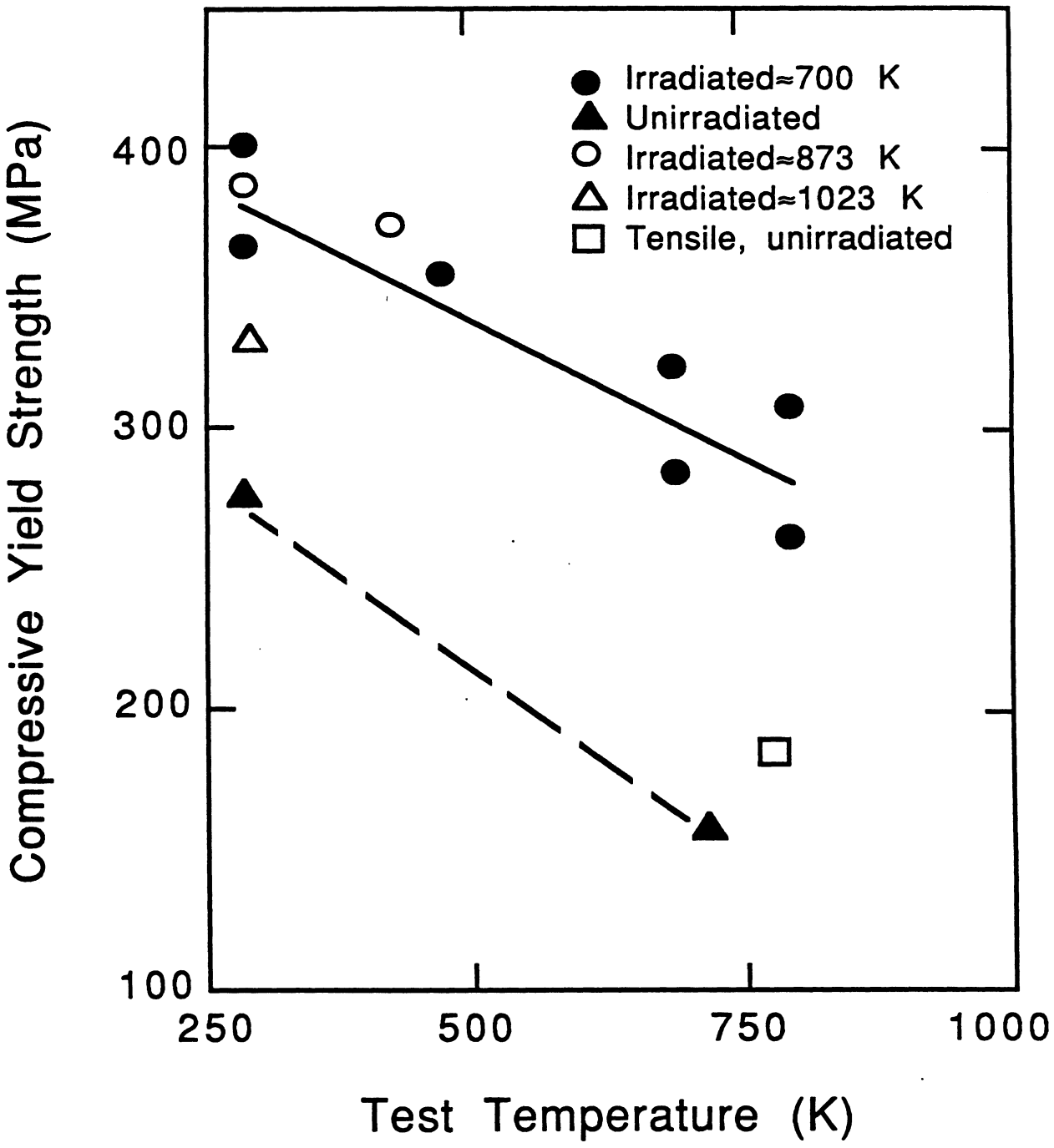

Figure 16.2-29. Compressive yield strength of beryllium as a function of test temperature under irradiation with a fluence of 1.2×10^{22} n/cm^2 [122].

of beryllium by a factor of ~ 2 at temperatures between 300 and 600 °C. Although the data base of irradiated beryllium is sparse, the irradiated strength measurements indicate adequate retention of the compressive strength. Irradiation experiments to measure the ductility of beryllium are needed to understand and model lifetime-limiting effects.

16.2.6.4. Discussion

Corrosion of beryllium in aqueous solutions is a function of the cleanliness of the beryllium surface and of solution impurities. Beryllium surfaces should be free of carbonates and sulfates and the water should have minimum chlorate and sulfate impurities to assure minimum corrosion rates. Coatings to protect beryllium against attack have been developed and their effectiveness has been demonstrated in a neutron-free environment.

Swelling levels of above $\sim 10\%$ will most likely result in a network of interlinking helium bubbles, thus promoting helium release. This means that swelling will stop temporarily until large enough temperature gradients cause sintering of open channels. The sintering temperature for beryllium has been estimated to be around 660 °C. The ongoing process of closing and opening of porosity will ultimately lead to an equilibrium helium-venting rate with an associated maximum swelling value. Realistic prediction of this process is currently not feasible because of the lack of experimental data. A phenomenological swelling equation for beryllium is developed which predicts a maximum swelling value between 9% and 15% depending on the amount of retained helium atoms. A swelling value of 10% is taken as the basis for design calculations. Swelling may be accommodated, to a degree, by using beryllium with low TD ($\sim 70\%$). This density can easily be achieved by using sphere-packed beryllium. The maximum operating temperature must be kept below 600 °C to prevent sintering of the spheres.

Two methods for accommodating the high rate of swelling in beryllium are available: (1) using a very fine grain beryllium operating at temperatures above 750 °C to ensure interlinkage of bubbles to vent the helium gas into the plenum of the cladding tube; and (2) using low-TD beryllium (sphere packed to a TD of $\sim 70\%$) to accumulate helium inside the porosity. The latter approach, however, results in a lower neutron multiplication and a reduction of thermal conductivity.

Irradiation data on the strength of beryllium are sparse. Irradiation hardening does occur at temperatures above 300 °C. McCarville *et al.* [123] predict that thermal creep may help extend the lifetime by relieving stresses caused by differential swelling, with irradiation-creep effects being negligible.

16.2.7. Discussion

In the TITAN-II design, tritium breeding is accomplished in a lithium salt which is dissolved in the primary-water coolant. Issues of corrosion and radiolysis, therefore, greatly impact the choice of the dissolved lithium salt and the structural material.

Two candidate lithium salts, lithium hydroxide (LiOH) and lithium nitrate ($LiNO_3$), are considered because they are highly soluble in water. The $LiNO_3$ salt was selected as the reference salt material for two main reasons. First, LiOH is more corrosive than $LiNO_3$ (Section 16.2.1). Recently, electrochemical corrosion tests were performed for aqueous LiOH and $LiNO_3$ solutions in contact with AISI 316L stainless steels [37]. It was found that stainless steels, particularly low-carbon steels, exhibit better corrosion resistance in $LiNO_3$ solution than in LiOH. Second, from the point of view of radiolysis, $LiNO_3$ solutions are also preferable. Radiolytic decomposition of water results in the formation of free radicals that will ultimately form highly corrosive hydrogen peroxide and OH ions. In an $LiNO_3$ solution, nitrate ions (NO_3) act as scavengers and reduce the probability of survival of highly reactive radicals in the water during exposure to radiation.

The most drastic effect of adding $LiNO_3$ to the coolant water is the elevation of the boiling point of the solution. This implies that the thermal-hydraulic design of such an aqueous salt blanket will be different from that of a pure-water-cooled design. A lower coolant pressure or a higher operating temperature can therefore be chosen.

The low-activation ferritic alloy, 9-C, was chosen from among other reduced-activation ferritics because of its good strength and elongation behavior after irradiation. The high chromium content (11 wt.%) of this alloy should provide good resistance to corrosion in an aqueous solution. The low-carbon content (0.09 wt.%) reduces the risk of hydrogen embrittlement. Although no data on the ductile-to-brittle transition temperature (DBTT) is available, it is believed that the high manganese content (6.5 wt.%) of 9-C will prevent the formation of delta-ferrite phases which are primarily responsible for increases of DBTT. The data base for corrosion of ferritics in $LiNO_3$ solutions is very limited. Indications are, however, that a high-concentration $LiNO_3$ solution does not exhibit unacceptable corrosion problems.

Stress-corrosion cracking (SCC) is a major concern in the nuclear industry. Most recent experiences with SCC in a nuclear environment clearly show that SCC can be suppressed by reducing the oxygen content through the addition of hydrogen to the coolant. The production of tritium in an aqueous $LiNO_3$ solution is seen as an SCC-controlling mechanism. The proper choice of structural material can further reduce the

probability of SCC. In particular, a high chromium content coupled with a low carbon content (as in the ferritic alloy, 9-C) are shown to reduce SCC.

Another form of attack on structural material in an aqueous environment is hydrogen embrittlement. The main factors influencing hydrogen embrittlement are the hydrogen content and the temperature of the structural alloy. Reducing the amount of atomic hydrogen available for solution in the structure and operating at high temperatures are the most effective means of reducing hydrogen attack. Atomic hydrogen is produced on metal surfaces during corrosion processes. Thus, minimizing corrosion also reduces hydrogen embrittlement of the structure. The production of tritium in the coolant does not necessarily result in an increased hydrogen attack because of rapid recombination to form molecular hydrogen or water molecules. In fact, the Nelson curves, used by the petrochemical industry as guidelines, show that chromium steels can operate at 400 °C with a hydrogen partial pressure of 17 MPa without experiencing hydrogen embrittlement [100].

Radiolytic decomposition of aqueous solutions exposed to a radiation environment is always cause for concern. Experimental data indicate that light-particle radiation (e, γ, and X rays) of concentrated $LiNO_3$ solutions results in a decrease of decomposition products compared with regular water. Heavy-particle radiation (n, p, α, and T) on concentrated $LiNO_3$ solutions also shows a decrease in the formation of radiolytic products, excepting oxygen. However, the production of tritium effectively reduces the oxygen content of the coolant by forming water molecules. Furthermore, the elevated operating temperature of the coolant is shown to be effective in reducing formation of decomposition products in non-boiling nuclear systems. More experimental data are required so that the radiolytic behavior of concentrated salt solutions can be predicated with a higher degree of confidence.

The TITAN-II design requires a neutron multiplier to achieve an adequate tritium-breeding ratio. Beryllium is the primary neutron multiplier for the TITAN-II design. Investigation of the swelling behavior of beryllium shows the necessity of using either low-density, sphere-packed or high-density, fine-grained beryllium. Depending on the type of beryllium chosen, different operating conditions must be satisfied to ensure minimum swelling and retention of structural integrity. Beryllium corrosion by an aqueous solution was also investigated. Past experience shows that minimizing carbonates, sulfates, and chlorates in solution reduces corrosion of beryllium. Coatings have also been developed and their effectiveness has been demonstrated. However, since most of the coatings were developed for radiation-free environments, research is needed to develop coatings that can withstand harsh radiation environments. For the TITAN-II design, a cladding of 9-C alloy surrounds the beryllium rods.

16.3. NEUTRONICS

Neutronics calculations for the TITAN-II design were performed with ANISN [124], a 1-D neutron and gamma-ray transport code, using a P_3S_8 approximation in cylindrical geometry. The nuclear data library, ENDF/B-V-based MATXS5 was used. The library was processed with the NJOY system at Los Alamos National Laboratory [125]. The energy group structures in this library are 30 groups for the neutron cross sections and 12 groups for the gamma-ray cross sections.

The TITAN-II design is cooled by an aqueous lithium-nitrate solution. The structural material is a low-activation ferritic-steel alloy, 9-C [2]. The TITAN-II blanket requires neutron-multiplier material to achieve an adequate tritium-breeding ratio (TBR). Beryllium is chosen as the multiplier, mainly because of its low-activation property.

This section describes the neutronics studies for the TITAN-II design. Scoping studies are reported in Section 16.3.1 and include an assessment of the blanket performance if heavy water (D_2O) is used as the coolant, and the impact of beryllium density on the blanket performance. The neutronics performance of the TITAN-II reference design is described in Section 16.3.2.

16.3.1. Scoping Studies

Neutronics scoping studies are performed with the configurational parameters based on the mechanical and thermal-hydraulic design of the TITAN-II FPC. The first wall is 12.5-mm thick and is composed of 16.7% structure, 61.8% coolant, and the balance is void (in this section, all material compositions are in volume percentages, except as otherwise noted). The blanket zone composition is 9% structure, 32% coolant, and 59% beryllium. The thickness of the blanket is a variable in the scoping studies. The blanket is followed by a metallic shield composed of 90% structure and 10% coolant. Two shield thicknesses of 0.2 and 0.25 m are considered.

A 50-mm-thick zone is located behind the shield to simulate the toroidal-field (TF) coils. The material composition of this zone is 10% structure, 10% spinel insulator ($MgAl_2O_4$), 10% coolant (pure water), and 70% copper conductor. The ohmic-heating (OH) coils of the TITAN-II design are located 0.78 m from the first wall in the scoping studies. The material compositions of the OH coils are identical to the TF coils. The space between the TF and OH coils contains pure water (the low-pressure water pool).

For the scoping studies, it is assumed that the aqueous coolant contains $LiNO_3$ salt and ordinary water (H_2O) with 1:5 molecular ratio. This aqueous $LiNO_3$ solution has

Table 16.3-I.

BERYLLIUM ZONE THICKNESSES TO ACHIEVE DIFFERENT TRITIUM-BREEDING RATIOS IN THE TITAN-II BLANKET[a]

	Tritium-Breeding Ratio					
	1.1			1.2		
^{6}Li enrichment (%)	7.42	30.	60.	7.42	30.	60.
Be zone thickness (m)	0.20	0.12	0.09	0.23	0.14	0.11
Blanket energy multiplication [b]	1.41	1.30	1.26	1.43	1.33	1.29

(*a*) For a 0.2-m-thick shield with 18 MW/m^2 neutron wall loading.

(*b*) Including all nuclear energy deposited in the first wall, Be zone, and shield.

a density of 1.07 g/cm^3 and contains 5 at.% of lithium. The blanket tritium breeding is strongly affected by ^{6}Li enrichment in the lithium salt. Three ^{6}Li enrichment cases were considered in the scoping studies: 7.42% (natural abundance), 30%, and 60%.

In the initial phase of the scoping studies, we varied the beryllium zone thickness from 0.1 to 0.3 m while keeping the shield thickness at 0.2 m. It was found that the TBR ranged from 0.76 for natural ^{6}Li enrichment (7.42%) and 0.1-m-thick beryllium zone to TBR of 1.66 for 60% ^{6}Li enrichment and 0.3-m-thick beryllium zone.

Next, for a given TBR, the thickness of the beryllium zone was estimated. Table 16.3-I presents the estimated thickness of the beryllium zone to achieve TBR of 1.1 or 1.2 for different ^{6}Li enrichment of 7.42%, 30%, and 60%. The resultant blanket-energy multiplications for these blanket systems are also given. Table 16.3-I shows that: (1) the blanket energy multiplication ranges from 1.25 to 1.43 as the beryllium zone thickness varies from 0.09 to 0.23 m; and (2) ^{6}Li enrichment can be adjusted, for example, from 7.42% to 60% ^{6}Li, to obtain the desirable TBR.

The neutron fluence at the location of TF coils was also examined. After 30 full-power years (FPY) of operation at 18.1 MW/m^2 neutron wall loading, the maximum fast-neutron ($E_n \geq 0.1$ MeV) fluence was found to be insensitive to ^{6}Li enrichment. For beryllium zone thicknesses of 0.1, 0.2, and 0.3 m, the maximum fast-neutron fluences

Table 16.3-II.

IMPACT OF ^{6}Li ENRICHMENT ON BLANKET PERFORMANCE[a]

^{6}Li Enrichment (%)	7.42	30.	60.
Tritium-breeding ratio	0.982	1.269	1.361
Blanket energy multiplication, M	1.42	1.37	1.35
Fraction (% of M) of nuclear energy in			
First wall	8.3	8.8	9.0
Beryllium zone	63.4	66.2	67.1
Shield	28.3	25.0	23.9
Energy leakage (% of M)	2.5	2.5	2.4
Maximum fluence[b] at TF coils (n/cm^2)	8.8×10^{22}	8.7×10^{22}	8.7×10^{22}

(*a*) For 0.15-m Be zone and 0.25-m shield designs at 18 MW/m^2 neutron wall loading.

(*b*) Fast-neutron fluence ($E_n \geq 0.1$ MeV) for 30 FPY of operation.

at the TF coils are, respectively, 2.3×10^{23}, 9×10^{22}, and 3.3×10^{22} n/cm^2. Since the fast-neutron-fluence limit to the spinel insulators is determined to be 2×10^{23} n/cm^2 (Section 10.2.3), a beryllium zone thicker than 0.15 m will be adequate to ensure a 30-FPY lifetime for the TF coils. Note that a single-piece maintenance procedure is envisioned for the TITAN-II design (Section 20). The complete FPC, including the TF coils, is replaced each year during the scheduled maintenance. The used TF coils are separated from the replaced FPC and are reused on a new reactor torus.

Further scoping studies were performed for a 0.15-m-thick beryllium zone and a 0.25-m-thick shield (for a total blanket and shield thickness of 0.4 m). Table 16.3-II summarizes the results of neutronics calculations for three different ^{6}Li enrichments of 7.42%, 30%, and 60%. The case of natural enrichment does not yield adequate tritium breeding and for enrichments above 30% the blanket performance is rather insensitive to the enrichment levels. From the results shown in Table 16.3-II, a set of preliminary performance parameters can be obtained: (1) a blanket energy multiplication of about

Table 16.3-III.

COMPARISON OF NEUTRONICS PERFORMANCE OF BERYLLIUM MULTIPLYING BLANKETS[a] WITH H_2O AND D_2O-BASED LITHIUM-NITRATE COOLANTS

	Coolant Type			
	H_2O		D_2O	
^{6}Li enrichment (%)	7.42	30.	7.42	30.
Tritium-breeding ratio	0.982	1.269	0.936	1.217
Blanket energy multiplication	1.42	1.37	1.44	1.39
TF-coil heating rate (W/cm^3)	4.6	4.2	7.2	6.7

(*a*) For 0.15-m Be zone and 0.25-m shield designs at 18 MW/m^2 neutron wall loading.

1.38 for a TBR of 1.2; (2) the nuclear energy deposited in the TF coils, the pool water, and the OH coils is about 2.5% of the total nuclear energy deposited in the first wall, blanket, and shield; (3) the maximum fast-neutron fluence at the TF coils is less than 1×10^{23} n/cm^2; and (4) the needed ^{6}Li enrichment is 30% or less for obtaining a TBR of 1.2 in the full-coverage 1-D analysis.

Heavy water (D_2O) as the coolant

The option of using heavy water (D_2O) as the coolant for the TITAN-II design was considered because D_2O has a lower neutron-absorption cross section than ordinary water (H_2O). Furthermore, deuterium has a significant (n,2n) cross section of about 0.1 barn at 14 MeV. It is also of interest to investigate whether D_2O can be used without any beryllium in the TITAN-II concept.

Two additional neutronics calculations were performed for the 0.15-m-thick beryllium zone blanket of Table 16.3-II. In these calculations, H_2O was replaced by D_2O while all other blanket parameters remained the same. Table 16.3-III compares the results of these calculations with those obtained with H_2O as the coolant. The results show

that the ordinary-water blanket is able to breed more tritium than the heavy-water one, within the range of blanket parameters used, because hydrogen has a better neutron-moderation capability than deuterium. As a result, the neutron-leakage rate into the TF coils is expected to be higher in the D_2O blanket than in the H_2O blanket, as is seen in Table 16.3-III. The D(n,2n) reactions do not significantly contribute to tritium breeding, since beryllium is the major neutron multiplier with a multiplication factor of 15 or more higher than that of the heavy water under the specified blanket parameters.

The need for the beryllium multiplier in the TITAN-II design is demonstrated by considering four different designs without Be:

1. 0.3-m blanket and 0.1-m shield, D_2O coolant, 60% ^6Li,
2. 0.6-m blanket and no shield, D_2O coolant, 30% ^6Li,
3. 0.6-m blanket and no shield, D_2O coolant, 60% ^6Li, and
4. 0.6-m blanket and no shield, H_2O coolant and 60% ^6Li.

The compositions in the above blankets are identical to those in the previous study, except that beryllium is replaced by either D_2O or H_2O with the corresponding $LiNO_3$ content of the solution.

Table 16.3-IV summarizes the results for these four cases. It is clear that without beryllium, both D_2O and H_2O $LiNO_3$ blankets have insufficient TBRs. Marginal breeding ratios can be achieved for a blanket with a structural content of about 1% or 2% and with D_2O as the coolant.

The fast-neutron fluence at the TF coils for the first blanket considered (total thickness of 0.4 m) is about the same as the blanket design containing beryllium (Table 16.3-II). The latter indicates that water (either light or heavy water) itself is a very good neutron moderator, but lacks adequate neutron-multiplication capability.

Effect of beryllium density factor

Scoping studies were performed to assess the impact of the beryllium zone thickness and density factor on optimized blanket-energy multiplication and beryllium utilization. The blanket composition in this set of calculations includes a 15-mm-thick first wall with 16.7% structure, 61.8% coolant, and a balance of void. A variable-thickness beryllium

zone was considered consisting of 12.2% structure, 58.7% beryllium, and 29.1% coolant, according to a more up-to-date mechanical design of the FPC. Two beryllium density factors, 1.0 and 0.8, were considered. A 0.15-m-thick breeder/reflector zone with 9% structure and 91% aqueous coolant and a 0.1-m-thick shield with 90% structural metal and 10% aqueous coolant are located behind the Be zone.

Figure 16.3-1 shows the Be (n,2n) reaction rate as a function of beryllium zone thickness which indicates that for a 0.3-m-thick beryllium zone, the reaction rate is about saturated for both density factors of 1.0 and 0.8. When the beryllium zone thicknesses are 0.1, 0.15, and 0.2 m, the corresponding Be (n,2n) reaction rates relative to the value

Table 16.3-IV.

NEUTRONICS PERFORMANCE OF D_2O- AND H_2O-BASED $LiNO_3$ BLANKETS[a] WITHOUT BERYLLIUM NEUTRON MULTIPLIER

	Case 1	Case 2	Case 3	Case 4
Blanket thickness (m)	0.3	0.6	0.6	0.6
Shield thickness (m)	0.1	0.0	0.0	0.0
Coolant [b]	D_2O	D_2O	D_2O	H_2O
^6Li enrichment (%)	60.	30.	60.	60.
Tritium-breeding ratio	0.850	0.987	0.993	0.880
Blanket energy multiplication	1.12	1.16	1.15	1.13
D (n,2n)	0.130	0.140	0.140	N/A
TF-coil heating rate (W/cm^3)	7.7	3.4	3.2	2.5
Fluence[c] at TF coils (n/cm^2)	1.0×10^{23}	2.5×10^{22}	2.2×10^{22}	1.8×10^{22}

(*a*) For designs with 9% ferritic-steel structure and 18 MW/m^2 neutron wall loading.

(*b*) The coolant is an aqueous $LiNO_3$ solution containing 5 at.% lithium.

(*c*) After 30 FPY of operation.

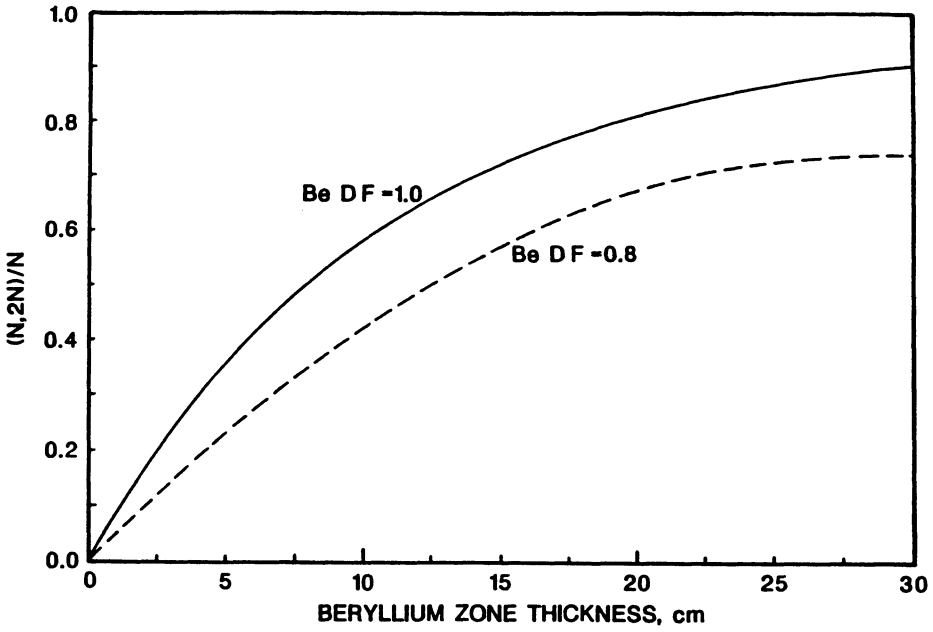

Figure 16.3-1. Beryllium neutron-multiplication factor in the TITAN-II design as a function of beryllium zone thickness for beryllium density factors (D.F.) of 0.8 and 1.

at 0.3 m are 0.64, 0.77 and 0.9, respectively. The Be (n,2n) reaction rate is almost directly proportional to the beryllium density factor (packing fraction) used. Hence, a beryllium design with a 0.8 density factor will produce a 20% lower neutron-multiplication factor than a design with a density factor of 1.0.

The ultimate impact of a lower-density beryllium on the neutronics performance of the TITAN-II design is a lower blanket energy multiplication (M) when the TBRs in these designs are fixed at 1.2 by adjusting the ^{6}Li enrichment. A preliminary design study was performed using a 0.15-m-thick beryllium zone as the base blanket for the design analysis. Two beryllium zone compositions were considered in the preliminary structural design study: Case A with 12.2% structure, 29.1% coolant, and 58.3% beryllium; and Case B with 15% structure, 20.5% coolant, and 64.5% beryllium. For each case, two beryllium density factors of 0.8 and 1.0 were considered. Natural lithium in the aqueous coolant is used when the beryllium density factor is 1.0, while 20% ^{6}Li enrichment is used for the designs when the beryllium density factor is 0.8. These ^{6}Li enrichments were chosen primarily to make sure that these preliminary designs result in reasonable TBRs (> 1).

Table 16.3-V shows the neutronics performance for these blankets with these two beryllium zone compositions. For a beryllium density factor of 0.8, both cases have equal

Table 16.3-V.

COMPARISON OF NEUTRONICS PERFORMANCE OF PRELIMINARY TITAN-II BLANKET DESIGNS[a]

	Case A		Case B	
Compositions of Be zone (%)				
Beryllium	58.7		64.5	
Coolant	29.1		20.5	
Structure	12.2		15.0	
Beryllium density factor	1.0	0.8	1.0	0.8
^{6}Li enrichment (%)	7.4	20.	7.4	20.
Tritium-breeding ratio	1.06	1.19	1.01	1.18
Blanket energy multiplication, M	1.38	1.31	1.43	1.34
Be(n,2n) reaction rate	0.684	0.573	0.740	0.624
Nuclear energy leakage (% of M)	2.8	3.3	2.6	3.1

(*a*) All calculations were obtained with the following system:
First wall (15 mm): 16.7% structure, 61.8% coolant, and 21.5% void;
Beryllium zone (0.15 m): Two variable compositions as shown;
Breeder/reflector zone (0.15 m): 9% structure and 91% coolant;
Shield (0.1 m): 90% structure and 10% coolant; and
Coolant: aqueous (H_2O) $LiNO_3$ solution containing 5 at.% lithium.

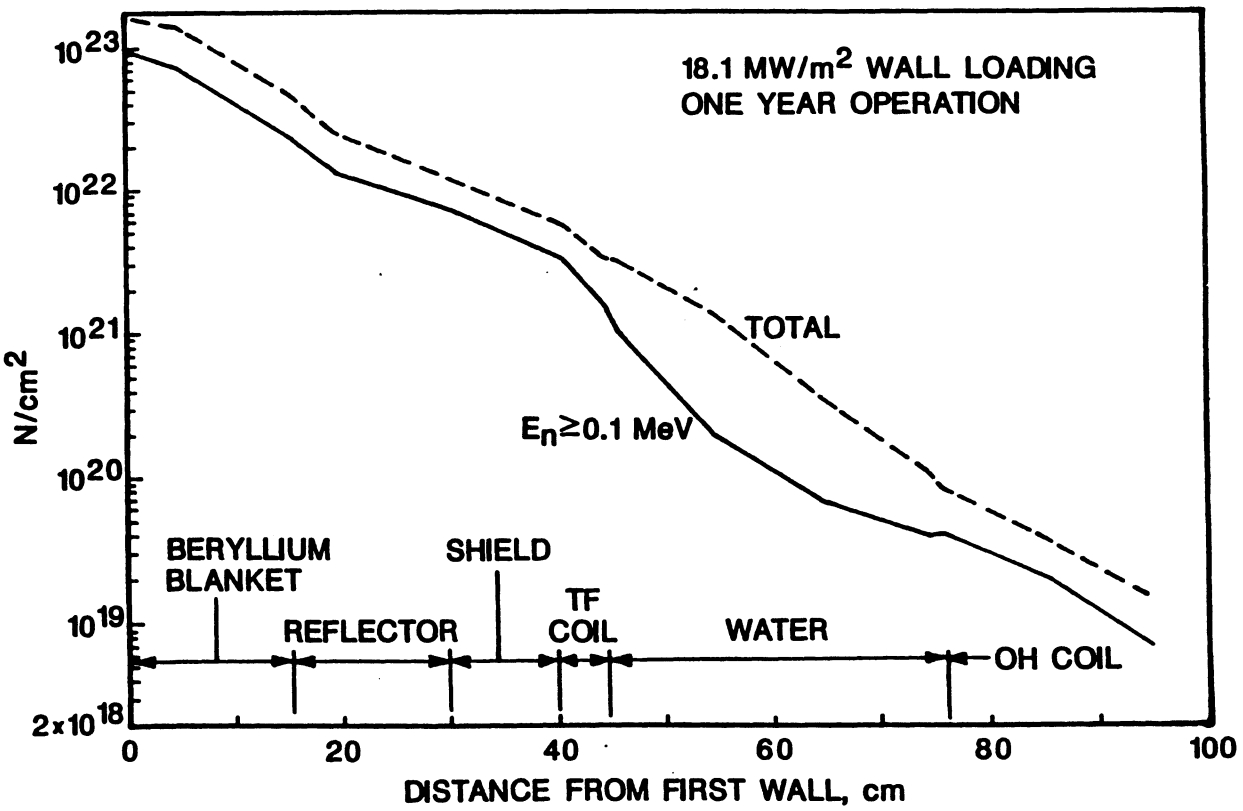

Figure 16.3-2. Total and fast-neutron ($E_n \geq 0.1\,\text{MeV}$) flux distributions in TITAN-II components as a function of distance from the first wall.

TBRs of 1.2 and roughly equal M (1.31 for Case A and 1.34 for Case B). For a Be density factor of 1.0, M increases to 1.38 and 1.43, respectively, for Cases A and B. However, the TBRs are reduced to 1.06 and 1.01. If the TBRs are adjusted to about 1.2 by increasing the ^{6}Li enrichment in lithium, M will decrease slightly to about 1.36 and 1.40. This study suggests that the reduction of the beryllium density factor from 1.0 to 0.8 will cause M to decrease by about 4%.

Figure 16.3-2 shows the neutron-flux distribution as a function of distance from the first wall for Case A with a beryllium density factor of 0.8 and a ^{6}Li enrichment of 20%. The maximum fast-neutron fluence at the TF coils is about 3×10^{21} n/cm^2 after 1 FPY of operation at 18.1 MW/m^2 neutron wall loading. Therefore, TF and OH coils can be used for the lifetime of the power plant with no replacement, since the fast-neutron fluence after 30 FPY is about a factor of 2 to 3 below the radiation-damage limit to the spinel insulator. This margin may provide an incentive to move the OH coils closer to the blanket system in order to improve the coupling between the OH coils and the plasma.

16.3.2. Reference Design

Based on the above scoping studies, the following parameters were selected for the TITAN-II reference design: a 0.2-m-thick beryllium zone with a beryllium density factor of 0.9 (a maximum value when beryllium swelling is considered); a 0.1-m-thick breeder/reflector zone; and only a 50-mm water gap region between the TF and OH coils, bringing the OH coils closer to the blanket system by 0.3 m. Also, a higher $LiNO_3$ concentration (6.4 at.%) in the aqueous coolant is used because of heat-transfer considerations. The ^6Li enrichment level is chosen to achieve a TBR of 1.2. The schematic and materials composition of the TITAN-II reference design are illustrated in Figure 16.3-3.

The neutronics performance of the reference design is summarized in Table 16.3-VI and compared to three alternate designs with no breeder/reflector zones and 0.3-m-thick beryllium zones. The TBR is calculated to be 1.22 for the reference design when the ^6Li enrichment is 12%. The corresponding ^6Li enrichment for the alternate designs with thicker beryllium zones is also 12%. The blanket energy multiplication for the reference design is 1.36 and 1.40 for the alternate design because of its thicker beryllium zone. The nuclear energy leakages to the TF coil, water, and OH coils are also given in Table 16.3-VI, and are very similar in these designs with a 2.8% total leakage of the blanket energy from the high-temperature zones. The volumetric nuclear-heating rates in the reference and alternate (12% ^6Li enrichment) designs are displayed, respectively, in Figures 16.3-4 and 16.3-V.

16.4. THERMAL AND STRUCTURAL DESIGN

The TITAN-II design uses an aqueous salt solution ($LiNO_3$ in ordinary water) as the primary coolant. Major parameters of the TITAN-II design are given in Table 16.1-I. The configuration of the first wall, blanket, and shield is shown in Figures 16.1-1 through 16.1-4. The coolant channels are in the poloidal direction. The coolant enters at the bottom and exits at the top of the torus. One set of coolant channels runs along the outboard side of the torus and another set along the inboard side. The geometry of the coolant channels is shown in Figure 16.4-1. The cross section of the first wall is a semicircular channel with the convex side facing the plasma. The outer diameter is 3 cm and the wall thickness is 1.5 mm, including a 0.25-mm erosion allowance.

The blanket is made of rectangular-cross-section lobes attached to the first-wall coolant channels. The outer dimensions of the blanket lobes are 3 cm toroidally and

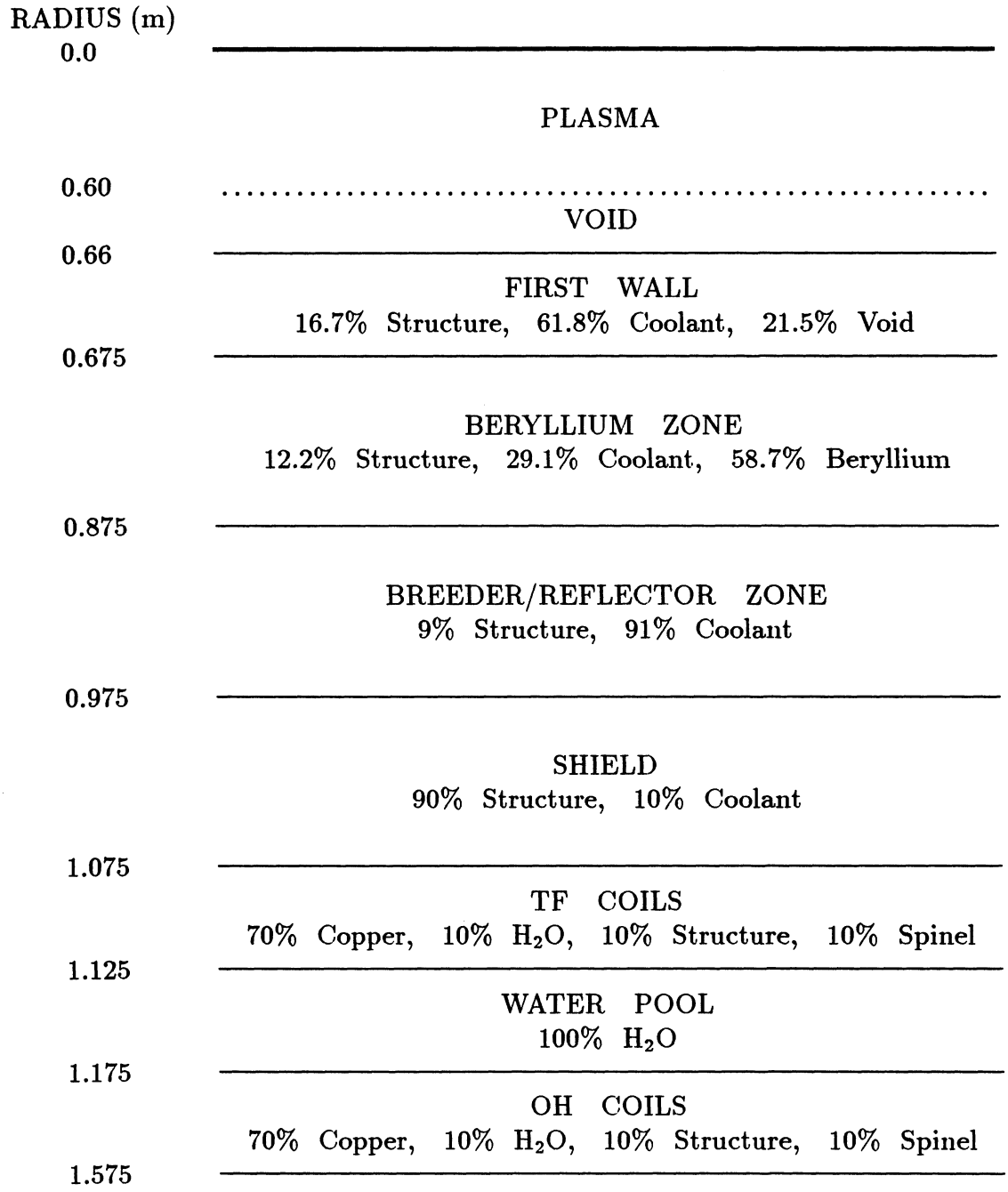

Figure 16.3-3. Schematic of the blanket and shield for the TITAN-II reference design. The coolant is an aqueous $LiNO_3$ solution (6.4 at.% Li) and beryllium density factor is 90%.

Table 16.3-VI.

NEUTRONICS PERFORMANCE OF THE TITAN-II REFERENCE AND ALTERNATE BLANKET DESIGNS

	Reference Design	Alternate Designs		
Beryllium zone thickness (m)	0.2		0.3	
Breeder/reflector zone thickness (m)	0.1		0.0	
Shield thickness (m)	0.1		0.1	
^{6}Li enrichment (%)	12.	7.42	12.	15.
Tritium-breeding ratio	1.22	1.08	1.20	1.25
Blanket energy multiplication, M	1.36	1.42	1.40	1.39
Fraction (% of M) of nuclear energy in				
First wall	12.4	11.8	12.1	12.2
Beryllium zone	69.2	81.0	81.5	81.5
Breeder/reflector zone	12.7	–	–	–
Shield	5.7	7.2	6.4	6.3
Energy leakage (% of M) to				
TF coils	1.27	1.43	1.40	1.38
Water pool	0.31	0.30	0.30	0.30
OH coils	1.09	1.11	1.11	1.12
TOTAL:	2.67	2.84	2.81	2.80

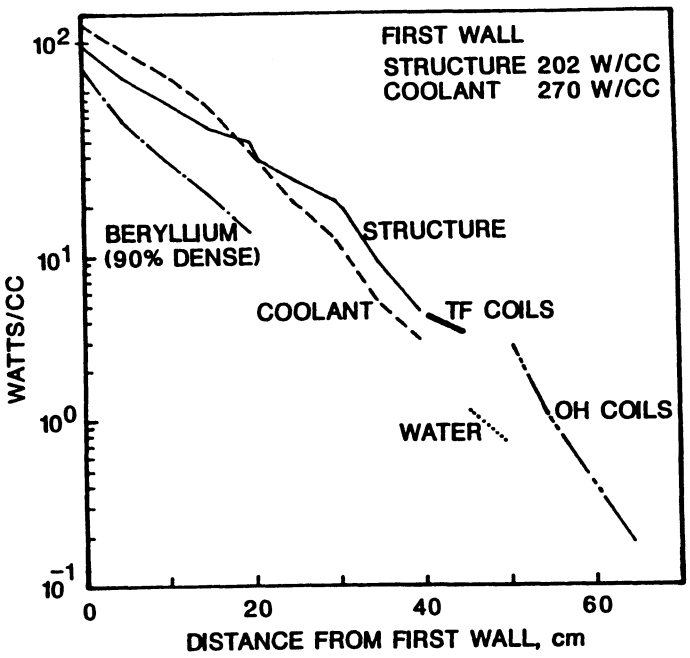

Figure 16.3-4. Volumetric nuclear heating rates in the reference TITAN-II design (18.1 MW/m^2 neutron wall loading) as a function of distance from the first wall.

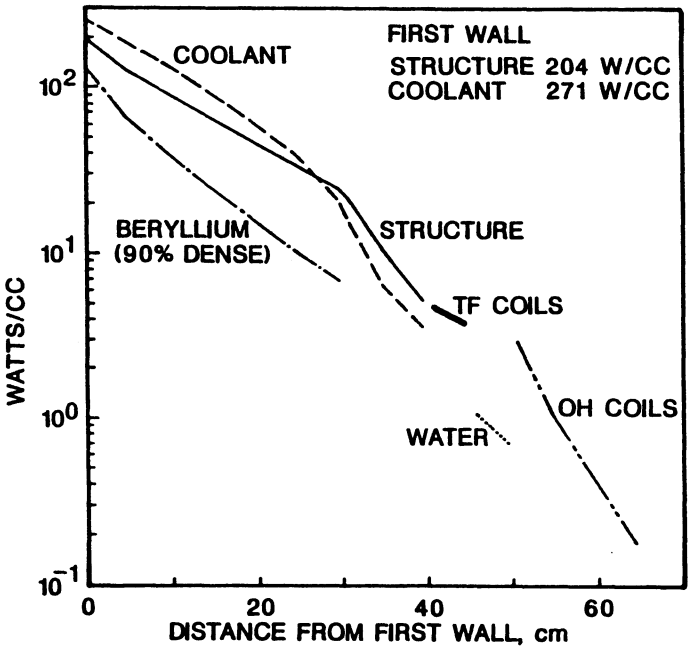

Figure 16.3-5. Volumetric nuclear heating rates in the alternate TITAN-II design (12% ^{6}Li enrichment and 18.1 MW/m^2 neutron wall loading) as a function of distance from the first wall.

30 cm radially. The lobe wall thickness is 1.4 mm. The first 20 cm of the blanket lobe (the multiplier zone) contains 7 rows of beryllium rods clad in 9-C, with a diameter of 2.6 cm. The thickness of the clad is 0.25 mm. The multiplier zone contains 12% structure, 59% beryllium, and 29% coolant (all by volume). Nuclear-heating rate in the blanket decreases away from the first wall. Therefore, to ensure proper coolant velocity, poloidal flow separators are placed behind the 2nd, 4th, and 7th rows of beryllium rods to form channels which have individual orifices. The remaining 10 cm of the blanket lobe (the breeder/reflector zone) does not contain beryllium and consists of 9% structure and 91% coolant (by volume). Behind the breeder/reflector zone, there is a 10-cm-thick shield. The shield contains two rows of circular coolant channels. The volume percentages of structure and coolant in the shield are 90% and 10%, respectively.

A review of the thermal analysis of the TITAN-II FPC is given in Section 16.4.1. The thermal-hydraulic parameters of the reference design are summarized in Section 16.4.2. The structural design of the FPC is presented in Section 16.4.3.

16.4.1. Thermal Analysis

The design peak heat flux on the first wall due to plasma radiation is 4.6 MW/m^2, corresponding to a plasma radiation fraction of 0.95. The coolant is an aqueous $LiNO_3$ solution with a lithium concentration of 6.4 at.% and a base pressure of 7 MPa. The inlet and exit temperatures of the coolant are, respectively, 298 and 330 °C. The resulting exit subcooling is 17 °C and, at moderate coolant velocities, nucleate boiling will take place

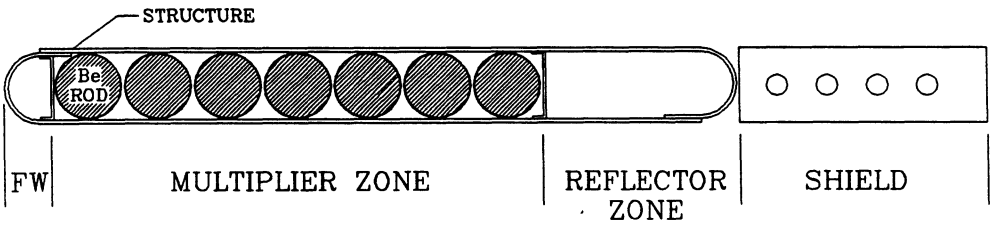

Figure 16.4-1. Geometry of the first-wall, blanket, and shield coolant channels.

in the first-wall coolant channels because of the high heat flux. Therefore, the mode of heat transfer in the first-wall coolant channels will be subcooled flow boiling (SFB). On the other hand, the heat load in the blanket and shield coolant channels is by volumetric nuclear heating only. The resulting heat flux on the coolant surface is smaller than that on the first wall. The maximum heat flux is less than $1\,MW/m^2$. Therefore, at these coolant velocities in the blanket and shield coolant channels, boiling will not take place and non-boiling, forced-convection heat transfer is sufficient to remove the heat.

16.4.1.1. Subcooled flow boiling

The maximum value of the average coolant temperature is always less than the boiling point by at least 17 °C. Any boiling will, therefore, be subcooled boiling. When the wall temperature exceeds the saturation temperature, boiling begins. Bubbles form at nucleation sites, grow, and detach from the wall. In the bulk of the coolant, where the temperature is lower than the boiling point, the bubbles collapse. Flow boiling is a highly efficient mode of heat transfer. The boiling process suffers a drastic reduction in heat-transfer capability when the heat flux exceeds a certain limiting value termed critical heat flux. Beyond the critical heat flux, the boiling process changes from nucleate boiling to film boiling and the heat transfer capability is much less than that of the critical heat flux. If the surface heat flux is not correspondingly reduced in such a case, the wall temperature will drastically increase and may result in melting of the wall material. This is more likely to happen in designs with a constant heat flux.

Three important parameters govern boiling heat transfer: the incipience of boiling, the wall superheat corresponding to a given surface heat flux, and the critical heat flux for the given coolant and flow conditions. Complete physical understanding of the boiling phenomena and theoretical solutions to different problems are not available at present. However, extensive experiments have been performed with different types of boiling heat transfer, mainly with pure liquids, and many empirical correlations are available. Since pure water (without additives) is used as coolant in many boiling heat-transfer applications, most of the boiling heat-transfer data are for water. It is expected that when additives are mixed with water, as is the case for TITAN-II, the boiling heat-transfer capability as measured by the critical heat flux will increase. However, only very limited data are available in this area. Therefore, the correlations for boiling heat transfer of pure water are used for the aqueous coolant of TITAN-II with appropriate corrections for changes in coolant properties resulting from the addition of the salt (Section 16.2.3).

Incipience of boiling

A semi-empirical correlation for the heat flux for incipience of boiling at a given wall superheat is provided by Bergles and Rohsenow [126]. Conversion to more convenient SI units yields

$$q_i'' = 0.0155\, p^{1.156} \left[\frac{9}{5}(T_w - T_{sat})\right]^{2.047/p^{0.0234}}, \qquad (16.4\text{-}1)$$

where q_i'' is the incipient heat flux (MW/m^2), p is the pressure (MPa), and T_w and T_{sat} are, respectively, the wall and saturation temperatures (°C). This correlation is valid for all velocities and represents the numerical data for water quite accurately over a pressure range of 0.1 to 14 MPa (15 to 2000 psia).

Equation 16.4-1 can be used to determine if boiling will take place or if the heat-transfer mechanism will remain purely convective at a given flow velocity, pressure, and heat flux. If the wall temperature obtained from the assumption of pure forced-convection heat transfer is greater than that given by Equation 16.4-1, then boiling will take place. In this case, the wall temperature should be calculated from the boiling equations given below.

Wall superheat in subcooled-flow-boiling heat transfer

Several correlations are available for calculating wall superheat corresponding to a given heat flux in fully developed, forced convection, nucleate-boiling heat transfer. The following three equations (converted to SI units) are by Jens and Lottes [127], Weatherhead [128], and Thom *et al.* [129], respectively:

$$T_w - T_{sat} = \frac{100}{3}\left(\frac{q''}{3.152}\right)^{1/4} \exp\left(-\frac{p}{6.207}\right), \qquad (16.4\text{-}2)$$

$$T_w - T_{sat} = (47.74 - 0.127\, T_{sat})\left(\frac{q''}{3.152}\right)^{1/4}, \qquad (16.4\text{-}3)$$

$$T_w - T_{sat} = 40\left(\frac{q''}{3.152}\right)^{1/2} \exp\left(-\frac{p}{8.690}\right), \qquad (16.4\text{-}4)$$

with temperature in °C, pressure in MPa, and the heat flux in MW/m^2.

Equations 16.4-2 and 16.4-3 are based on the assumption that the surface characteristics do not significantly influence the position of the fully developed boiling curve in

forced convection. Equation 16.4-4 appears to be in better agreement with experimental data. At higher heat fluxes, Equation 16.4-4 by Thom *et al.* [129] predicts highest wall superheat among the three equations and, therefore, will give a conservative estimate for the wall temperature of the first-wall coolant channel. Hence, Equation 16.4-4 is used in the thermal-hydraulic design of the TITAN-II FPC.

Critical heat flux

In any application of boiling heat transfer, it must be ensured that the maximum possible heat flux is less than the critical heat flux (CHF) by a certain safety margin. A large amount of data for internal flow boiling CHF for pure liquids, especially for water, is available and many empirical correlations for the CHF exist. Because of the scatter in the data, these correlations are generally accurate to $\pm 20\%$ over the applicable range of the data. Therefore, the CHF given by the different correlations may vary by as much as 40% [130].

The particulars about boiling in the first-wall coolant channels of TITAN-II are: the heat flux varies circumferentially, the flow is upward, and the coolant is an aqueous salt solution (not pure water). Since boiling is a localized phenomenon, circumferential variation of heat flux is not likely to affect the CHF. This has been shown to be the case by an experiment conducted at Oak Ridge National Laboratory [131].

It has been shown by Hasan *et al.* [132] that the direction of flow relative to gravity does not affect the CHF at high flow velocities in external flow boiling. They found that in subcooled or near-saturation boiling of methyl and ethyl alcohols flowing across a horizontal cylinder, the flow direction does not have any effect on the CHF for velocities in excess of about 1 m/s. The coolant velocity in the first-wall coolant channel is about 20 m/s. Therefore, the flow direction is not expected to have any effect on the CHF in the first-wall coolant channels of TITAN-II.

Several correlations for critical heat flux (q''_{CHF}) in flow boiling of pure liquids are available. The following correlation (converted to SI units) is by Jens and Lottes [127] and is based on the data for water only:

$$q''_{CHF} = C \left(\frac{G}{1356} \right)^m (\Delta T_{sub})^{0.22}, \qquad (16.4\text{-}5)$$

where G is the mass velocity of the coolant ($= \rho v$) in kg/m^2-s, the factor 1356 aries from the conversion of units, ΔT_{sub} is the local subcooling in °C, and q''_{CHF} is in MW/m^2.

Constants C and m depend on the pressure, p (MPa), through

$$C = 3.00 - 0.102\,p\,, \tag{16.4-6}$$

$$m = \frac{p}{30} + 0.04\,. \tag{16.4-7}$$

Data used in deriving the above CHF correlation was limited to maximum values of CHF of 38 MW/m^2, water velocity of 17 m/s, pressure of 13.6 MPa, and local subcooling of 90 °C.

A subcooled empirical correlation for the CHF developed by Tong [133], has the following form (after conversion to SI units):

$$q''_{CHF} = (0.725 + 1.93 \times 10^{-4}\,G) \times (3.0 + 0.018\,\Delta T_{sub}) \times (0.435 + 1.23\,e^{-0.0093\,L/d_h}) \times (1.7 - 1.4\,e^{-a})\,. \tag{16.4-8}$$

The parameter, a, is given by

$$a = 0.532 \left(\frac{h_{sat} - h_{in}}{h_{fg}}\right)^{3/4} \left(\frac{\rho_f}{\rho_v}\right)^{1/3}\,. \tag{16.4-9}$$

The length and hydraulic diameter are denoted by L and d_h, respectively. The inlet enthalpy is h_{in} and the saturation enthalpy is h_{sat}. The heat of vaporization is h_{fg}, ρ_f is water density, and ρ_v is vapor density. Data used in deriving the above correlation were limited to maximum values of CHF of 12.6 MW/m^2, water velocity of 110.6 m/s, pressure of 19 MPa, local subcooling of 127 °C, and L/d_h of 365. Because the data for this correlation were obtained from uniform-heat-flux test sections, it is not clear whether the CHF predicted by Equation 16.4-8 is a local CHF or an average heat flux up to the critical point.

Another empirical correlation of CHF data in up-flow of water through vertical tubes was provided by Katto and cited in Reference [130]:

$$q''_{CHF} = q''_o \left(1 + K\,\frac{\Delta h_{sub}}{h_{fg}}\right)\,, \tag{16.4-10}$$

where parameters K, q''_o, and the Weber number, We, are given by:

$$K = 0.416 \left(\frac{\rho_v}{\rho_f}\right)^{0.133} We^{0.433} \left(0.0221 + \frac{d_h}{L}\right) \left(\frac{d_h}{L}\right)^{0.27}\,, \tag{16.4-11}$$

$$We = \frac{G^2\,L}{\sigma\,\rho_f}\,, \tag{16.4-12}$$

$$q''_o = 9.8 \times 10^{-8}\,G\,h_{fg} \left(\frac{\rho_v}{\rho_f}\right)^{0.133} We^{-0.433}\,\frac{(L/d_h)^{0.27}}{1 + 0.0031\,L/d_h}\,, \tag{16.4-13}$$

with σ being the surface tension of water and L being the length of the channel. The ranges of velocity and CHF are rather small for this correlation.

Of the three correlations, the Jens-Lottes correlation (Equation 16.4-5) is the simplest and has the range of parameters for boiling heat transfer which is close to those of the first-wall coolant channel of TITAN-II. In the region of high heat flux, the predictions of Equations 16.4-5 and 16.4-8 are close, but the prediction by Equation 16.4-10 is too small, probably because the equation is not applicable at high heat flux. For example, at 13.8 MPa, water velocity of 10 m/s, and exit subcooling of 20 °C, the predictions of critical heat fluxes for the first-wall channel of TITAN-II by the above three correlations are 6.8, 5.8, and 3.8 MW/m^2, respectively.

As explained before, correlation 16.4-8 probably underestimates the CHF. References cited in [130] show that the CHF is increased by about 40% with an aqueous solution of ethanol over pure water. Therefore, if the maximum heat flux is kept within 60% of that predicted by the correlation of Jens and Lottes, an adequate safety margin for CHF is available. Any increase in the CHF due to the lithium-salt content will add to the safety margin. The Jens-Lottes correlation (Equation 16.4-5) is used to check for CHF in the first-wall coolant channel in TITAN-II.

16.4.1.2. Maximum temperature of the first wall

The maximum structure temperature in the first-wall coolant channel is given by

$$T_{w,max} = T_{ex} + \Delta T_w + \Delta T_f \,, \tag{16.4-14}$$

where T_{ex} is the mixed-coolant exit temperature and ΔT_w and ΔT_f are the wall and film temperature drops, respectively. The maximum temperature drop across the wall is obtained from a 1-D, cylindrical-geometry heat conduction at the point of maximum radiation heat flux on the first wall. The maximum wall temperature drop is given by:

$$\Delta T_w = \frac{q_o'' a}{k_s} \ln\left(\frac{b}{a}\right) + \frac{q_w''' b^2}{2k_s} \ln\left(\frac{b}{a}\right) - \frac{q_w''' (b^2 - a^2)}{4k_s} \,, \tag{16.4-15}$$

where q_o'' is the maximum radiation heat flux, q_w''' is the volumetric heating rate in the channel wall, a and b are the inner and outer radii, respectively, and k_s is the thermal conductivity of the wall material. The film temperature drop, ΔT_f, is the result of subcooled flow boiling (Section 16.4.1.1) and can be written as $\Delta T_f = (T_w - T_{sat}) + \Delta T_{sub,ex}$, where $\Delta T_{sub,ex}$ is the subcooling at the channel exit. The wall superheat, $(T_w - T_{sat})$, is calculated from Equation 16.4-4 using the maximum radiation heat flux on the first-wall coolant channel.

16.4.1.3. Analysis of blanket and shield

In the multiplier and breeder/reflector zones of the blanket lobe and in the shield, the heat flux removed by the coolant is very low. The flow is turbulent in the channels of these regions. Forced-convective heat transfer is adequate to remove the heat without raising the wall temperature to the level which would initiate nucleate boiling. Therefore, the maximum structure temperatures in the blanket and shield are calculated under the condition of non-boiling, forced-convective heat transfer.

The film temperature drop is calculated from the forced-convection, turbulent-flow Nusselt number, Nu, which is given by the Dittus-Boelter equation:

$$Nu = 0.023\,(Re)^{0.8}\,(Pr)^{1/3}\,, \tag{16.4-16}$$

where $Re = \rho_f V d_h/\mu_f$ is the Reynolds number, $Pr = c_p\mu_f/k_f$ is the Prandtl number, and ρ_f, μ_f, c_p, and k_f are the density, viscosity, specific heat capacity, and thermal conductivity of the coolant, respectively. The coolant velocity is denoted by V and d_h is the hydraulic diameter of each zone. The film temperature drop is then obtained from:

$$\Delta T_f = \frac{q''\,d_h}{Nu\,k_f}\,. \tag{16.4-17}$$

The heat flux, q'', at the wall-coolant interface is determined from the volumetric nuclear-heating rates.

The important temperatures in the blanket and shield are those at the center of the beryllium rods, the clad, the channel wall, and the maximum temperature in the shield region. These temperatures should not exceed the design limits. The maximum temperatures are obtained by adding the film temperature drop and the temperature drops across the structural material and gap resistance to the coolant exit temperature. One-dimensional heat conduction is used to find the temperature drops in the structural material. The maximum center-line temperature of a beryllium rod, $T_{c,max}$, is given by:

$$T_{c,max} = T_{ex} + \Delta T_f + \Delta T_{clad} + \Delta T_{gap} + \Delta T_{Be}\,, \tag{16.4-18}$$

where ΔT_{clad}, ΔT_{gap}, and ΔT_{Be} are the temperature drops across the clad, gap, and the beryllium rod (from center to the surface), respectively:

$$\Delta T_{clad} = \frac{q'''_s\,(b^2 - a^2)}{4k_s} - \frac{(q'''_s - q'''_{Be})\,a^2}{2k_s}\,\ln\left(\frac{b}{a}\right)\,, \tag{16.4-19}$$

$$\Delta T_{gap} = \frac{q'''_{Be}\,a}{2h_{gap}}\,, \tag{16.4-20}$$

$$\Delta T_{Be} = \frac{q'''_{Be}\,a^2}{4k_{Be}}\,, \tag{16.4-21}$$

where q_s''' and q_{Be}''' are the volumetric nuclear-heating rates in the structure (cladding) and beryllium rod, respectively. The thermal conductivities of the structural material and beryllium are, respectively, k_s and k_{Be}, and the heat-transfer coefficient for the gap is h_{gap}.

The maximum blanket-lobe wall temperature, $T_{w,max}$, is given by:

$$T_{w,max} = T_{ex} + \frac{q_s''' t^2}{2k_s} + \frac{q_s''' t\, d_h}{Nu\, k_f}, \tag{16.4-22}$$

where t is the wall thickness.

The maximum temperature in the shield region, $T_{s,max}$, is given by:

$$T_{s,max} = T_{ex} + \frac{q_s'''(R^2 - r^2)}{Nu\, k_f} + \frac{q_s''' R^2}{2k_s} \ln\left(\frac{R}{r}\right) - \frac{q_s'''(R^2 - r^2)}{4k_s}, \tag{16.4-23}$$

where R is the radius of the shield region surrounding a coolant channel of radius r. The thermal-hydraulic design should ensure that none of the above three maximum temperatures, $T_{c,max}$, $T_{w,max}$, and $T_{s,max}$, exceeds the corresponding design-limit temperatures.

16.4.1.4. Pressure Drops

The pressure drop in the coolant circuit is caused by the friction in the coolant channel and bends, and by sudden contraction and expansion at the inlet and outlet. In the first-wall coolant channel, the pressure drop will be increased because of the two-phase flow which results from subcooled flow boiling. In the blanket- and shield-coolant channels, the friction pressure drop is given by:

$$\Delta p_f = f \frac{\rho_f V^2}{2d_h} L, \tag{16.4-24}$$

where f is the friction factor which is a function of the Reynolds number and the wall roughness parameter for turbulent flow. The friction factor is given in the Moody diagram available in texts on fluid dynamics [134].

Friction pressure resulting from sudden expansion and contraction or occurring at a 90° bend is given by:

$$\Delta p_f = \alpha \frac{\rho_f V^2}{2g}, \tag{16.4-25}$$

where g is the gravity acceleration. The factor α is equal to $0.5\,(1 - 1/n)$ for a sudden contraction and is equal to $(1 - 1/n)^2$ for sudden expansion with n being the ratio by which the flow area suddenly decreases or increases. For a circular channel with a 90° bend, the factor α depends on the ratio of the radius of curvature to the channel radius. When the ratio is 1, $\alpha = 0.6$ and when it is 5, $\alpha = 1.4$.

The pressure drop in subcooled flow boiling in the first-wall-coolant channel can be calculated from the following equation [135].

$$\left(\frac{dp}{dz}\right)_{SFB} = \left(\frac{dp}{dz}\right)_f \exp\left[\frac{2.65}{p}\left(\frac{q''_o}{q''_{SPL}} - 1\right)\right], \qquad (16.4\text{-}26)$$

where p is the pressure in MPa, $(dp/dz)_f$ is the pressure drop for single-phase flow and can be obtained from Equation 16.4-24 for unit channel length, and

$$q''_{SPL} = \frac{\Delta T_{sub,in} + \Delta T_{sat}}{(4L/G\,c_p\,d_h) + (d_h/Nu\,k_f)}. \qquad (16.4\text{-}27)$$

Here $\Delta T_{sub,in} = T_{sat} - T_{in}$ is the subcooling at the inlet and L is the channel length. The wall superheat, $\Delta T_{sat} = T_w - T_{sat}$, is given by Equation 16.4-4. Nusselt number, Nu is obtained from Equation 16.4-16 for purely convective heat transfer.

16.4.2. Reference Design

Figure 16.4-1 shows the cross sections of the first-wall, blanket, and shield coolant channels. The nuclear-heating rates in the FPC components are given in Figure 16.3-4. The input parameters relevant to the thermal-hydraulic design are given in Table 16.4-I. In the TITAN-II design, pressure drop and pumping power are not as limiting as the structure temperature and the base pressure of the coolant. The coolant base pressure is 7 MPa and the inlet and exit temperatures of the coolant are, respectively, 298 and 330 °C. The primary-coolant pressure has been selected to be lower than the steam-generator pressure (7.2 MPa) so that any leakage in the steam-generator tubes does not result in leaks of the tritium-containing primary coolant to the steam cycle. The necessity for an intermediate heat exchanger is thereby avoided. The coolant inlet and exit temperatures are selected to match the primary-coolant temperatures of a typical PWR power cycle, thus eliminating a full-scale power-cycle analysis.

The thermal-hydraulic design must ensure that the maximum structure temperatures, coolant velocities, and pressure drops do not exceed the design limits. The structure temperatures are determined by using the equations presented in Section 16.4.1. The coolant

velocities are determined by energy balance. The nuclear-heating rates in the structure, coolant, and beryllium rods are obtained from the neutronics analysis (Figure 16.3-4). The thermal-hydraulic reference design of TITAN-II first wall, blanket, and shield are given in Tables 16.4-II through 16.4-V.

The thermal-hydraulic design of TITAN-II is conservative in that the structure temperatures are well within the design limits. The critical heat flux in the first-wall channel is 8.34 MW/m^2 which is 63% higher than the peak heat flux crossing the coolant film (5.1 MW/m^2). The pumping power is 49 MW, nearly equal to that for TITAN-I. For coolant circulation, pumps supplying a head of 1 MPa are used. Because the coolant flows in parallel through the first wall, multiplier, reflector, and shield zones, orifices are used to reduce the pressure as necessary for each channel. Separate coolant supplies for each of the flow channels (or zones) would alleviate the need for orifices and reduce the pumping power considerably. However, the added complexity of more coolant systems and hydraulic separation of the flow channels does not justify this change.

16.4.3. Structural Analysis

The first wall and blanket of the TITAN-II design are integrated in the form of blanket lobes. The construction procedure for each blanket lobe is shown in Figure 16.4-2. Each

Table 16.4-I.

THERMAL-HYDRAULIC DESIGN PARAMETERS

First-wall heat flux	4.6	MW/m^2
Coolant inlet temperature	298	°C
Coolant exit temperature	330	°C
Coolant pressure	7	MPa
Structure temperature limit	550	°C
Pressure stress limit	200	MPa
Thermal stress limit	400	MPa

Table 16.4-II.

THERMAL-HYDRAULIC DESIGN OF TITAN-II FIRST WALL

Channel outer diameter, b	30.0	mm
Channel inner diameter, a	27.0	mm
Wall thickness, t	1.5	mm
Erosion allowance	0.25	mm
Structure volume fraction	0.17	
Coolant volume fraction	0.62	
Void volume fraction	0.21	
Volumetric heating (structure)	202	MW/m^3
Volumetric heating (coolant)	270	MW/m^3
Total thermal power	770.2	MW
Coolant inlet temperature, T_{in}	298	°C
Coolant exit temperature, T_{ex}	330	°C
Maximum wall temperature, $T_{w,max}$	503	°C
Coolant pressure, p	7	MPa
Maximum primary stress	98	MPa
Maximum secondary stress	363	MPa
Coolant flow velocity, U	22.6	m/s
Mass flow rate	1.15×10^4	kg/s
Volumetric flow rate	10	m^3/s
Pressure drop, Δp	0.5	MPa
Total pumping power	12.5	MW
Reynolds number, Re	1.49×10^6	
Nusselt number, Nu	2360	
Prandtl number, Pr	16.5	
Critical heat flux, q''_{CHF}	8.3	Mw/m^2
Subcooling at exit, $T_{ex,sub}$	17	°C

Table 16.4-III.

THERMAL-HYDRAULIC DESIGN OF TITAN-II BERYLLIUM ZONE

Zone radial thickness	200	mm
Zone toroidal extent	30	mm
Wall thickness	1.4	mm
Structure volume fraction	0.12	
Coolant volume fraction	0.29	
Beryllium volume fraction	0.59	
Volumetric heating (structure)[(a)]	180	MW/m^3
Volumetric heating (coolant)[(a)]	240	MW/m^3
Volumetric heating (beryllium)[(a)]	140	MW/m^3
Total thermal power	1753.6	MW
Coolant inlet temperature	298	°C
Coolant exit temperature	330	°C
Maximum beryllium temperature	573	°C
Mass flow rate	2.6×10^4	kg/s
Volumetric flow rate	22.6	m^3/s
Coolant flow velocity[(a)]	14	m/s
Pressure drop[(a)]	1.0	MPa
Total pumping power	28.2	MW
Reynolds number[(a)]	2.7×10^5	
Nusselt number[(a)]	601	

(a) Values for the first cell of multiplier zone.

Table 16.4-IV.

THERMAL-HYDRAULIC DESIGN OF TITAN-II BREEDER/REFLECTOR ZONE

Zone radial thickness	100	mm
Zone toroidal extent	30	mm
Wall thickness	1.4	mm
Structure volume fraction	0.09	
Coolant volume fraction	0.91	
Volumetric heating (structure)	40	MW/m^3
Volumetric heating (coolant)	40	MW/m^3
Total thermal power	314.3	MW
Coolant inlet temperature	298	°C
Coolant exit temperature	330	°C
Maximum wall temperature	348	°C
Mass flow rate	4.66×10^3	kg/s
Volumetric flow rate	4.1	m^3/s
Coolant flow velocity	1	m/s
Pressure drop	5.0×10^{-4}	MPa
Total pumping power	5.1	MW
Reynolds number	1.5×10^5	
Nusselt number	376	

Table 16.4-V.

THERMAL-HYDRAULIC DESIGN OF TITAN-II SHIELD

Shield radial thickness	100	mm
Structure volume fraction	0.90	
Coolant volume fraction	0.10	
Total thermal power	159.8	MW
Coolant inlet temperature	298	°C
Coolant exit temperature	330	°C
Mass flow rate	2.44×10^3	kg/s
Volumetric flow rate	2.1	m^3/s
Total pumping power	2.6	MW
First Row of Channels		
Channel inner diameter	12.7	mm
Volumetric heating (structure)	22	MW/m^3
Volumetric heating (coolant)	10	MW/m^3
Maximum wall temperature	409	°C
Coolant flow velocity	6.5	m/s
Pressure drop	2.2×10^{-2}	MPa
Reynolds number	3.3×10^5	
Second Row of Channels		
Channel inner diameter	19.0	mm
Volumetric heating (structure)	9	MW/m^3
Volumetric heating (coolant)	5	MW/m^3
Maximum wall temperature	427	°C
Coolant flow velocity	3.7	m/s
Pressure drop	4.7×10^{-3}	MPa
Reynolds number	2.8×10^5	

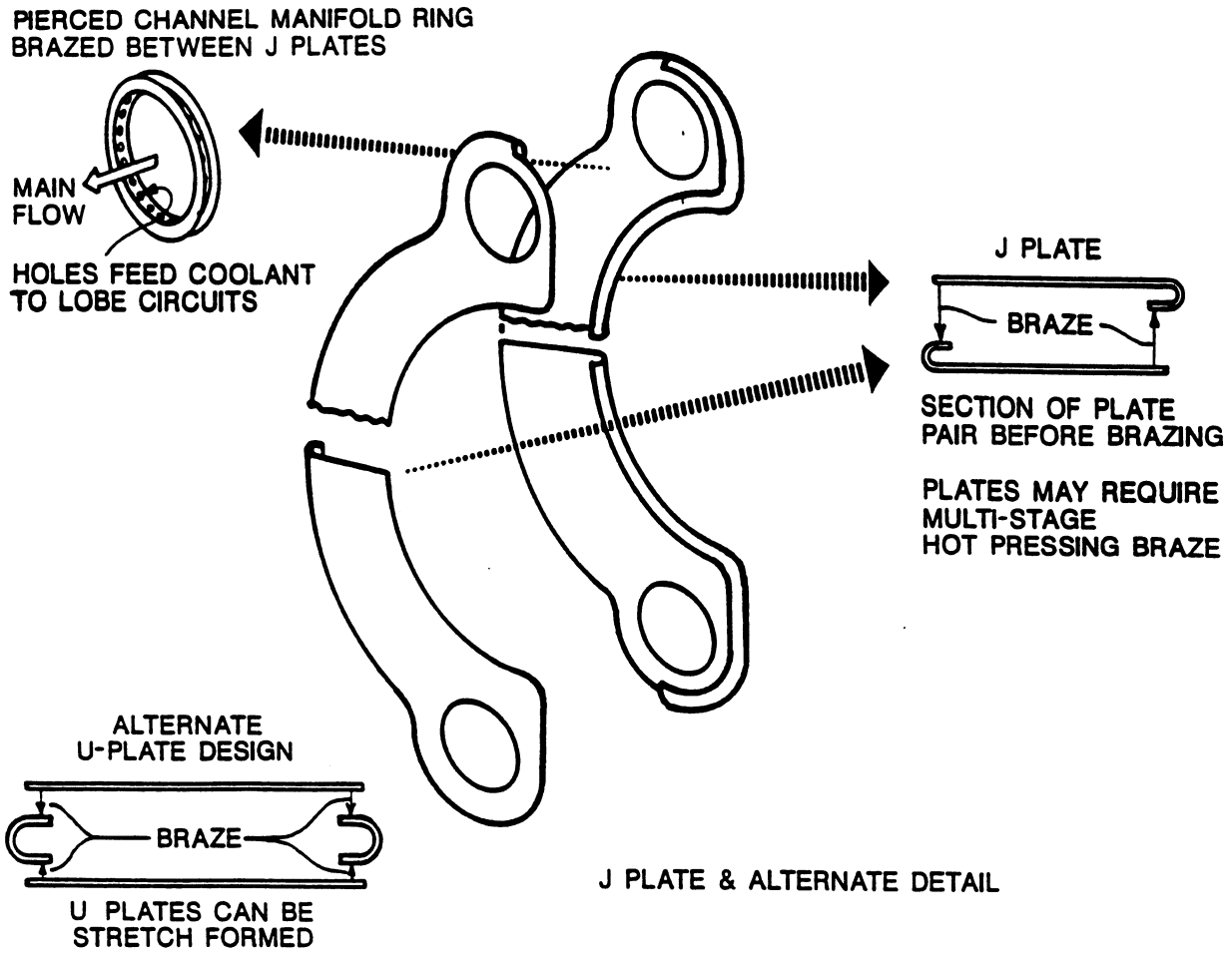

Figure 16.4-2. The TITAN-II blanket lobe, J-plate design.

blanket lobe is made of two plates, called "J-plates" because one edge of each plate is rolled to the appropriate radius to form a J-section. Both J-plates are made of the low-activation, high-strength ferritic steel, 9-C [2]. The first-wall plate is thicker than the other plate, since it is subject to erosion. Two plates are then brazed or welded together to form a complete blanket lobe. A channel manifold ring completes the lobe and allows the coolant and breeder mixture to flow. This configuration will require a multistage pressing operation, perhaps even hot-pressing to achieve this shape.

An alternate design, also shown in Figure 16.4-2, is the U-plate design. The advantages of this design are that the thin material can be used for both sides, and the edge U members are easier to make than the J-plates. However, acceptance of either configuration would depend on detailed investigation of the thick braze or weld area to ensure there is no focusing of thermal radiation or other heat-transfer problems.

Seventy blanket lobes are than stacked side-by-side to form a blanket module. The structural details of a blanket module are shown in Figure 16.4-3. This arrangement is structurally a membrane pressure vessel with balancing forces, derived from identical neighboring lobes, maintaining its flat sides. This configuration requires an external constraining structure to keep it pressed into oval form, which is readily derived from the shield as discussed below. The advantage of this design is that the structural fraction in the important near-first-wall radial zone is nearly as low as ideally possible, giving good tritium-breeding performance. This configuration also has a much lower void fraction when compared to a tubular design, giving a minimum-thickness blanket. The assembly technique for each blanket module is expected to be multistage brazing with intermediate leak checking. Since the lobes only require constraint in the blanket toroidal direction and because they are soft structurally in this direction, high precision is not necessary.

For the first wall, the structural-material temperature limit is taken at the centerline. The allowable peak, midline temperature of the 9-C alloy is 550 °C. The allowable primary stress, S_{mt}, for 9-C is 200 MPa. The coolant base pressure is 7 MPa. With the 4.6 MW/m^2 of surface heat loading, the lobe radius is conservatively selected at 1.5 cm. The first-wall thickness at the beginning of life (BOL) is selected at 1.5 mm. The plasma side of the first wall is designed with an erodible thickness of 0.25 mm. The BOL first-wall maximum surface temperature is 650 °C. The BOL midline temperature of 503 °C is 47 °C below the allowable temperature.

The primary stress, S_p, due to coolant pressure, is:

$$S_p = \frac{pr}{t} = 98.6 \text{ MPa}, \qquad (16.4\text{-}28)$$

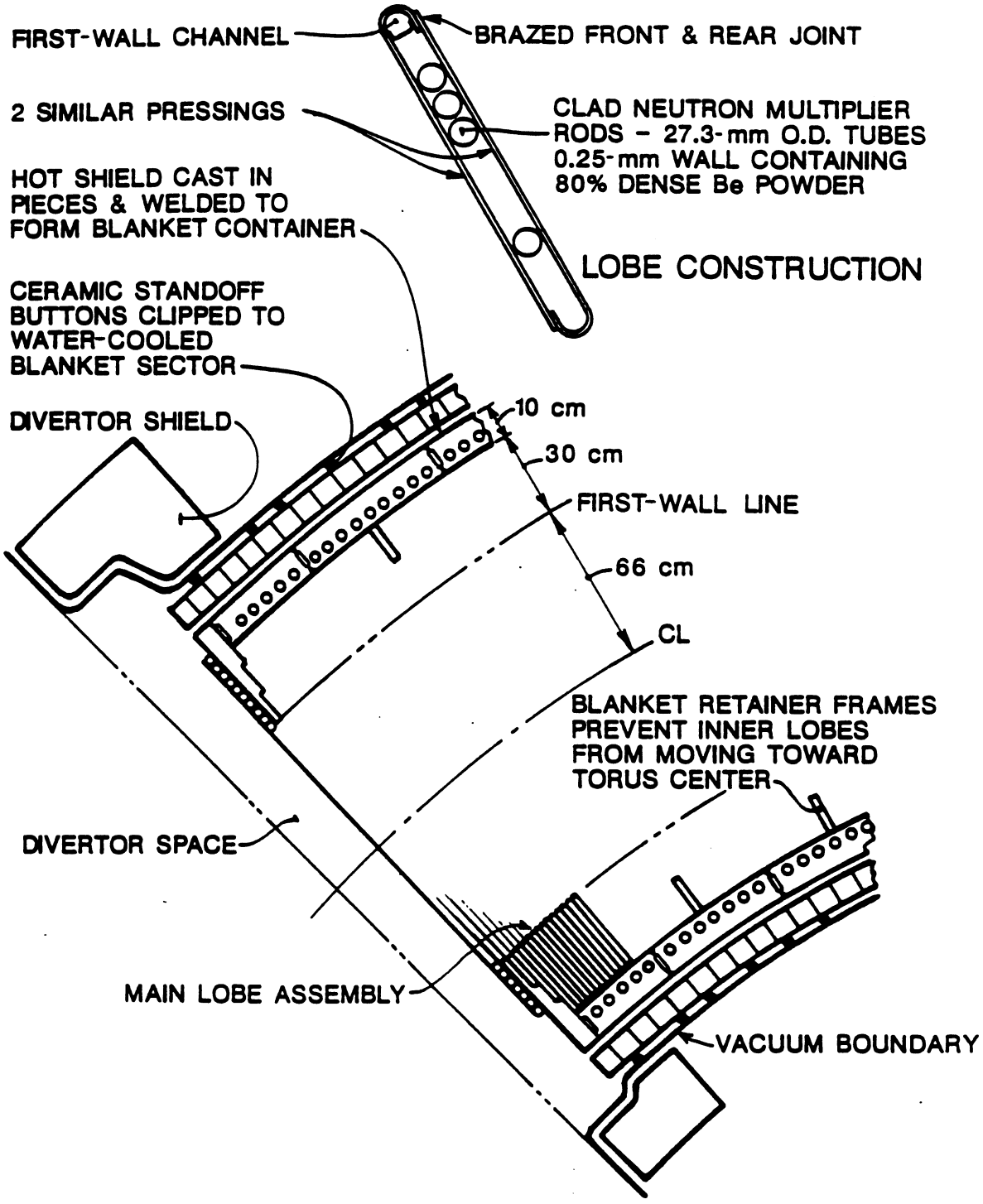

Figure 16.4-3. Equatorial-plane cross section of a TITAN-II blanket module.

where $r = 14.175\,\text{mm}$ is the lobe centerline radius and $t = 1.15\,\text{mm}$ is the wall thickness at the end of life.

The temperature stress, under these conditions, is a secondary stress with an allowable value of $2 \times S_{mt} = 400\,\text{MPa}$. The temperature stress in the TITAN-II first wall is estimated at:

$$S_{th} = \frac{\Delta T}{2}\frac{\alpha E}{1-\nu} = 363\ \text{MPa}, \tag{16.4-29}$$

for the temperature drop across the first wall of $\Delta T = 265\,°\text{C}$, a coefficient of thermal expansion for 9-C alloy of $\alpha = 1.11 \times 10^6\,/\,°\text{C}$, a Young's modulus of $E = 172\,\text{GPa}$, and Poisson ratio of $\nu = 0.3$. The lobed wall in the classical hoop-tension configuration (Figure 16.4-3) has a very high structural efficiency (ratio of mean stress under maximum loading to the allowable stress) and good swelling tolerance.

The split at the top and bottom of the torus divides the blanket and the shield into inner and outer half shells which are structurally independent. The tendency of the lobe flat sides to blow out has to be resisted by what are, in effect, the divertor walls (Figure 16.4-3). These wall are 12-cm-thick cantilever beam members which also derive some of their strength from their torsional stiffness and will require internal cooling. These walls are anchored to the 10-cm-thick shield shell by welds at the inside and outside of the shield. The shield is made of cast half-ring sectors, welded together at the inside edge (Figure 16.4-3).

Welding of the main body of the shield to give a 2.5-cm-thick continuous, semicircular member between divertors gives a sufficiently strong beam to prevent "concertina" expansion of the blanket lobes. The shell on the inside of the vertical split includes 15×3-cm retainer frames at about 0.5-m intervals which are welded into the shield. Each 0.5 m of the inner assembly has a force trying to increase its major radius. The magnitude of this expanding force:

$$\begin{aligned} F_{exp} &= \text{Blanket axial area} \times \text{Subtended angle} \times \text{Pressure} \\ &= \tfrac{\pi}{2}(0.96^2 - 0.66^2) \times \sin(10°) \times 7.0 \times 10^6\ \text{N} \\ &= 927{,}950\ \text{N}. \end{aligned} \tag{16.4-30}$$

Each inner assembly presses against both of the retainer frames with a total force of 1,317,866 N. Thus, given a coefficient of friction (ratio of the expanding to retainer forces) greater than 0.16, the lobe assembly will retain itself against "concertina" expansion sideways, ensuring that no outer shell force is required for stability of the inner shell. The 0.16 figure will need to be confirmed by experiment for use in the final design.

It should be pointed out that the present design is relatively flexible and a few of the parameters can easily be adjusted for the final design.

Immediately behind the shield there is a 5-cm-thick zone occupied by the toroidal field (TF) coil which is a multi-turn copper coil held in position by ceramic standoffs from the shield (Figure 16.4-3). The design of the standard elements to support the TF coils is comparatively straightforward since the TF coil has only gravitational and magnetic position stabilizing forces carried externally.

The vacuum boundary is a continuous, 5-mm-thick metal shell immediately outside the TF coil. Because of the large toroidal radius of 5.06 m, such a shell cannot withstand the atmospheric and water-pool pressures totalling about 3 atm without buckling. Accordingly, since the working stress is only about 7 MPa, nonconducting stabilizers similar to those used for the 5-cm-thick TF coil can be used. If necessary, the vacuum boundary can be electrically insulated in the toroidal direction by alternate layers of soft aluminum and hard, anodized 7075 aluminum-alloy sheets. The soft aluminum provides a deformable vacuum seal, and the anodized layer provides the electrical insulation. The two vacuum boundary skins can then be held together by 15-mm-thick stainless-steel, insulator-lined swagged clamps. Details of this method of vacuum-vessel insulation will still need to be demonstrated.

A number of electrically insulated penetrations of the vacuum shell also have to be made for the TF-coil leads. It is envisaged that the technology of automotive spark plugs can be developed to do this task which consists of embedding a precision ceramic insulator in soft metal (usually copper) gaskets. This technique is presently available for diameters an order of magnitude larger than spark plugs, and its extension to sizes relevant to TITAN-II appears feasible. This will also need to be developed.

A skirt, welded to the lower header system and extended to the pool bottom, will support the entire removable first wall, blanket, and shield assembly. This skirt will be of open-frame form to allow free circulation of the pool.

16.4.4. Discussion

The TITAN-II design uses an aqueous salt solution as the coolant. The coolant circulation is essentially loop-type, similar to that for TITAN-I, although the geometry of the blanket-coolant channels is very different. The aqueous salt solution has two advantages as coolant. First, the coolant can act as tritium breeder. Second, the salt content elevates the boiling point of the coolant which can be utilized to reduce primary-coolant pressure below the pressure in the steam generator, eliminating the need for

intermediate heat exchangers. Pressure reduction in a pure-water system cannot be realized because of the lower saturation temperature and the resulting lower critical heat flux.

Among other effects of the salt content, the specific heat capacity is reduced by a factor of about two while the density increases only by 15% which result in a significant reduction in the heat capacity of the coolant. The temperature rise of the primary coolant is 32 °C. Therefore, although the coolant pressure drop is only 1 MPa, the large coolant volume flow rate (39 m^3/s) results in a pumping power of 49 MW, which is very close to that for TITAN-I.

The thermal-hydraulic design of TITAN-II is expected to have adequate safety margins. The maximum heat flux on the first-wall channel is 60% lower than the critical heat flux. The maximum temperature at the mid-plane of the first wall is 503 °C which is less than the allowable limit of 550 °C. The structure temperatures in the blanket and shield coolant channels have even greater safety margins. The maximum pressure stress is less than 50% of the allowable and the thermal stress is below its limit.

16.5. POWER-CYCLE ANALYSIS

The selection of the inlet and exit temperatures of the primary coolant (respectively, 298 and 330 °C) is motivated by the possibility of using a typical fission, pressurized-water-reactor (PWR) power cycle. The lithium-salt content of the TITAN-II aqueous coolant (6.4 at.%) elevates the boiling point of the coolant from 285 °C for pure water to 347 °C at a primary-coolant pressure of 7 MPa. With a primary-coolant pressure of 7 MPa, a higher steam pressure in the steam generator can be selected. During normal operation, if there is any steam-generator tube leakage, the primary coolant will not leak into the steam side. Therefore, the necessity for an intermediate heat exchanger (IHX) can be avoided, resulting in an increase in the power cycle efficiency. Somewhat higher steam temperatures can be obtained with higher primary-coolant pressure, but at the cost of additional expense and complexity associated with IHX and more robust primary piping. Therefore, the TITAN-II reference design uses a power cycle without an intermediate heat exchanger. The steam conditions are similar to those of an existing PWR-type power cycle.

The parameters of a typical PWR power cycle are readily available. The STARFIRE report [136] has a detailed discussion on PWR-type power cycles. That report also discusses some possible improvements which can raise the gross thermal efficiency by

Table 16.5-I.

COMPARISON OF SOME PWR POWER CYCLES

	STARFIRE PWR	Typical PWR
Primary coolant (water):		
Inlet temperature (°C)	280	298
Exit temperature (°C)	320	330
Coolant pressure (MPa)	13.8	15.5
Saturation temperature (°C)	335	345
Exit subcooling (°C)	15	15
Throttle steam conditions:		
Temperature (°C)	299	308
Pressure (MPa)	6.3	7.2
Saturation temperature (°C)	279	289
Gross thermal efficiency	0.34	0.346

one or two percentage points. Other nuclear steam supply systems and power cycles have been reported [137] which are applicable to the TITAN-II design. Table 16.5-I summarizes the parameters for PWR-type power cycles from these two references. These data show that with pure water as the primary coolant, gross thermal efficiency of 34% to 36% can be realized. Further increase of the primary-coolant pressure beyond 15 MPa will not increase the efficiency significantly.

Using an aqueous salt solution as the primary coolant allows the exit temperature of the primary coolant to be significantly increased at the same pressure as that for pure water. However, if the primary coolant pressure is higher than the steam generator pressure (about 7 MPa), then an IHX will be necessary for safety reasons. This reduces some of the benefits of higher primary-coolant exit temperatures. In addition, the use of IHXs increases the capital cost and complexity of the system. By designing for an over-pressure in the steam side, TITAN-II does not need an IHX under normal conditions to

isolate the primary coolant circuit. At 7 MPa pressure and a lithium content of 6.4 at.% in TITAN-II coolant, the primary coolant inlet and exit temperatures can be made equal to those for the typical PWR power cycle given in Table 16.5-I. The primary coolant pressure of 7 MPa is less than the steam generator pressure of 7.2 MPa for this cycle and considerably less than the 15 MPa required in a typical PWR. The parameters of TITAN-II reference power cycle are given in Table 16.5-II which has the same steam cycle parameters as found in Reference [137]. The estimated gross thermal efficiency of the TITAN-II power cycle is 35%.

16.6. SUMMARY AND CONCLUSIONS

The TITAN-II design uses an aqueous solution as the primary coolant and breeder. Two candidate lithium salts, lithium hydroxide (LiOH) and lithium nitrate ($LiNO_3$), were considered because they are highly soluble in water. The $LiNO_3$ salt was selected as the reference salt material for two main reasons. First, LiOH is more corrosive than $LiNO_3$ (Section 16.2.1). Recently, electrochemical corrosion tests were performed for aqueous LiOH and $LiNO_3$ solutions in contact with AISI 316L stainless steels [37]. It was found that stainless steels, particularly low-carbon steels, exhibit better corrosion resistance in $LiNO_3$ solution than in LiOH. Second, from the point of view of radiolysis, $LiNO_3$ solutions are also preferable. Radiolytic decomposition of water results in the formation of free radicals that will ultimately form highly corrosive hydrogen peroxide and OH ions. In an $LiNO_3$ nitrate solution, nitrate ions (NO_3) act as scavengers and reduce the probability of survival of highly reactive radicals in the water during exposure to radiation.

The low-activation ferritic alloy, 9-C, was chosen from among other reduced activation ferritics because of its good strength and elongation behavior after irradiation. The high chromium content (11 wt.%) of this alloy should provide good resistance to corrosion and stress corrosion cracking in an aqueous solutions. The low carbon content (0.09 wt.%), reduces the risk of hydrogen embrittlement. Although no data on the ductile-to-brittle transition temperature (DBTT) is available, it is believed that the high manganese content (6.5 wt.%) of the 9-C alloy will prevent the formation of delta-ferrite phases which are primarily responsible for increases of DBTT. The data base for corrosion of ferritics in $LiNO_3$ solutions is very limited. Indications are, however, that a high-concentration $LiNO_3$ solution does not exhibit unacceptable corrosion problems.

Stress-corrosion cracking (SCC) is a major concern in the nuclear industry. Most recent experiences with SCC in a nuclear environment clearly show that SCC can be

Table 16.5-II.

TITAN-II REFERENCE POWER CYCLE

Primary coolant (water):		
Total thermal power	3027	MW
Inlet temperature	298	°C
Exit temperature	330	°C
Coolant pressure	7	MPa
Saturation temperature	347	°C
Exit subcooling	17	°C
Mass flow rate	4.5×10^4	kg/s
Total pumping power	49	MW
Throttle steam conditions:		
Temperature	308	°C
Pressure	7.2	MPa
Saturation temperature	289	°C
Degree of superheat	19	°C
Gross thermal efficiency	0.35	

suppressed by reducing the oxygen content through the addition of hydrogen to the coolant. The production of tritium in an aqueous lithium-salt solution is seen as an SCC-controlling mechanism. The proper choice of structural material can further reduce the probability of SCC. In particular, coupling a high chromium content with a low carbon content is shown to reduce SCC. The ferritic alloy, 9-C, fulfills both requirements.

Another form of attack on structural material in an aqueous environment is hydrogen embrittlement. The main factors influencing hydrogen embrittlement are the hydrogen content and temperature of the structural alloy. Reducing the amount of atomic hydrogen available for solution in the structure and operating at high temperatures are the most effective means of reducing hydrogen attack. Atomic hydrogen is produced on metal surfaces during corrosion processes. Thus, minimizing corrosion also reduces hydrogen embrittlement of the structure. The production of tritium in the coolant does not necessarily result in an increased hydrogen attack because of rapid recombination to form molecular hydrogen or water molecules. In fact, the Nelson curves, used by the petrochemical industry as guidelines, show that chromium steels can operate at 400 °C with a hydrogen partial pressure of 17 MPa without experiencing hydrogen embrittlement [101].

Radiolytic decomposition of aqueous solutions exposed to a radiation environment is always cause for concern. Experimental data indicate that light-particle radiation (e, γ, X rays) of concentrated $LiNO_3$ salt solutions results in a decrease of decomposition products compared with regular water. Heavy-particle radiation (n, p, α, T) on concentrated $LiNO_3$ solutions also shows a decrease in the formation of radiolytic products, excepting oxygen. However, the production of tritium effectively reduces the oxygen content of the coolant by forming water molecules. Furthermore, the elevated operating temperature of the coolant is shown to be effective in reducing the formation of decomposition products in non-boiling nuclear systems. More experimental data are required so that the radiolytic behavior of concentrated salt solutions can be predicated with a higher degree of confidence.

Neutronics scoping studies resulted in a TITAN-II reference design with a total blanket thickness of 41.5 cm including the first wall, 20 cm of beryllium multiplier zone, 10 cm of ferritic steel breeder/reflector, and 10 cm of shield. With a ^6Li enrichment of 12% in the $LiNO_3$ solution, the tritium-breeding ratio (TBR) is estimated at 1.2 and the blanket energy multiplication at 1.36.

Neutronics scoping studies have shown that the TITAN-II design requires a neutron multiplier to achieve an adequate TBR. Beryllium is the primary neutron multiplier for the TITAN-II design. Investigation of the swelling behavior of beryllium shows the need

for using either low-density, sphere-packed or high-density, fine-grained beryllium. Depending on the type of beryllium chosen, different operating conditions must be satisfied to ensure minimum swelling and retention of structural integrity. Beryllium corrosion by an aqueous solution was also investigated. Past experience shows that minimizing carbonates, sulfates, and chlorates in solution reduces corrosion of beryllium. Coatings have also been developed and their effectiveness has been demonstrated. However, since most of the coatings were developed for radiation-free environments, research is needed to develop coatings that can withstand harsh radiation environments. For the TITAN-II design, a cladding of the 9-C alloy surrounds the beryllium rods.

The primary coolant contains 6.4 at.% lithium with a ^{6}Li enrichment of 12%. Estimated properties of this solution were used in the thermal-hydraulic calculations. Compared to water, this aqueous solution has a higher density, a lower specific heat capacity, and a higher boiling point. This implies that the thermal-hydraulic design of such an aqueous salt blanket will be different from that of a pure-water-cooled design. A lower coolant pressure or a higher operating temperature can be chosen.

Taking advantage of the elevated boiling point of the solution, the reference TITAN-II design operates at a coolant pressure of 7 MPa, with inlet and outlet temperatures of 298 and 330 °C, respectively. The design can handle a first-wall heat flux of 4.6 MW/m^2 using subcooled-flow-boiling heat transfer. The beginning-of-life first-wall midline temperature is 503 °C, which is below the temperature limit for alloy 9-C (550 °C). The primary-coolant pressure has been selected to be lower than the steam-generator pressure (7.2 MPa) so that any leakage in the steam-generator tubes does not result in leaks of the tritium-containing primary coolant to the steam cycle. The necessity for an intermediate heat exchanger is thereby avoided. Pressure reduction in a pure-water system cannot be realized because of the lower saturation temperature and the resulting lower critical heat flux. This power conversion system has a gross thermal efficiency of 35%.

The engineering design study of the TITAN-II FPC indicates that this design is technically feasible. Design approaches to address different critical design areas have been identified. However, experimental investigations and design improvements in several areas are needed to confirm the findings. In the materials area, experimental measurements of the effects of corrosion, hydrogen embrittlement, and radiolysis in aqueous-coolant/ferritic-steel systems are needed. Experimental data to confirm the estimated physical properties of nitrate solution, confirmation of the $LiNO_3$ subcooled-flow-boiling heat transfer, critical heat flux, and pressure drop are essential.

REFERENCES

[1] D. Steiner *et al.*, "A Heavy Water Breeding Blanket," in *Proc. 11th Symp. on Fusion Engineering*, Austin, Texas (1985).

[2] D. S. Gelles, N. M. Ghoniem, and R. W. Powell, "Low Activation Ferritic Alloys Patent Description," University of California Los Angeles report UCLA/ENG-87-9/PPG-1049 (1987).

[3] M. G. Fontana and N. D. Greene, *Corrosion Engineering,* McGraw-Hill International Book Company, Singapore (1978).

[4] J. C. Danko, "Corrosion in the Nuclear Power Industry," *Metals Handbook,* 9th edition, **13** (1987) 927.

[5] H. R. Copson, *Corrosion Resistance of Metals and Alloys,* F. L. LaQue and H. R. Copson (Eds.), American Chemical Society, Reinhold Publishing Corporation, New York (1963) p. 72.

[6] P. A. Akolzin, "The Role of Temperature in the Electrochemical Corrosion of Steel," *Proc. High Temperature High Pressure Electrochemistry in Aqueous Solutions*, sponsored by Central Electricity Research Laboratory, England, National Association of Corrosion Engineers, USA, University of Surrey, England (January 7-12, 1973) 414.

[7] M. E. Indig and A. R. McIree, "High Temperature Electrochemical Studies of the Stress Corrosion of Type 304 Stainless Steel," *Corrosion* **35** (1979) 288.

[8] M. J. Povich and D. E. Broecker, "The Stress Corrosion Cracking of Austenitic Stainless Steel Alloys in High Temperature Air Saturated Water," *Mater. Performance* **18** (1979) 41.

[9] Y. Park, J. R. Galvelle, A. K. Agrawal, and R. W. Staehle, "Stress Corrosion Cracking and Anodic Behavior of AISI 304 Stainless Steel, Inconel 600, and Incoloy 800 Straining in Boiling NaOH Solutions," *Corrosion* **34** (1978) 413.

[10] W. Schoch, H. Wiehn, E. Richter, and H. Schuster, *VGB-Mitteilungen* **52** (1972) 288.

[11] W. H. M. Huijbregts, *KEMA Scientific and Technological Report* **3** (1985) 33.

[12] W. Kastner, K. Roedle, and H. Tratz, *VGB-Kraftwerktechnik* **64** (1984) 452.

[13] J. B. Lee, A. K. Agrawald, and R. W. Staehle, "Corrosion and Corrosion Cracking of Materials for Water-Cooled Reactors," Electric Power Research Institute (EPRI) report NP-1741 (1981).

[14] G. A. A. Van Osch and W. H. M. Huijbregts, "Corrosion Potential Measurements in Boiler Water: The Influence of Oxygen Content," *Corrosion* **42** (1986) 120.

[15] M. G. Fontana and N. D. Greene, *Corrosion Engineering,* McGraw-Hill International Book Company, Singapore (1978) p. 104.

[16] K. N. Nesmeyanova, E. B. Matzevich, and V. G. Kasatkina, in *Proc. 3rd Int. Conf. Metallic Corrosion*, Moscow (1966).

[17] T. Maekawa, M. Kagawa, and N. Nakajima, "Corrosion Behavior in High-Temperature Water and Steam," *J. Japan Inst. Metals* **31** (1967) 1213.

[18] G. Ito, Y. Shimidzu, and T. Usuki, *Corrosion Eng.* **17** (1968) 440.

[19] T. Fujii, T, Kobayashi, and G. Ito, "The Influence of Dissolved Oxygen on the Electrochemical Behavior of Mild Steel and Stainless Steel in Aqueous Solution at Temperatures above 100 °C," *Proc. High Temperature High Pressure Electrochemistry in Aqueous Solutions*, sponsored by Central Electricity Research Laboratory, England, National Association of Corrosion Engineers, USA, University of Surrey, England (January 7-12, 1973) 416.

[20] M. G. Fontana and N. D. Greene, *Corrosion Engineering,* McGraw-Hill International Book Company, Singapore (1978) p. 200.

[21] T. R. Weber , M. A. Stranick, and M. S. Vukasovich, "Molybdate Corrosion Inhibition in Deaerated and Low-Oxygen Waters," *Corrosion* **42** (1986) 542.

[22] M. A. Stranick, "The Corrosion Inhibition of Metals by Molybdates, Part 1: Mild Steel," *Corrosion* **40** (1984) 296.

[23] L. G. Ljungberg, D. Cubicciotti, and M. Trolle, "Material Behavior in Alternate (Hydrogenated) Water Chemistry in the RINGHALS-1 Boiling Water Reactor," *Corrosion* **42** (1986) 263.

[24] B. M. Gordon, W. L. Clarke, M. E. Indig, A. E. Pickett, and M. T. Wang, *Corrosion/81*, Paper No. 20, National Association of Corrosion Engineers, Houston, TX (1981).

[25] R. L. Gowan *et al.*, "Assessment of Operation of the Dresden-2 Nuclear Power Station Under Hydrogen Water Chemistry," prepared by General Electric for Nuclear Energy Business Operation (July 1984).

[26] B. M. Gordon, C. W. Jewett, A. E. Pickett, and M. E. Indig, "Corrosion Resistance Improvement of Ferritic Steels through the Hydrogen Addition to the BWR Coolant," *Proc. of Topical Conference on Ferritic Alloys for Use in Nuclear Energy Technologies*, AIME, Snowbird, UT (June 19-23, 1983) 65.

[27] A. McNinn, "Stress Corrosion of High-Chromium Nickel-Base Metals and AISI 316 Nuclear Grade Stainless Steel in Simulated Boiler Water Reactor Environment," *Corrosion* **42** (1986) 682.

[28] A. B. Bond and H. J. Dundas, "Stress Corrosion Cracking of Ferritic Stainless Steels," *Proc. of Stress Corrosion Cracking and Hydrogen Embrittlement of Iron Base Alloys*, R. W. Staehle, J. Hochmann, R. D. McCright, and J. E. Slate (Eds.), Unieux-Firminy, France (June 12-16, 1973) 1136.

[29] A. B. Bond and H. J. Dundas, "The Effects of Composition on the Stress Corrosion Cracking of Ferritic Steels," *Corrosion* **24** (1968) 344.

[30] R. N. Parkins, "Environmental Aspects of Stress Corrosion Cracking in Low Strength Ferritic Steels," *Proc. of Stress Corrosion Cracking and Hydrogen Embrittlement of Iron Base Alloys*, R. W. Staehle, J. Hochmann, R. D. McCright, and J. E. Slate (Eds.), Unieux-Firminy, France (June 12-16, 1973) 601.

[31] P. L. Andresen, " The Effects of Aqueous Impurities on IGSCC of Sensitized Type 304 Stainless Steel," Electric Power Research Institute (EPRI) report NP-3384 (1983).

[32] R. N. Parkins and R. Usher, *Proc. 1st Int. Congr. Metallic Corrosion*, Butterworths, London (1961) 289.

[33] Z. Szklarska-Smialowska, "Effect of Potential of Mild Steel on Stress Corrosion Cracking in Ammonium Nitrate Solutions," *Corrosion* **20** (1964) 198.

[34] W. Radeker and H. Grafen, *Stahl und Eisen* **76** (1956) 1616.

[35] H. Mazille and H. H. Uhlig, "Effect of Temperature and Some Inhibitors on Stress Corrosion Cracking of Carbon Steels in Nitrate and Alkaline Solutions," *Corrosion* **28** (1972) 427.

[36] R. Waeben, W. Bogaert, and M. Embrecht, "Initial Corrosion Evaluation of Candidate Materials for an ASCB Driver Blanket for NET," *Proc. IEEE 12th Symp. Fusion Engineering*, Monterey, CA (October 12-16, 1987) 1332.

[37] W. F. Bogaerts, M. J. Embrechts, and R. Waeben, "Application of the Aqueous Self-Cooled Blanket Concept to a Tritium Producing Shielding Blanket for NET," University of Leuven (Belgium) report EUR-FU/XII-80/87/75 (1987).

[38] H. A. Bethe and J. Ashkin, *Experimental Nuclear Physics,* E. Serge (Ed.), John Wiley & Sons, Inc., New York (1953) p. 166.

[39] R. H. Schuler and A. O. Allen, "Radiation Chemistry Studies with Cyclotron Beams of Variable Energy: Yield in Aerated Ferrous Sulfate Solutions," *J. Am. Chem. Soc.* **79** (1957) 1565.

[40] P. R. Burch, *Radiat. Res.* **6** (1957) 289.

[41] E. Pollard, *Advances in Biological and Medical Physics* **3** (1953) 153.

[42] A. O. Allen, *The Radiation Chemistry of Water and Aqueous Solutions,* D. Van Nostrand Company, Inc., New Jersey (1961).

[43] A. K. Pikaev, in *Pulse Radiolysis of Water and Aqueous Solutions,* E. J. Hart (Ed.), Indiana University Press, Bloomington & London (1967).

[44] D. C. Walker, "Hydrated Electrons in Chemistry," in *Radiation Chemistry, Vol. 1*, R. F. Gould (Ed.), American Nuclear Society, Washington D. C. (1968).

[45] P. Gunther, "Helium-bildung aus α-Strahlern," *Z. Phys. Chem.* **185** (1939) 367.

[46] P. Cohen, "Water Coolant Technology of Power Reactors," American Nuclear Society (1980).

[47] W. M. Dale, L. H. Gray, and W. J. Meredith, *J. Phil. Trans.* **A242** (1949) 33.

[48] W. Duane and O. Scheuer, *Le Radium* **10** (1913) 33.

[49] M. Lefort, "Radiochimie Des Solutions Aqueouses," *J. Chem. Phys.* **51** (1954) 351.

[50] M. Daniels, "Radiolysis and Photolysis of the Aqueous Nitrate System,"in *Radiation Chemistry, Vol. 1*, R. F. Gould (Ed.), American Nuclear Society, Washington D. C. (1968).

[51] G. H. Jenks, "Effects of Reactor Operation on HFIR Coolant," Oak Ridge National Laboratory report ORNL-3848 (1985).

[52] J. T. Kiwi and M. Daniels, "On the Radiolysis of Concentrated Alkaline and Calcium-Nitrate Solutions," *J. Inorg. Nucl. Chem.* **40** (1978) 576.

[53] H. A. Schwarz, "The Effect of Solutes on the Molecular Yields in the Radiolysis of Aqueous Solutions," *J. Am. Chem. Soc.* **77** (1955) 4960.

[54] J. A. Lane, H. G. MacPherson, and F. Maslan, "Fluid Fuel Reactors," in *Atoms for Peace,* Addison-Wesley Publishing Company, Inc., New York (1958).

[55] T. J. Sworski, "Yield of Hydrogen Peroxide in the Decomposition on Water by Cobalt γ-Radiation. I: Effect of Bromide Ion," *J. Am. Chem. Soc.* **76** (1954) 4687.

[56] A. O. Allen and R. A. Holroyd, "Peroxide Yield in the γ-Irradiation of Air-saturated Water," *J. Am. Chem. Soc.* **77** (1955) 5852.

[57] R. G. Sowden, "The Effect of Nitrate Ion on the Yield of Hydrogen from Water Radiolysis," *J. Am. Chem. Soc.* **79** (1957) 1263.

[58] M. Burton and K. C. Kurien, "Effects of Solute Concentration in Radiolysis of Water," *J. Phys. Chem.* **63** (1959) 899.

[59] W. G. Burns and P. B. Moore, "The Radiation Chemistry of High Temperature (300-400 °C) Water," Harwell Laboratory report AERE-R9516, England (1980).

[60] R. F. S. Robertson and P. G. Anderson, "Out-Reactor Test of HTP Loop," National Research Council of Canada report CRDC-596 (June 1955); also issued as Atomic Energy of Canada, Ltd. report AECL-195.

[61] T. Kambara, R. M. Whites, and F. S. Rowland, "The Reactions of Recoil Tritium Atoms in Aqueous Solution," *J. Inorg. Nucl. Chem.* **21** (1961) 210.

[62] R. H. Wood, University of Delaware, Newark, personal communication, August 1987.

[63] L. V. Puchkov and V. G. Matashkin, "Densities of $LiNO_3$–H_2O and $NaNO_3$–H_2O Solutions at Temperatures in the Range 25 – 300 °C," *J. App. Chem. USSR* **43** (1970) 1864.

[64] L. V. Puchkov, V. G. Matashkin, and R. P. Matveeva, "Density of Aqueous Lithium Nitrate Solutions at High Temperatures (up to 350 °C) and Concentrations," *J. App. Chem. USSR* **52** (1979) 1167.

[65] L. V. Puchkov and P. M. Sargaev, "Viscosities of Lithium, Sodium, Potassium, and Ammonium Nitrate Solutions at Temperatures up to 275 °C," *J. App. Chem. USSR* **46** (1973) 2367.

[66] L. V. Puchkov and P. M. Sargaev, "Dependence of Viscosity of Electrolyte Solutions on Temperature and Concentration," *J. App. Chem. USSR* **47** (1974) 280.

[67] R. H. Wood and J. R. Quint, "A Relation between the Critical Properties of Aqueous Salt Solutions and the Heat Capacity of the Solutions Near the Critical Point Using a Single-Fluid Corresponding-States Theory," *J. Chem. Thermodynamics* **14** (1982) 14.

[68] W. L. Marshall and E. V. Jones, "Liquid-Vapor Critical Temperatures of Aqueous Electrolyte Solutions," *J. Inorg. Nucl. Chem.* **36** (1974) 2313.

[69] S. Sourirajan and G. C. Kennedy, "The System H_2O–NaCl at Elevated Temperatures and Pressures," *Am. J. Sci.* **260** (1962) 115.

[70] H. Ozbek and S. L. Phillips, "Thermal Conductivity of Aqueous Sodium Chloride Solutions from 20 to 330 °C," *J. Chem. Eng. Data* **25** (1980) 263.

[71] G. A. Sacchetto, G. G. Bombi, and C. Macca, "Vapor Pressure of Very Concentrated Electrolyte Solutions," *J. Chem. Thermodynamics* **13** (1981) 31.

[72] "Standards for Protection Against Radiation," U. S. Nuclear Regulatory Commission, Code of Federal Regulations, Title 10, Part 0 to 199 (1986).

[73] D. N. Braski, "The Effect of Neutron Irradiation on the Tensile Properties and Microstructure of Several Vanadium Alloys," in *Proc. ASTM Conf. on Fusion Reactor Materials*, Seattle, WA (1986).

[74] W. E. Kenedy, Jr. and F. M. Mann, "Potential Low-Level Waste Disposal Limits for Fusion Radionuclides," *Trans. Am. Nucl. Soc.* **45** (1983) 51.

[75] F. M. Mann, "Reduced Activation Calculations for the Starfire First Wall," *Fusion Technol.* **6** (1984) 273.

[76] S. A. Fetter, "Radiological Hazards of Fusion Reactors: Models and Comparisons," Ph. D. Thesis, University of California Berkeley (1985).

[77] D. G. Doran, A. F. Rowcliffe, and F. M. Mann, "Prospects for Reduced Activation Alloys," *J. Nucl. Mater.* **141-143** (1986) 1074.

[78] T. Lechtenberg, "Irradiation Effects in Ferritic Steels," *J. Nucl. Mater.* **133-134** (1985) 149.

[79] R. L. Klueh, D. S. Gelles, and T. A. Lechtenberg, "Development of Ferritic Steels for Reduced Activation: The U. S. Program," *J. Nucl. Mater.* **141-143** (1986) 1081.

[80] C. Y. Hsu and T. A. Lechtenberg, "Alloy Development for Irradiation Performance, ADIP Semiannual Progress Report," U. S. Department of Energy report DOE/ER-0045/15 (Sept. 30, 1985) 137.

[81] J. M. Vitek and R. L. Klueh, "Alloy Development for Irradiation Performance, ADIP Semiannual Progress Report," U. S. Department of Energy report DOE/ER-0045/12 (March 31, 1984) 110.

[82] T. A. Lechtenberg, General Atomics, San Diego, CA, private communication, March 1987.

[83] E. T. Cheng and R. W. Conn, "Waste Disposal Ratings in the TITAN RFP Reactor," *Proc. IEEE 12th Symp. on Fusion Engineering*, Monterey, CA (October 12-16, 1987) 913.

[84] B. Craig, "Hydrogen Damage," *Metals Handbook*, 9th edition **13** (1987) 163.

[85] H. Howarth, "The Oxidation Resistance of Low-Alloy Steels," *Corrosion: Metal/Environment Reactions*, L. L. Shreir (Ed.), Newnwe-Butterworth, London (1977) 7:13.

[86] L. Raymond, "Evaluation of Hydrogen Embrittlement," *Metals Handbook,* 9th edition **13** (1987) 283-290.

[87] R. W. Staehle, J. Hochmann, R. D. McCright, and J. E. Slate (Eds.), *Proc. of Stress Corrosion Cracking and Hydrogen Embrittlement of Iron Base Alloys*, Unieux-Firminy, France (June 12-16, 1973).

[88] P. Azou (Ed.), *Third International Congress on Hydrogen and Materials*, Pergamon Press (1982).

[89] C. D. Beachem (Ed.), *Hydrogen Damage,* American Society for Metals (1977).

[90] I. M. Bernstein and A. W. Thompson (Eds.), *Hydrogen Effects in Metals,* American Institute of Mining, Metallurgical, and Petroleum Engineers (1981).

[91] H. H. Johnson, E. J. Schneider, and A. R. Troiano, *Trans. American Inst. Mining Engineers* **212** (1958) 5.

[92] R. P. M. Procter and H. W. Paxton, *Trans. Amer. Soc. Metals* **62** (1969) 989.

[93] W. W. Gerberich, "Effect of Hydrogen on High Strength and Martensitic Steel," in *Hydrogen in Metals,* I. M. Bernstein and A. W. Thompson (Eds.), American Society for Metals (1974) 115.

[94] G. Sandoz, "A Unified Theory for Some Effects of Hydrogen Source, Alloying Elements and Potential on Crack Growth in Martensitic AISI 4330 Steel," *Metall. Trans.* **3** (1972) 213.

[95] B. A. Graville, R. G. Baker, and F. Watkinson, *Br. Weld J.* **14** (1967) 337.

[96] D. H. Zhon, W. X. Zhon, and Z. L. Xu, "Hydrogen Degradation of 21-6-9 and Medium Carbon Steels by Disk-Pressure Test," *J. Nucl. Mater.* **141-143** (1986) 503.

[97] H. R. Gray, "Testing for Hydrogen Environment Embrittlement: Experimental Variables," *Hydrogen Embrittlement Testing,* American Society for Testing and Materials (ASTM STP 543), Philadelphia (1974) p. 133.

[98] J. P. Fidelle, R. Borudeur, C. Rowx, and M. Rapin, "Disk Pressure Testing of Hydrogen Environemnt Embrittlement," *Hydrogen Embrittlement Testing,* American Society for Testing and Materials (ASTM STP 543), Philadelphia (1974) p. 221.

[99] W. T. Chandler and R. J. Walter, "Testing to Determine the Effect of High-Pressure Hydrogen Environments on the Mechanical Properties of Metals," in *Hydrogen Embrittlement Testing,* American Society for Testing and Materials (ASTM STP 543), Philadelphia (1974) p. 171.

[100] R. S. Treseder, "Guarding Against Hydrogen Embrittlement," *Chem. Eng.* **29** (1981) 105.

[101] "Steels for Hydrogen Service at Elevated Temperatures and Pressures in Petroleum Refineries and Petrochemical Plants," API Publication 941, 2nd edition (1971).

[102] D. Webster and G. J. London (Eds.), *Beryllium Science and Technology,* Plenum Press, New York and London (1979).

[103] J. N. Wanklyn and P. J. Jones, "The Aqueous Corrosion of Reactor Metals," *J. Nucl. Mater.* **63** (1962) 291.

[104] A. J. Stonehouse and W. W. Beaver, "Beryllium Corrosion and How to Prevent It," *Mater. Prot.* **4** (1965) 24.

[105] P. D. Miller and W. K. Boyd, "Beryllium Deters Corrosion - Some Do's and Don'ts," *Mater. Eng.* **68** (1968) 33.

[106] J. Brooker and A. J. Stonehouse, "Chemical Conversion Coatings Retard Corrosion of Beryllium," *Mater. Prot.* **8** (1969) 43.

[107] J. B. Rich and G. P. Walters, "The Effects of Heating Neutron Irradiated Beryllium," *J. Nucl. Mater.* **1** (1959) 96.

[108] C. E. Ells and E. C. W. Perryman, "Effects of Neutron-Induced Gas Formation on Beryllium," *J. Nucl. Mater.* **1** (1959) 73.

[109] J. R. Weir, "The Effects of High-Temperature Reactor Irradiation on Some Physical and Mechanical Properties of Beryllium," *Proc. of Int. Conf. Metallurgy of Beryllium,* Institute of Metals, London (October 1961) 362.

[110] J. B. Rich and R. S. Barnes, "Mechanical Properties of Some Highly Irradiated Beryllium," *J. Nucl. Mater.* **4** (1961) 287.

[111] M. O. Tucker and R. J. White, "The Geometry in Interlinked Grain Edge Porosity," *Res Mechanica* **1** (1980) 21.

[112] J. M. Beeston, M. R. Martin, C. R. Brickman, G. E. Korth, and W. C. Francis, *Symp. on Materials Performance in Operating nuclear Systems,* Ames Laboratory report CNF-730801, Ames, IA (August 1978) 59.

[113] J. M. Beeston, L. G. Miller, E. L. Wood, and R. W. Moir, "Comparison of Compression Properties and Swelling of Beryllium Irradiated at Various Temperatures," Idaho National Engineering Laboratory report EGG-FT-6608 (1984).

[114] R. S. Barnes and G. B. Redding, "Neutron Lifetime Measurement in the Fast Reactors Zeus and Zephyr," *Nucl. Energy* **10** (1959) 22.

[115] J. B. Rich, "The Mechanical Properties of Beryllium Irradiated At 350 and 600 °C," *The Metallurgy of Beryllium,* Institute of Metals, Chapman and Hall, Ltd., London (1963) 135.

[116] L. E. Muir, *Interfacial Phenomena in Metals and Alloys,* Addison-Wesley Publishing Corp., Reading, MA (1975) 124.

[117] W. G. Wolfer and T. J. McGarville, "Swelling of Beryllium," in *Damage Analysis and Fundamental Studies,* U. S. Department of Energy report DOE/ER-0046/19 (November 1984).

[118] N. L. Peterson, "Self-Diffusion in Pure Metals," *J. Nucl. Mater.* **69 & 70** (1978) 3.

[119] J. M. Beeston, "Gas Release and Compression Properties in Beryllium Irradiated at 600 and 700 °C," *Effects of Irradiation on Structural Metals*, American Society of Testing and Materials (ASTM STP 426) (1967) 135.

[120] G. P. Marino, "The Porosity Correction Factor for the Thermal Conductivity of Ceramic Fuels," *J. Nucl. Mater.* **38** (1971) 178.

[121] C. E. Ells and J. R. Weir, "The Effects of Neutron Irradiation on the Plastic Deformation and Fracture of Beryllium," *J. Nucl. Mater.* **13** (1964) 49.

[122] L. G. Miller, J. M. Beeston, B. L. Harris, and C. P. C. Wong, "Special Topics Reports for the Reference Tandem Mirror Fusion Breeder: Beryllium Lifetime Assessment," Lawrence Livermore National Laboratory report UCID-20166 (1984).

[123] T. J. McCarville, D. H. Berwald, W. Wolfer, F. J. Fulton, J. D. Lee, *et al.*, "Technical Issues for Beryllium Use in Fusion Blanket Applications," Lawrence Livermore National Laboratory report UCID-20319 (1985).

[124] W. W. Engle, Jr., "A User's Manual for ANISN, A One-Dimensional Discrete Ordinates Transport Code with Anisotropic Scattering," Oak Ridge Gaseous Diffusion Plant, K-1693 (1967).

[125] R. MacFarlane, "Nuclear Data Libraries from Los Alamos for Fusion Neutronics Calculations," *Trans. Am. Nucl. Soc.* **36** (1984) 271.

[126] A. E. Bergles and W. M. Rohsenow, *J. Heat Trans.* **C86** (1964) 365.

[127] W. H. Jens and P. A. Lottes, "Analysis of Heat Transfer, Burnout, Pressure Drop and Density Data for High Pressure Water," U. S. Atomic Energy Commission report ANL-4627 (1951).

[128] R. J. Weatherhead, "Nucleate Boiling Characteristics and Critical Heat Flux Occurrence in Subcooled Axial Flow Water System," U. S. Atomic Energy Commission report ANL-6675 (1962).

[129] J. R. S. Thom, W. M. Walker, T. A. Fallon, and G. F. S. Reising, "Boiling in Subcooled Water During Flow in Tubes and Annuli," *Proc. Inst. Mech. Engr.* **3C** (1965-66) 180.

[130] R. D. Boyd, C. P. C. Wong, and Y. S. Cha, "Technical Assessment of Thermal-Hydraulics for High Heat Flux Fusion Components," Sandia National Laboratory report SAND-84-0159 (1985).

[131] S. L. Milora, S. K. Combs, and C. A. Foster, "A Numerical Model for Swirl Flow Cooling in High-Heat-Flux Particle Beam Targets and the Design of a Swirl-Flow-Based Plasma Limiter," Oak Ridge National Laboratory report TM-9183 (1984).

[132] M. Z. Hasan, M. M. Hasan, R. Eichhorn, and J. H. Lienhard, "Boiling Burnout During Crossflow Over Cylinders," *J. Heat Trans.* **C103** (1981) 478.

[133] L. S. Tong, *Boiling Heat Transfer and Two-Phase Flow,* Robert E. Krieger Publishing Co., New York (1975).

[134] H. Schlichting, *Boundary Layer Theory,* McGraw-Hill Book Co., New York (1979).

[135] J. G. Collier, *Convective Boiling and Condensation,* McGraw-Hill, London (1972).

[136] C. C. Baker, M. A. Abdou, R. M. Aron, *et al.*, "STARFIRE– A Commercial Tokamak Fusion Power Plant Study," Argonne National Laboratory report ANL/FPP-80-1 (1980).

[137] "Steam/Its Generation and Use," Babcock & Wilcox Co. (1978).